

## **Study of improved design and physical properties of $12\text{CaO}\cdot 7\text{Al}_2\text{O}_3$ thin films**

Feizi, Elnaz

The copyright of this thesis rests with the author and no quotation from it or information derived from it may be published without the prior written consent of the author

For additional information about this publication click this link.

<http://qmro.qmul.ac.uk/jspui/handle/123456789/8801>

Information about this research object was correct at the time of download; we occasionally make corrections to records, please therefore check the published record when citing. For more information contact [scholarlycommunications@qmul.ac.uk](mailto:scholarlycommunications@qmul.ac.uk)

**Study of improved design and physical  
properties of  $12\text{CaO}\cdot 7\text{Al}_2\text{O}_3$  thin films**

**ELNAZ FEIZI**

**School of Engineering and Materials Science**

**Queen Mary, University of London**

A THESIS SUBMITTED IN FULFILMENT OF THE REQUIREMENTS FOR THE  
DEGREE OF DOCTOR OF PHILOSOPHY OF THE UNIVESITY OF LONDON

March 2012

## **Declaration**

I hereby declare that the work carried out and presented in this thesis is based on my own work and that it has not been submitted as an exercise for any other qualification. Wherever contributions of others were involved, it is fully acknowledged.

Name                    ELNAZ FEIZI

Signature

Date

## Abstract

Calcium aluminate compound,  $12\text{CaO}\cdot 7\text{Al}_2\text{O}_3$ , was prepared via an improved sol-gel technique in the form of thin film on magnesium oxide (MgO) single crystal substrate as well as powder. The microstructures of the films were observed before and after crystallization, and the effect of solution processing parameters, including the molar fractions of the ingredients, on the continuity of the films and the formation of surface defects was studied. An optimized sol-gel process using a new solution recipe was developed based on the microstructural observations. Homogeneous thin films of  $12\text{CaO}\cdot 7\text{Al}_2\text{O}_3$  with high critical thickness ( $\sim 5 - 6 \mu\text{m}$ ) were produced using this optimized technique.

The chemical composition of the films was determined using energy dispersive spectroscopy and X-ray photoelectron spectroscopy. Raman and Fourier transform infrared (FTIR) spectral analyses were employed in order to investigate the effect of heat treatment temperature on the crystallization of  $12\text{CaO}\cdot 7\text{Al}_2\text{O}_3$  film on magnesium oxide substrate. The results of the phase analysis show that a single-phase film of  $12\text{CaO}\cdot 7\text{Al}_2\text{O}_3$  is formed at a temperature of  $1300^\circ\text{C}$ . A crystallized structure with well-defined grain boundaries is obtained after 2 hr of heat treatment at this temperature under normal air atmosphere.

The phase formation of  $12\text{CaO}\cdot 7\text{Al}_2\text{O}_3$  in powder form was investigated via room-temperature and high-temperature X-ray diffraction (XRD) and crystallization of  $12\text{CaO}\cdot 7\text{Al}_2\text{O}_3$  and  $\text{CaO}\cdot \text{Al}_2\text{O}_3$  powders started taking place simultaneously at a temperature of  $\sim 900^\circ\text{C}$ .

A comparison between the FTIR results of the films with XRD results of the powder proved the crystallization of  $12\text{CaO}\cdot 7\text{Al}_2\text{O}_3$  thin film to start at a higher temperature compared to the powder. Furthermore, a single-phase  $12\text{CaO}\cdot 7\text{Al}_2\text{O}_3$  tends to form in thin film on MgO substrate, whereas the formation of  $12\text{CaO}\cdot 7\text{Al}_2\text{O}_3$  is accompanied by the formation of secondary phases of  $\text{CaO}\cdot \text{Al}_2\text{O}_3$  and  $3\text{CaO}\cdot \text{Al}_2\text{O}_3$ .

The optical absorption properties of the  $12\text{CaO}\cdot 7\text{Al}_2\text{O}_3$  films were investigated at different temperatures from room temperature to  $300\text{ }^\circ\text{C}$  and the experimental data were analysed in Tauc and Urbach regions. The optical band gap decreased from  $4.088\text{ eV}$  at  $25\text{ }^\circ\text{C}$  to  $4.051\text{ eV}$  at  $300\text{ }^\circ\text{C}$ , while Urbach energy increased from  $0.178\text{ eV}$  at  $25\text{ }^\circ\text{C}$  to  $0.257\text{ eV}$  at  $300\text{ }^\circ\text{C}$ .

The relationship between the optical band gap and the Urbach energy at different temperatures showed an almost linear relationship from which the theoretical values of  $4.156$  and  $0.065\text{ eV}$  were evaluated for the band gap energy and Urbach energy of a  $12\text{CaO}\cdot 7\text{Al}_2\text{O}_3$  crystal with zero structural disorder at  $0\text{ K}$ .

## **Acknowledgement**

I would like to show my deepest gratitude to my supervisor Professor Asim Ray for his valuable guidance and support throughout my research.

I would also like to thank Dr. Rory Wilson, Dr. Zofia Luklinska, Dr. George Fern, Dr. Paolo Coppo, Dr. Colin Catherall, Dr. Terry Ireland, Ms Lorna Anguilano, Dr. Nima Roohpour, Mr. Olivier Savard, Mr. Abdul Ghani and Dr. Akbar Rahide for their advice and training.

I would like to thank my friends Carlos, Chandana, Marjan, Zahra, Jasminder, Charline, Olivier and Amin for their friendship and support.

I would specially like to thank Dr. Jesus Ojeda who helped me with my experiments. Special thanks to Father John Hunter for revising my thesis.

Finally I would like to thank my parents for their unconditional love and support.

## Table of Contents

<b>Chapter 1: Introduction</b>	21
<b>Chapter 2: Literature Review</b>	25
2.0 Introduction	25
2.1 Structural and physical properties of C12A7	25
2.1.1 Atomic structure	25
2.1.2 Thermal stability	33
2.1.3 Ionic conductivity and mechanisms of oxide-ion migration	34
2.2 Electronic structure of C12A7 and incorporation of ionic species	37
2.3 Electron-incorporated C12A7	40
2.3.1 An introduction to C12A7 electride	40
2.3.2 Atomic and electronic structure	42
2.3.3 Electrical conductivity	44
2.4 Optical properties of C12A7	47
2.4.1 Optical absorption	47
2.4.2 Reflectivity	54
2.4.3 Luminescence	55
2.4.4 Photochromism	56
2.5 C12A7 fabrication techniques	57
2.6 Fabrication of C12A7 via sol-gel technique	59
2.6.1 Ingredients for solution preparation	60
2.6.2 Chelation	62
2.6.3 Hydrolysis	64
2.6.4 Addition of acid	66
2.6.5 Thin film application	67

2.6.6 Heat treatment	67
2.7 Anion-incorporated C12A7 fabrication techniques	69
2.7.1 Incorporation with superoxides	69
2.7.2 Incorporation with hydroxide	72
2.7.3 Incorporation with hydride	73
2.7.4 Incorporation with heavy metal ions	73
2.7.5 Incorporation with fluoride	74
2.8 Electron-incorporated C12A7 fabrication techniques	75
2.8.1 Heat treatment in a reducing atmosphere of H <sub>2</sub> plus UV irradiation	76
2.8.2 Heat treatment in a metal-vapour atmosphere	78
2.8.3 Melt-solidification and glass-ceramic processing in a reducing atmosphere	80
2.8.4 Heat treatment in a reducing gas atmosphere of CO/CO <sub>2</sub>	82
2.8.5 Hot implantation of inert-gas ions	83
2.8.6 Chemical reduction treatment using oxygen-deficient amorphous	84
2.8.7 Hot proton implantation plus UV irradiation	84
2.9 Applications of C12A7	85
<b>Chapter 3: Experimental Procedure</b>	89
3.0 Introduction	89
3.1 Solution preparation	89
3.2 Sample preparation	93
3.3 Heat treatment	95
3.4 Microstructural observations	96
3.5 Chemical analysis	98
3.5.1 Energy dispersive spectroscopy	98



3.5.2 X-ray diffraction	99
3.5.3 X-ray photoelectron spectroscopy	101
3.5.4 Fourier transform infrared spectroscopy: Attenuated total reflectance	104
3.5.5 Raman spectroscopy	106
3.6 Differential scanning calorimetry/ thermal gravimetric analysis	108
3.7 Optical properties	109
3.7.1 Absorbance and reflectance measurements at room temperature	109
3.7.2 High-temperature optical absorption	111
<b>Chapter 4: Microstructure and chemical composition</b>	<b>113</b>
4.1 Chemical stability of the solution	113
4.2 Thin film surface microstructure	114
4.3 Chemical analysis of the thin films and powder	125
4.3.1 Energy dispersive spectroscopy	125
4.3.2 X-ray photoelectron spectroscopy	126
4.3.3 Room-temperature powder X-ray diffraction analysis	128
4.3.4 High-temperature powder X-ray diffraction analysis	137
4.3.5 Differential scanning calorimetry and thermal gravimetric analysis	138
<b>Chapter 5: FTIR and Raman spectral analyses of C12A7 thin film and powder</b>	<b>142</b>
5.0 Introduction	142
5.1 FTIR-ATR spectral analysis of the thin films	143
5.2 Raman spectral analysis of the powder and the thin films	158
<b>Chapter 6: Optical absorption properties of C12A7 thin films</b>	<b>169</b>
6.1 Optical properties at room temperature	169

6.1.1 Optical absorption and its relationship with transmittance and reflectance	169
6.1.2 Determination of the refractive index, extinction coefficient and dielectric constant	172
6.1.3 Absorption coefficient and Tauc's law	178
6.1.4 Absorption tail and Urbach's law	182
6.2 Absorption properties at high temperatures	184
6.2.1 Variation of the absorption coefficient with temperature	184
6.2.2 Variation of the Urbach energy with temperature	186
6.2.3 Variation of the steepness parameter with temperature	190
6.2.4 Variation of the band gap energy with temperature	192
6.2.5 The relationship between the band gap energy and Urbach energy	195
<b>Chapter 7: Conclusions and future work</b>	197
<b>References</b>	202

## List of Figures

- Figure 2.1** Position of C12A7 compound in the binary phase diagram of CaO- $\text{Al}_2\text{O}_3$  26
- Figure 2.2** Schematic structures of C12A7 (a) unit cell [17], (b) the connection between two neighbouring cages via the cage opening [12]. Cage A and B are shown from the top and side views respectively. 28
- Figure 2.3** Schematic structures of (a) an empty cage and (b) an occupied cage filled with an  $\text{O}^{2-}$  ion. Upon  $\text{O}^{2-}$  occupation, one of the  $\text{Ca}^{2+}$  ions displaces towards the centre of the cage along the  $S_4$  axis.  $\text{O}_{(\text{III})}$  state is the position of extra-framework  $\text{O}^{2-}$  ion inside the cage [25]. 29
- Figure 2.4** Two possible routes for the migration of an extra-framework  $\text{O}^{2-}$  ion from one cage to another involving crystallographic states  $\text{O}_{(\text{III})}$ - $\text{O}_{(\text{I})}$ - $\text{O}_{(\text{I})}'$ - $\text{O}_{(\text{III})}'$  [14] 35
- Figure 2.5** Electronic transitions for C12A7 incorporated with different ionic species. The excitation energy for each transition is also given [15] 38
- Figure 2.6** Schematic illustration of cage and framework conduction bands energy levels and the position of electrons states in C12A7 electride [9] 44
- Figure 2.7** Temperature dependency of conductivity for semiconducting and conductive C12A7 [7] 45
- Figure 2.8** Temperature dependency of conductive C12A7 [50] in comparison with ITO thin films in a temperature range of 70-500 K. ITO films were prepared in four different thicknesses using electron beam evaporation and subsequent heat treatment at 800 °C for 3 hr [51] 46
- Figure 2.9** Comparison between the optical absorption spectra of the  $\text{O}^{2-}$  and electron-incorporated C12A7 [24] 52
- Figure 2.10** Dependence of optical absorption edge on temperature for C12A7 annealed in moist atmosphere. The absorption edge shifts towards lower energies with an increase in the temperature [15] 53
- Figure 2.11** Reflectivity spectrum of a C12A7 single crystal [43] compared to the reflectivity of the constituents  $\text{Al}_2\text{O}_3$  [58] and CaO [59] 54

<b>Figure 2.12 Comparison between the luminescence spectra of <math>O^{2-}</math> and <math>OH^-</math> - incorporated C12A7 at 10 K excited by 6.9 eV photons [60]</b>	55
<b>Figure 2.13 Schematic outline of sol-gel process</b>	60
<b>Figure 2.14 Chelation of aluminum sec-butoxide with ethyl acetoacetate [68, 75]</b>	63
<b>Figure 2.15 Hydrolysis reaction of aluminum sec-butoxide chelated with ethyl acetoacetate [75]</b>	65
<b>Figure 2.16 Schematic illustration of superoxide formation. The extra-framework <math>O^{2-}</math> is oxidized by oxygen molecules at the surface of the material and the products enter the empty cages by inward diffusion in order to compensate for the lack of negative charge in the framework [85]</b>	71
<b>Figure 2.17 Schematic illustration of electron incorporation mechanism in C12A7 via heat treatment in presence of calcium metal. The extra-framework oxygen ions diffuse to the ceramic-metal interface and oxidize Ca leaving electrons behind in order to compensate for the lack of negative charge of the ceramic framework [40].</b>	79
<b>Figure 2.18 Schematic illustration of (a) melt-solidification treatment [96], and (b) glass-ceramic processing [49] of C12A7 under the reducing atmosphere. The temperatures of 900 and 1450°C are the crystallization temperature and the melting point of C12A7 respectively.</b>	80
<b>Figure 2.19 Schematic illustration showing the formation of C12A7 electride in a reducing atmosphere with <math>C_2^{2-}</math> ions acting as templates for oxygen ion removal [1]</b>	81
<b>Figure 3.1 Schematic illustration of solution preparation</b>	90
<b>Figure 3.2 Partial phase diagram of the binary CaO-<math>Al_2O_3</math> system</b>	90
<b>Figure 3.3 Schematic illustration of scanning electron microscope components [106]</b>	97
<b>Figure 3.4 Schematic illustration of (a) constructive scattering which satisfies Bragg's law and (b) destructive scattering of waves which cancel each other [108]</b>	100

<b>Figure 3.5 X-ray photoelectron spectrometry setup</b>	101
<b>Figure 3.6 Schematic illustration of X-ray photoelectron spectroscopy [109]</b>	102
<b>Figure 3.7 Schematic illustration of ATR system operation [111]</b>	105
<b>Figure 3.8 Schematic illustration of the vibrational energy states involved in Raman signal [112]</b>	107
<b>Figure 3.9 Integrating sphere configuration and the sample position in transmission and reflection modes [114]</b>	111
<b>Figure 3.10 High-temperature UV-Vis spectrometry setup</b>	112
<b>Figure 4.1 Transparency of the prepared solution versus time, the solution ingredients and the molar ratios used for solution preparation.</b>	113
<b>Figure 4.2 Microstructure of the thin films prepared with methanol-to-ASB molar ratio of (a) 40:1 and (b) 20:1. The molar ratios of 3:1 for EAA-to-ASB and 20:1 for water-to-ASB were used for both solutions. The films have been heat treated at 1300 °C for 2 hr in an air atmosphere.</b>	115
<b>Figure 4.3 Schematic illustration of different types of aggregation growth [118]</b>	118
<b>Figure 4.4 Microstructure of the thin film (a) before and (b) after heat treatment at 1300 °C for 2 hr. The molar ratios of 20:1 for methanol-to-ASB, 3:1 for EAA-to-ASB, and 20:1 for water-to-ASB ratios were chosen for the preparation of the solution.</b>	119
<b>Figure 4.5 Microstructure of the thin film with a water-to-ASB molar ratio of 5:1. The film is heat treated at 1300 °C for 2 hr in air atmosphere.</b>	121
<b>Figure 4.6 Microstructure of the thin film prepared with a solution containing a molar ratio of 5:1 for methanol-to-ASB and water-to-ASB. The film was heat treated at 1300 °C for 2 hr in air atmosphere.</b>	122
<b>Figure 4.7 Microstructure of the thin film prepared with a solution containing isopropyl alcohol as the solvent. The molar ratio of 10:1 and 5:1 were chosen for isopropyl alcohol-to-ASB and water-to-ASB respectively. The film was heat treated at 1300 °C for 2 hr in air atmosphere. The figures were taken from the same sample with different magnifications.</b>	124

<b>Figure 4.8 Energy dispersive spectrum of C12A7 thin film</b>	125
<b>Figure 4.9 X-ray photoelectron spectrum of the thin film before the annealing treatment</b>	127
<b>Figure 4.10 X-ray photoelectron spectrum of the thin film after a heat treatment at 1300 °C for 2 hr in air atmosphere</b>	127
<b>Figure 4.11 X-ray diffraction pattern of the dried gel after a heat treatment at 700 °C for 15 hr</b>	129
<b>Figure 4.12 X-ray diffraction pattern of the dried gel after a heat treatment at 1100 °C for 6 hr</b>	130
<b>Figure 4.13 X-ray diffraction pattern of the dried gel after a heat treatment at 1300 °C for 6 hr</b>	131
<b>Figure 4.14 Comparison between the X-ray diffraction patterns of the dried gel after heat treatment at 1100 and 1300 °C</b>	132
<b>Figure 4.15 Williamson-Hall plot for C12A7 powder. The data was obtained from the diffraction peaks of the compound after a heat treatment at 1300 °C for 6 hr.</b>	135
<b>Figure 4.16 Effect of heat treatment time on the crystallite size and lattice strain of C12A7 for a heat treatment temperature of 1100 °C</b>	136
<b>Figure 4.17 High-temperature X-ray diffraction patterns of the dried gel in a temperature range of 700-1200 °C</b>	137
<b>Figure 4.18 TGA-DSC plots versus temperature for the dried gel during heat treatment at a heating rate of 10 °C/min. A positive heat flow indicates an exothermic process and vice versa.</b>	139
<b>Figure 4.19 Derivatives of weight percent and heat flow versus temperature for the dried gel during heat treatment at a heating rate of 10 °C/min. A positive heat flow rate indicates an exothermic process.</b>	140
<b>Figure 5.1 FTIR-ATR spectrum of the as-prepared thin film before the crystallization heat</b>	143

- Figure 5.2** FTIR-ATR spectrum of the thin film after heat treatment at 1100 °C for 4 hr under air atmosphere. The structure mainly consists of C5A3. The reference spectrum [144] is obtained from a C5A3 sample synthesized through a melt-solidification process at 1600 °C in a carbon crucible under the flow of argon. 147
- Figure 5.3** Schematic configuration diagrams of Ca polyhedra in (a) crystalline C12A7, and (b) crystalline C5A3 [146] 148
- Figure 5.4** FTIR-ATR spectrum of the thin film treated at 1100 °C initially for 4 hr and then for a further 5 hr under air atmosphere. The structure consists of C5A3 and C12A7. The reference spectrum [144] is obtained from an originally C12A7 bulk which was heat treated at 1300 °C under a vacuum atmosphere and consists of a C12A7-C5A3 mixture. 149
- Figure 5.5** FTIR-ATR spectrum of the thin film initially heat treated at 1100 °C for 4 hr and then at 1300 °C for 2 hr under an air atmosphere. The structure consists mainly of C3A and C5A3. The reference spectrum [21] is obtained from a C3A bulk which was synthesized through a self-combustion technique. 151
- Figure 5.6** FTIR-ATR spectrum of the thin film after heat treatment at 1300 °C for 2 hr under air atmosphere. The structure mainly consists of C12A7. 152
- Figure 5.7** FTIR-ATR spectra of the C12A7 thin film in the as-prepared state and after heat treatment at 1300 °C for 2 hr under a 5%H<sub>2</sub>-95%N<sub>2</sub> atmosphere. The vibration bands shift towards higher frequencies after H<sub>2</sub> treatment. 156
- Figure 5.8** FTIR-ATR spectra of the C5A3 thin film in the as-prepared state and after heat treatment at 1300 °C for 2 hr under a 5%H<sub>2</sub>-95%N<sub>2</sub> atmosphere. The vibration bands have remained in the original positions. 158
- Figure 5.9** Raman spectrum of the dried gel before the crystallization heat treatment 159

<b>Figure 5.10 Raman spectrum of C12A7 powder obtained from the heat treatment of the dried gel at 1300 °C for 4 hr. The reference spectrum [144] is from a crystalline C12A7 bulk which was prepared by a melt-solidification process at 1500 °C in a dry oxygen atmosphere.</b>	162
<b>Figure 5.11 Raman spectra of the secondary phases, CA and C3A, which were formed during the solid-state reaction treatment of the powder. The Raman spectrum of C12A7 is also obtained from the powder.</b>	163
<b>Figure 5.12 Raman spectrum of the drop-casted film after a heat treatment at 1100 °C for 4 hr in air atmosphere. The reference spectrum [144] is obtained from a crystalline C5A3 bulk which was prepared by a melt-solidification process at 1500 °C in an atmosphere of argon.</b>	164
<b>Figure 5.13 Raman spectrum of the drop-casted film after a heat treatment at 1300 °C for 2 hr in air atmosphere. The reference spectrum [144] is obtained from a crystalline C12A7 bulk which was prepared through a melt-solidification process at 1500°C in a dry oxygen atmosphere.</b>	165
<b>Figure 6.1 Absorbance spectrum of C12A7 thin film</b>	169
<b>Figure 6.2 Band structure of C12A7 [50]</b>	170
<b>Figure 6.3 UV-visible optical properties of C12A7 thin film</b>	172
<b>Figure 6.4 Calculated values of refractive index and extinction coefficient as functions of wavelength for C12A7 thin film</b>	173
<b>Figure 6.5 Real and imaginary parts of the complex dielectric constant as functions of wavelength for C12A7 thin film</b>	174
<b>Figure 6.6 Refractive index of C12A7 thin film as a function of the square of the photon energy. The inset shows the values of the refractive index below the band gap energy and the fitted straight line.</b>	175
<b>Figure 6.7 Plot of <math>1/(n^2-1) - (hv)^2</math> for C12A7 thin film. The inset shows a linear relationship below the absorption edge of the material.</b>	177
<b>Figure 6.8 Plot of the second derivative of the absorption coefficient with respect to photon energy in Tauc region</b>	180



<b>Figure 6.9</b> $(\alpha h\nu)^{1/r}$ plot versus $h\nu$ for $r = 0.5$ . The plot shows a linear relationship in the photon energy range of $\sim 4.2$ to $4.6$ eV.	181
<b>Figure 6.10</b> Semi-logarithmic plot of the absorption coefficient as a function of photon energy for C12A7 thin film	184
<b>Figure 6.11</b> Semi-logarithmic plots of the absorption coefficient as functions of photon energy in the Urbach region in a temperature range of $25$ to $300$ °C	186
<b>Figure 6.12</b> Temperature dependency of the Urbach energy and the fitted models proposed by Cody and Yang. The first model by Cody represents the dependency of the Urbach energy on the phonon energy (equation 6.20) while the second model is based on the Einstein temperature (equation 6.23).	188
<b>Figure 6.13</b> Steepness parameter of C12A7 thin film as a function of $T^{-2}$ and the fitted Taylor's series approximation	191
<b>Figure 6.14</b> Temperature dependency of the steepness parameter and the fitted model represented by Urbach. Taylor's series fitting is an approximation to the Urbach's model.	192
<b>Figure 6.15</b> Temperature dependency of the band gap energy and the fitted models proposed by Manoogian-Woolley, Varshni and Bose-Einstein	193
<b>Figure 6.16</b> Relationship between the band gap energy and Urbach energy obtained at different temperatures	195

## List of Tables

<b>Table 2.1 Structural parameters of C12A7 [14, 26]</b>	30
<b>Table 2.2 Summary of the migration mechanisms of the extra-framework oxygen ions near the inter-cage opening and the calculated activation energies [12]</b>	36
<b>Table 3.1 Molar ratios of the ingredients used for sol preparation. The ratios marked with * belong to the molar ratios of isopropyl alcohol; while methanol is used as the solvent in the rest of the solutions.</b>	91
<b>Table 4.1 Molar ratios and the total weight for the improved solution recipe</b>	125
<b>Table 4.2 Elemental analysis of C12A7 thin films using energy dispersive spectroscopy</b>	126
<b>Table 4.3 Binding energy peaks and the phases formed in the dried gel and the crystallized thin film</b>	128
<b>Table 4.4 D-spacings and the lattices indices of the dominant reflections of C12A7 [129] for the dried gel after a heat treatment at 1300 °C for 6 hr. The angles marked with * and ** belong to the diffraction angles of CA [130] and C3A [131] phases respectively.</b>	133
<b>Table 4.5 Results of DSC-TGA analysis in a temperature range of 25-1200 °C at a heating rate of 10 °C/min</b>	140
<b>Table 5.1 FTIR-ATR absorption bands and the vibrational assignments for the spin-coated films before the crystallization heat treatment</b>	144
<b>Table 5.2 Vibration frequencies of isolated and bonded Al-O octrahedra and tetrahedra [147, 148]</b>	154
<b>Table 5.3 Raman absorption bands and the vibrational assignments for the dried gel before the crystallization heat treatment</b>	159
<b>Table 5.4 Comparison between the results of the spectral analyses for similar Raman-active and FTIR-active peak positions</b>	161
<b>Table 5.5 Raman and FTIR peak positions for C12A7 thin films. The related symmetry and origin of the peaks [26] are also included.</b>	166

<b>Table 6.1 Calculated values of the single-effective oscillator and Cauchy-Sellmair model parameters</b>	177
<b>Table 6.2 Values of band gap energy obtained from the optical absorption spectrum and tauc's law</b>	181
<b>Table 6.3 Fitting parameters of the Urbach energy-temperature models proposed by Urbach, Cody and Yang</b>	189
<b>Table 6.4 Fitting parameters of the band gap energy-temperature models proposed by Manoogian-Woolley, Varshni, and Bose-Einstein</b>	194
<b>Table 6.5 Fitting parameters of the band gap energy-Urbach energy model proposed by Cody</b>	196

## List of Symbols and abbreviations

$\alpha$	Absorption coefficient
$\epsilon^*$	Complex dielectric constant
$\Theta_D$	Debye temperature
$\Theta_E$	Einstein temperature
$\kappa$	Extinction coefficient
$\sigma$	Steepness parameter
<b>ASB</b>	Aluminium sec-butoxide
<b>ATR</b>	Attenuated total reflectance
<b>BEI</b>	Back-scattered electron imaging
<b>C12A7</b>	$12\text{CaO} \cdot 7\text{Al}_2\text{O}_3$
<b>C12A7:F<sup>-</sup></b>	Fluoride- incorporated $12\text{CaO} \cdot 7\text{Al}_2\text{O}_3$
<b>C12A7:ITO</b>	$12\text{CaO} \cdot 7\text{Al}_2\text{O}_3$ -doped indium tin oxide
<b>C12A7:OH<sup>-</sup></b>	Hydroxide- incorporated $12\text{CaO} \cdot 7\text{Al}_2\text{O}_3$
<b>C12A7 : O<sup>-</sup> + O<sub>2</sub><sup>-</sup></b>	Superoxide- incorporated $12\text{CaO} \cdot 7\text{Al}_2\text{O}_3$
<b>C12A7: O<sup>2-</sup></b>	Oxide- incorporated $12\text{CaO} \cdot 7\text{Al}_2\text{O}_3$
<b>C3A</b>	$3\text{CaO} \cdot \text{Al}_2\text{O}_3$
<b>C5A3</b>	$5\text{CaO} \cdot 3\text{Al}_2\text{O}_3$
<b>CA</b>	$\text{CaO} \cdot \text{Al}_2\text{O}_3$
<b>CCB</b>	Cage conduction band
<b>DSC</b>	Differential scanning calorimetry
$E_g$	Band gap energy
$E_U$	Urbach energy
<b>EAA</b>	Ethyl acetoacetate

<b>EDS</b>	Energy dispersive spectroscopy
<b>FCB</b>	Framework conduction band
<b>FESEM</b>	Field-emission scanning electron microscope
<b>FTIR</b>	Fourier transform infrared spectroscopy
<b>IR</b>	Infrared
<b>M<sup>0</sup></b>	Metal atom
<b>M/M<sup>+</sup></b>	Metal ion
<b>Me</b>	Methyl group
<b>OLED</b>	Organic light-emitting diode
<b>SEI</b>	Secondary electron imaging
<b>SEM</b>	Scanning electron microscope
<b>TCO</b>	Transparent conductive oxide
<b>TGA</b>	Thermal gravimetric analysis
<b>UV</b>	Ultraviolet
<b>UV-Vis</b>	Ultraviolet-visible
<b>VB</b>	Valence band
<b>XPS</b>	X-ray photoelectron spectroscopy
<b>XRD</b>	X-ray diffraction
<b>YSZ</b>	Yttria stabilized zirconia

# Chapter One

## Introduction

Recent developments in the field of thin-film-based optoelectronic devices, such as thin film transparent transistors and solar cells, have led to an increasing interest in the fabrication of high quality thin films of insulating, semiconducting and conducting types, offering a high efficiency and improved chemical stability in different environments.

$12\text{CaO}\cdot 7\text{Al}_2\text{O}_3$ , or C12A7, has been widely known for several years as one of the main constituents of Portland cements. The unique crystal structure of this refractory oxide, however, has only recently been fully understood. The lattice structure of this compound is built up of nano-sized empty cages which can randomly incorporate negatively charged species, such as  $\text{O}^{2-}$ ,  $\text{O}^-$ ,  $\text{O}_2^{2-}$ ,  $\text{OH}^-$  and even electrons, in order to compensate for the extra positive charge of the lattice [1]. The material exhibits different physical properties depending on the type of incorporated anions without a significant change in the structure of the lattice. C12A7 has gained much attention for potential applications in various fields, such as ion conducting solid electrolyte, reducing agent, cold-cathode electron

field emitter, oxidizing catalyst, ion emitter, and as a transparent conductive oxide (TCO) in flat panel displays, solar cells and transparent transistors [2, 3]. Optical transparency, chemical stability under air atmosphere and at room temperature, ionic and electronic conductivity, and natural abundance are some of the properties of this compound which are highly desired.

The application of C12A7 in oxide-based electronic devices has led to a rising demand for a cost effective fabrication of high quality oxide thin films. While the fabrication of C12A7 single crystal and polycrystalline bulk has been studied extensively during the last few years, detailed investigation on the preparation of C12A7 thin films is rather limited. Two fabrication techniques, which have been previously suggested for the preparation of C12A7 thin films, include pulsed laser deposition [4] and sol-gel method. The former technique is relatively costly and requires a C12A7 target as the starting material for the deposition of the film, while obtaining a continuous defect-free film with a high critical thickness using sol-gel technique is found to be quite challenging [5].

This thesis reports a significantly improved sol-gel derived fabrication technique for the production of high quality thin films of the refractory oxide,  $12\text{CaO}\cdot 7\text{Al}_2\text{O}_3$ , and an in-depth investigation into the physical properties of the films on magnesium oxide substrates. Continuous defect-free thin films of single phase C12A7 have been achieved by optimizing the sol-gel fabrication technique in relation to microstructural, structural and crystalline properties. This thesis has been organized into seven chapters.

The following chapter starts with a critical review of the theoretical studies on the atomic and electronic structures of the anion/electron incorporated C12A7.

The physical properties of the compound are then discussed followed by experimental techniques for the preparation of C12A7 in form of single crystal, bulk and thin film with the main emphasis on sol-gel technique, as well as suggested processes for the incorporation of anions/electrons into the structure of the material. Some of the main potential applications of C12A7 are briefly introduced in the last section of this chapter.

Chapter 3 describes the sample preparation technique employed in this research via sol-gel process. A simple and straight-forward procedure for the preparation of the solution is introduced. All the instruments and technical specifications used for microstructural observations, chemical composition analyses and absorption spectral analyses are presented in this chapter.

Chapter 4 focuses on the microstructural observations of the thin film surfaces and the effect of the solution ingredients on the quality of the films. Optimization protocols for the sol-gel process have been explained suggesting an optimum solution recipe. The elemental and phase analysis of the products in form of powder and thin films are then presented and the effect of processing parameters on the formation of single-phase C12A7 are examined in detail.

The results of Fourier transform infrared spectroscopy (FTIR) and Raman spectroscopy are presented in chapter 5. A direct characterization of the thin films was found to be exceptionally challenging due to the small thickness of the films compared to that of the substrate. The infrared spectral analysis of the films using a recently developed technique, based on total attenuated reflectance, provided promising results regarding the phase analysis of the films. A detailed



FTIR spectral analysis of C12A7 ultra-thin films has not been reported elsewhere up to our knowledge.

Chapter 6 provides a detailed investigation on the optical properties of C12A7 films at room and high temperatures. The optical parameters of the films, including the Urbach energy and band gap energy, have been determined as a function of temperature. The experimental results have been interpreted in terms of theoretical models in order to evaluate the best relationship which can explain the optical behaviour of C12A7 at different temperatures.

The thesis is finally concluded with giving a summary in chapter 7 of the main observations and an outline of the future work.

# Chapter 2

## Literature Review

### 2.0 Introduction

In this chapter, the properties and applications of the refractory oxide  $12\text{CaO}\cdot 7\text{Al}_2\text{O}_3$  are presented. The atomic structure, as well as the physical and optical properties of the material, is explained in detail. The fabrication of this oxide via sol-gel method and the effect of subsequent heat treatment processes on the physical and optoelectronic properties of C12A7 are introduced. The potential applications of the material in various chemical and electronic fields are mentioned in the last section of this chapter.

### 2.1 Structural and physical properties of C12A7

#### 2.1.1 Atomic structure

Calcium-alumina binary compound,  $12\text{CaO}\cdot 7\text{Al}_2\text{O}_3$  or C12A7, is one of the main constituents of calcium aluminate cements. This complex oxide, also known by the name mayenite in the cement industry, is an intermediary stable

phase in the CaO-Al<sub>2</sub>O<sub>3</sub> binary system [6]. It is chemically stable up to high temperatures with the melting point of 1415 °C, and therefore, considered as a refractory oxide [1, 7, 8, 9]. The position of this compound in the CaO-Al<sub>2</sub>O<sub>3</sub> binary diagram is shown in figure 2.1.

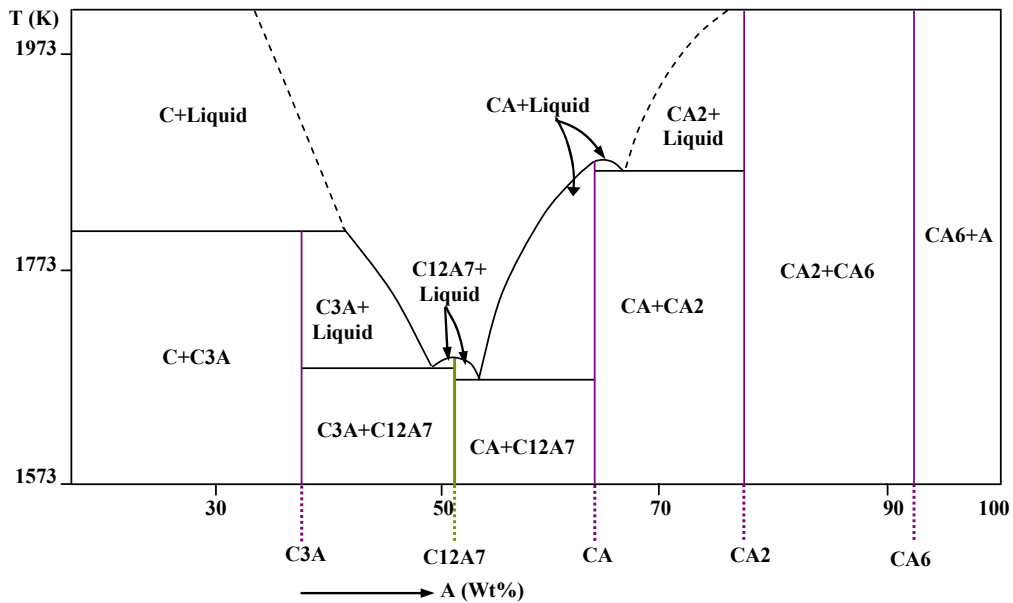


**Figure 2.1** Position of C12A7 compound in the binary phase diagram of CaO-Al<sub>2</sub>O<sub>3</sub> [10]

The body centred cubic unit cell of C12A7 is comprised of two 12CaO.7Al<sub>2</sub>O<sub>3</sub> molecules with a lattice constant of 1.989 nm [11]. The stoichiometric chemical composition of the unit cell is represented as [Ca<sub>24</sub>Al<sub>28</sub>O<sub>64</sub>]<sup>4+</sup>.2O<sup>2-</sup> in which [Ca<sub>24</sub>Al<sub>28</sub>O<sub>64</sub>]<sup>4+</sup> is the positively charged framework with 12 sub-nanometer-sized cages [1, 7, 12], shown in figure 2.2(a). This means that each cage has a mean charge of +1/3. In order to compensate for the positive charge of the framework, two O<sup>2-</sup> oxygen ions are incorporated in each unit cell and distributed randomly inside 2 out of 12 cages [1]. These oxygen ions are held in place by the positive charge of the cage wall and are not bonded to any specific atom [13]. They are named as "extra-framework" or

"free" oxygen ions to distinguish them from the framework oxygen ions located at the cage wall [13]. The empty cages have a concentration of approximately  $5 \times 10^{21} \text{ cm}^{-3}$ , each with an empty space of around 0.6 nm in diameter [14, 15]. An empty cage consists of 16 oxygen ions, 8 tetrahedral aluminium ions and 6 octahedral calcium ions (figure 2.2(b)) and is directly connected to 12 neighbouring cages [16].

C12A7 is considered to have an anti-zeolite-type of framework [2, 18]. The difference between C12A7 and zeolite is that in zeolite, cations are introduced into the structure to compensate for the extra negative charge of the lattice caused by the substitution of  $\text{Si}^{4+}$  with  $\text{Al}^{3+}$ , but in C12A7, monovalent anion species substitute for the free oxygen ions and stabilize the structure [19, 20]. The framework of C12A7 contains  $\text{AlO}_4$  tetrahedra forming eightfold rings, i.e. it is considered as an aluminate framework rather than a calcium aluminate framework (which is often mentioned in the literature). A random distribution of calcium and free oxygen ions causes a short-range distortion of this framework [8, 21].

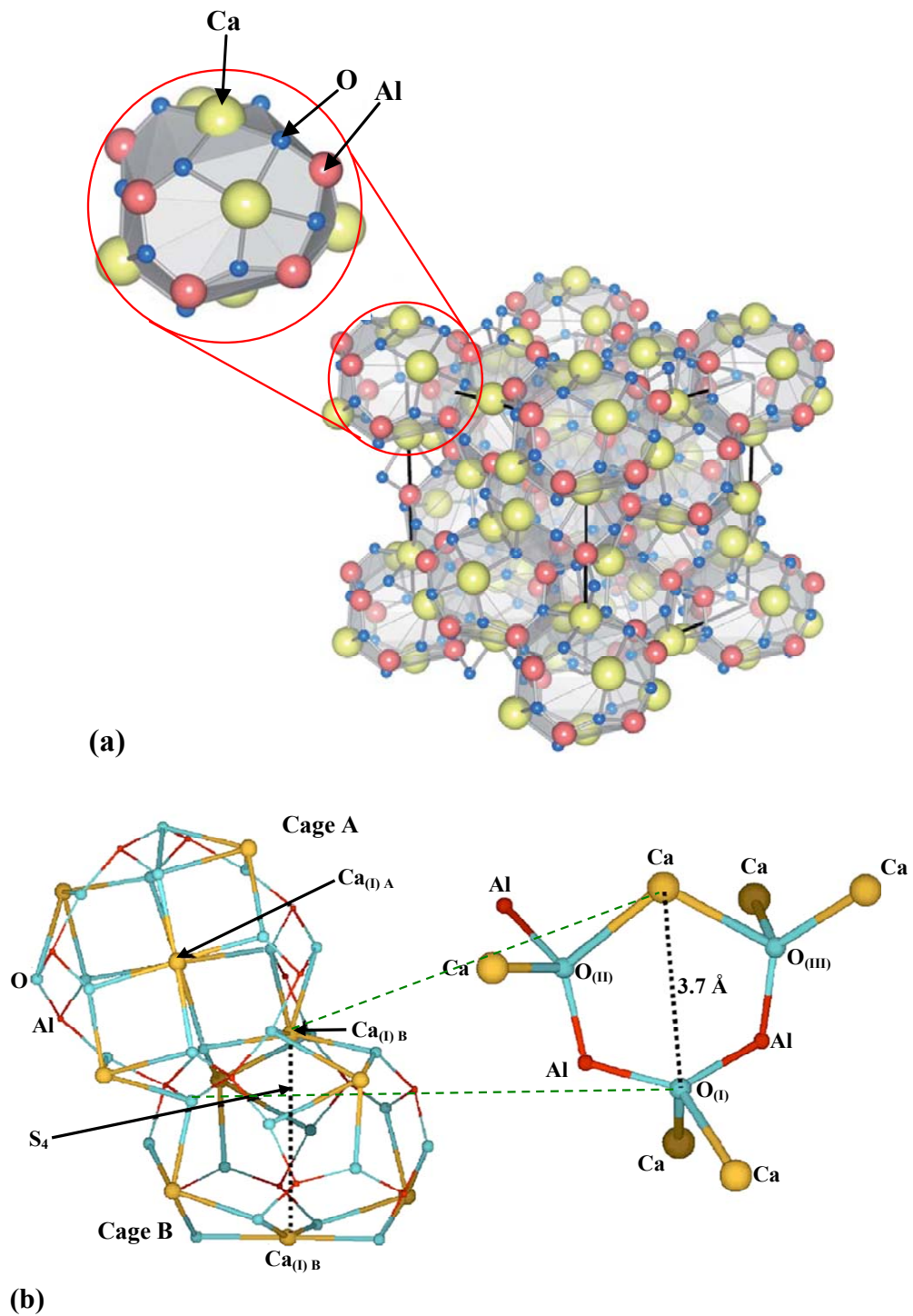
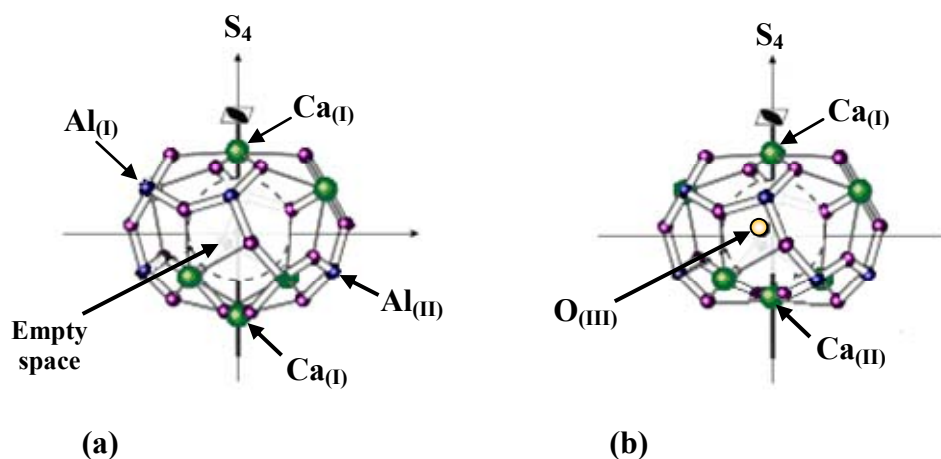


Figure 2.2 Schematic structures of C12A7 (a) unit cell [17], (b) the connection between two neighbouring cages via the cage opening [12]. Cage A and B are shown from the top and side views respectively.

The framework structure of C12A7 and the distortion of the lattice via the introduction of extra-framework oxygen ions have been previously studied. The

schematic structures of an empty and occupied cage based on neutron powder diffraction studies are shown in figure 2.3.



**Figure 2.3** Schematic structures of (a) an empty cage and (b) an occupied cage filled with an  $O^{2-}$  ion. Upon  $O^{2-}$  occupation, one of the  $Ca^{2+}$  ions displaces towards the centre of the cage along the  $S_4$  axis.  $O_{(III)}$  state is the position of extra-framework  $O^{2-}$  ion inside the cage [25].

The line connecting the two  $Ca_{(I)}$  ions positioned at the cage wall is the  $S_4$  symmetry axis [12]. In the absence of the extra-framework oxygen ions, the 12 empty cages of the unit cell form 3 groups of 4, each with  $S_4$  symmetry axes along x, y and z crystallographic axes [22]. The nature of the bonding between the cage-wall species is different for Al-O and Ca-O bonds. The bonding between the framework  $O^{2-}$  ion and  $Al^{3+}$  ion has a covalent nature, but the bonding between the framework  $O^{2-}$  and  $Ca^{2+}$  ions is strongly ionic [23]. When  $O^{2-}$  ion is introduced into the cage, one of the two  $Ca^{2+}$  ions is displaced from the original position,  $Ca_{(I)}$ , to the new position,  $Ca_{(II)}$ , with the other  $Ca^{2+}$  ion remaining near the original site  $Ca_{(I)}$ . The introduced  $O^{2-}$  ion occupies a state in the middle of the two Ca states [23] with an inter-ionic distance of 1.5 times the sum of their radius [24]. As a result, the  $S_4$  symmetry of the cage is only partly

preserved [12]. The reason for the loss of symmetry is that the extra-framework oxygen ion can be positioned at one of the four equivalent 48e sites, which are all displaced from both the centre of the cage and the  $S_4$  axis [14]. The position of the free oxygen ion is affected by the presence of  $Al^{3+}$  ions as well as six  $Ca^{2+}$  ions at the cage wall, hence causing the displacement from the  $S_4$  axis [9, 14, 19]. The off-centre shift of the free oxygen ions inside the cages increases with increasing temperature [8].

The two different positions of polar  $Ca^{2+}$  ions,  $Ca_{(I)}$  and  $Ca_{(II)}$ , are separated by an approximately 0.06 nm distance. The  $Ca_{(II)}$  position has two equivalent sites around the  $S_4$  axis and the occupation of these sites depends on which of the four available 48e crystallographic sites inside the cage has been occupied by the free oxygen ion [14]. The structural parameters of C12A7, including the coordinates and occupancies of the atoms in C12A7, are listed in table 2.1.

**Table 2.1 Structural parameters of C12A7 [14, 26]**

<i>Atom</i>	<i>Site</i>	<i>Coordinates</i>			<i>Occupancy</i>	<i>Type</i>
		<i>x</i>	<i>y</i>	<i>z</i>		
Ca	24d	0	0.25	0.1397	1	Framework
$Al_{(I)}$	16c	0.0187	0.0187	0.0187	1	Framework
$Al_{(II)}$	12b	-0.125	0	0.25	1	Framework
$O_{(I)}$	48e	0.151	-0.037	0.057	1	Framework
$O_{(II)}$	16c	-0.064	-0.064	-0.064	1	Framework
$O_{(III)}$	48e	0.337	0	0.25	0.083	Extra-framework

Although the introduction of an oxygen ion into a cage induces a slight displacement of all the ions at the cage wall, the displacement of the framework

$O^{2-}$  and  $Al^{3+}$  ions is mostly limited to thermal vibrations. However, the displacement of  $Ca^{2+}$  ions is more significant. The reason is that the inner face of  $Ca^{2+}$  ions inside the cage is not concealed by the framework  $O^{2-}$  ions, and therefore, it is exposed to the extra-framework ions being electrostatically attracted to them [2,23].

There are two types of  $Al^{3+}$  ions at the cage wall.  $Al_{(I)}$  is coordinated by one non-bridging oxygen ion,  $O_{(I)}$ , and two bridging oxygen species,  $O_{(II)}$ , with  $C_3$  symmetry axis. Non-bridging oxygen ions are bonded to one  $Al^{3+}$  ion only, and the bridging oxygen species are coordinated with two  $Al^{3+}$  ions.  $Al_{(II)}$  ion is bonded with four oxygen ions, all of which are bridging type with  $S_4$  symmetry axis [25, 26].

Each of the two neighbouring cages is joined via an intercage opening [12, 27]. The intercage opening (figure 2.2(b)) is a hexagonal ring including  $Ca_{(I)}-O_{(I)}-Al_{(II)}-O_{(I)}-Al_{(I)}-O_{(II)}$  with the diameter of around 0.1 nm which should theoretically facilitate the diffusion of the species with similar or less diameters [7, 12]. Each of the oxygen ions located at the opening is connected to four cations: two in the same plane of the opening and two in the plane approximately perpendicular to the plane of the opening [12].

The cage structure of each cage in C12A7 is comparable to CaO with rock salt structure. In CaO, six  $Ca^{2+}$  ions form a regular octahedral structure with  $O_h$  symmetry. In C12A7, however, the six  $Ca^{2+}$  ions form a distorted octahedral crystallographic structure with  $S_4$  symmetry and therefore, the distance between  $Ca^{2+}$  and extra-framework  $O^{2-}$  ions is more than the separation distance in CaO, making  $O^{2-}$  ions loosely bound to the cage [25].



Two stable calcium aluminate phases in the calcia-alumina binary system with closest chemical compositions to C12A7 are CaO.Al<sub>2</sub>O<sub>3</sub> (CA) and 3CaO.Al<sub>2</sub>O<sub>3</sub> (C3A). The position of these two phases with respect to C12A7 is shown in figure 2.1. CA has a metastable orthorhombic unit cell ( $a = 8.744 \text{ \AA}$ ,  $b = 8.093 \text{ \AA}$ ,  $c = 15.148 \text{ \AA}$ ), which is formed at medium temperatures. The enthalpy of crystallization of the orthorhombic phase is reported to be 25 kJ/mol. This metastable phase is initially formed due to the kinetically limited crystallization at lower temperatures. As the temperature is further increased, however, the metastable phase lowers its free energy by progressing towards the formation of stable monoclinic phase [6], which is built up of a framework of cornered joint AlO<sub>4</sub> tetrahedra [28] with lattice parameters of  $a = 8.693 \text{ \AA}$ ,  $b = 8.076 \text{ \AA}$ ,  $c = 15.178 \text{ \AA}$  and  $\beta = 90.17^\circ$  [6] and p2/n space group [28].

CA contains less weight percent of calcium oxide compared to C12A7. C3A, on the other hand, is a Ca-rich stable phase with a cubic unit cell ( $a = 15.263 \text{ \AA}$ ) and space group Pa3. Each unit cell consists of 72 Ca, 48 Al and 144 O atoms. The structure is built up of sixfold hollow rings of distorted AlO<sub>4</sub> tetrahedra (Al<sub>6</sub>O<sub>18</sub>). Each unit cell contains 80 rings, 72 of which are filled with Ca atoms [28]. The formation of C12A7 is sometimes accompanied by the simultaneous formation of CA and/or C3A as secondary phases. The effect of heat treatment temperature and duration on the formation of CA and C3A alongside C12A7 in powder and thin films will be discussed further in chapters 4 and 5.

### **2.1.2 Thermal stability**

The thermal stability of C12A7 is only preserved under normal air and oxygen atmospheres [2, 29]. The presence of oxygen during the heat treatment promotes

the crystallization of the compound [29]. The framework is not stable at high temperatures in a reducing atmosphere [2] or a dry atmosphere of inert gas [30]. Solidification of the melt in a reducing atmosphere leads to the production of C5A3-C3A mixture below 1500 °C and CA-C3A mixture when cooling down from above 1600 °C [2]. Vacuum annealing at temperatures higher than 1100 °C also results in the decomposition of this compound [31].

The heat treatment of C12A7 in a moist atmosphere between ~ 900 – 1050 °C [30, 32] results in the absorption of water in form of OH<sup>-</sup> species into the cages forming Ca<sub>12</sub>Al<sub>14</sub>O<sub>32</sub>(OH)<sub>2</sub> rather than the stoichiometric Ca<sub>12</sub>Al<sub>14</sub>O<sub>33</sub>. The incorporation of OH<sup>-</sup> ions does not change the cage structure of the framework [33, 34]. However, it has been suggested that the non-stoichiometric compound should not be considered as part of the CaO-Al<sub>2</sub>O<sub>3</sub> binary system [6]. The structure may contain from 1.30 to 1.40 wt% of water when heat treated in an atmosphere with normal humidity [21, 34]; although this phenomenon is reversible and a heat treatment in dry oxygen atmosphere leads to the release of OH<sup>-</sup> ions from the cages [20].

C12A7 exhibits high stability against energetic ion irradiation due to the ability of free oxygen ions to fill the framework oxygen vacancies that might form during irradiation and hence preserve the original lattice structure [7, 12].

The concentration of free oxygen ions is dependent upon temperature [8]. This amount often exceeds the stoichiometric value at room temperature due to the presence of peroxide, superoxide and hydroxide ions, such as OH<sup>-</sup>, O<sub>2</sub><sup>-</sup>, O<sub>2</sub><sup>2-</sup> and O<sup>-</sup>, giving the most stable composition of Ca<sub>12</sub>Al<sub>14</sub>O<sub>33.53</sub>. As the temperature increases, however, the excess oxygen radicals deform into O<sup>2-</sup> ions under a

vacuum atmosphere and are eliminated from the structure [8, 14]. At high enough temperatures (700°C and higher), the stoichiometric concentration of extra-framework oxygen species can be obtained [8].

### 2.1.3 Ionic conductivity and mechanisms of oxide-ion migration

C12A7 has high oxide ion conductivity in a temperature range of  $\sim 500-1200$  °C [35]. A typical ionic conductivity of  $\sim 0.016$  S.cm<sup>-1</sup> has been reported for this material at 900 °C which is only about an order of magnitude lower than that of the well-known electrolyte based on yttria- stabilized zirconia [8, 12, 32, 35- 37].

The migration of free oxygen ions requires an increase in the temperature and occurs via a hopping mechanism or tunnelling at higher temperatures [14]. The diffusion of O<sub>2</sub><sup>-</sup> is slow compared to that of O<sup>2-</sup> due to its high activation energy. The diffusion of O<sup>-</sup> ions, on the other hand, is faster than O<sup>2-</sup> species [12]. If held in a dry oxygen atmosphere, the compound shows even higher ionic conductivity compared to the stoichiometric material due to the incorporation of O<sup>-</sup> ions inside the structure and the higher mobility of this species compared to O<sup>2-</sup> ions [35]. A conductivity of  $5 \times 10^{-4}$  S.cm<sup>-1</sup> has been reported for C12A7 at  $\sim 300$  °C under an oxidizing atmosphere (P<sub>O<sub>2</sub></sub>  $\sim 1$  atm). The conductivity further increases with increase in temperature reaching its maximum of 0.05 S.cm<sup>-1</sup> near the melting point of the compound [35, 38].

Theoretical investigations, based on quantum mechanical calculations and embedded-cluster approach, have shown that the diffusion of O<sup>2-</sup> species involves a simultaneous displacement of four ions, known as *the exchange*

*mechanism*. The migration path of an extra-framework oxygen species from one cage to another is schematically illustrated in figure 2.4.

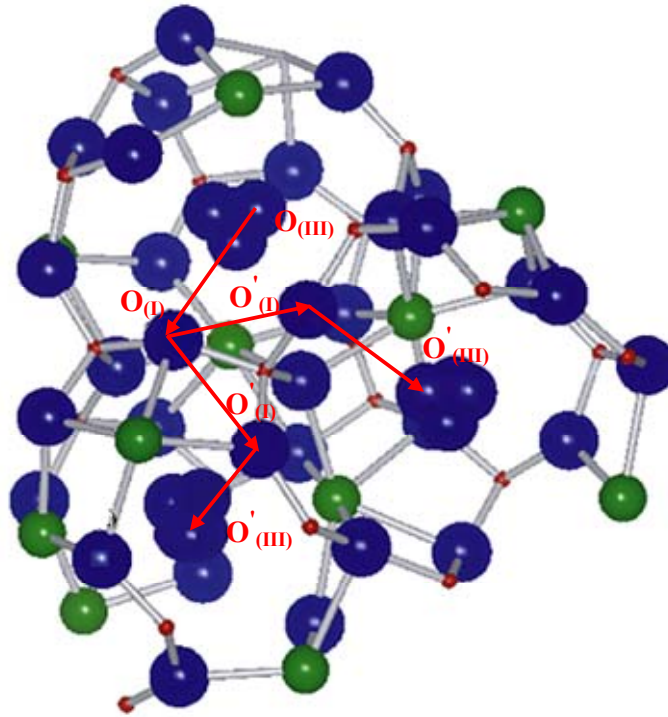


**Figure 2.4 Two possible routes for the migration of an extra-framework  $O^{2-}$  ion from one cage to another involving crystallographic states  $O_{(III)}-O_{(II)}-O'_{(II)}-O'_{(III)}$  [14]**

At the beginning of the diffusion, the extra-framework oxygen substitutes a framework oxygen ion nearby. Since there are three oxygen ions with different crystallographic states at the cage opening, there are three possible pathways for the extra-framework oxygen to replace the framework ion. During the next step, the displaced oxygen ion exchanges its position with a framework oxygen ion which is closer to an empty state in a neighbouring cage. The last stage of the diffusion includes the occupation of the displaced oxygen ion in the empty state of the second cage [12]. Taking into account the distances between the cage-wall oxygen ions and the free oxygen ion, the most likely pathway for the migration is believed to be the substitution of a framework oxygen ion in the

O<sub>(I)</sub> state with a free oxygen, which then replaces the O'<sub>(I)</sub> state in a neighbouring cage and migrates to the empty space inside the second cage. This pathway involves the movement of four oxygen ions [14]. It should be noted that a much more complex exchange mechanism might occur in reality and the given explanation is simplified in order to understand the basics of oxygen diffusion in the structure [12].

The energy needed for the migration of oxygen ion via exchange mechanism is much smaller than the energy required for *the interstitial mechanism*, i.e. the movement of an extra-framework ion directly in between the cages through the cage opening. Hence, the latter mechanism is unlikely to happen and an exchange mechanism is found to be the dominant mechanism for O<sup>2-</sup> ion diffusion [8, 12, 14]. This means that in spite of having a nanoporous structure and large intercage openings, C12A7 still follows the same diffusion mechanism as other oxides, such as MgO, SiO<sub>2</sub> and HfO<sub>2</sub>. The possible diffusion pathways for the free oxygen species and the calculated activation energies for each type of migration mechanism are summarized in table 2.2.

**Table 2.2 Summary of the migration mechanisms of the extra-framework oxygen ions near the inter-cage opening and the calculated activation energies [12]**

Diffusion Mechanism	Activation Energy (eV)
Interstitial	1.7
Exchange via O <sub>(I)</sub>	1.9
Exchange via O <sub>(II)</sub>	1.2
Exchange via O <sub>(III)</sub>	1.0

## 2.2 Electronic structure of C12A7 and incorporation of ionic species

The incorporated oxygen ions in C12A7 structure can be replaced by other monovalent anions or even by electrons [1]. The maximum theoretical concentration of monovalent anions is  $2.32 \times 10^{21} \text{ cm}^{-3}$ , i.e. if all the  $\text{O}^{2-}$  ions are substituted with monovalent anions [20, 39]. The replacement of  $\text{O}^{2-}$  ions with monovalent species stabilizes the structure through charge delocalisation [20, 40].

The incorporation of a monovalent anion inside an empty cage causes the  $\text{Ca}^{2+}$  ions along the  $S_4$  symmetry axis to displace towards the centre of the cage, although this displacement is not as much as in the case of  $\text{O}^{2-}$  ion incorporation [15]. The larger distance between  $\text{Ca}^{2+}$  ions in a superoxide-ion incorporated cage is mainly due to the lower charge and higher ionic radius of the superoxide anions [2].

$\text{O}^{2-}$  ion produces the highest deformation of the cage structure compared to other species. All anions, except  $\text{O}^{2-}$ , occupy a state close to the centre of the cage along  $S_4$  axis and even  $\text{OH}^-$  ion is located at the centre with H oriented towards one of the cage-wall oxygen ions.  $\text{O}^{2-}$  anion is the only species that occupies an empty state displaced from the centre of the cage [15].

There are two types of conduction bands known for C12A7: one is *the framework conduction band* that is composed of Ca 5s orbitals. The second band, also known as *the cage conduction band*, is formed as a result of the overlap of the s-like states in empty cages and is located at around 2 eV below the framework conduction band [15, 41]. These states are not related to any of

the lattice atoms and can be defined as *the states of entrapped particles in a box* instead [15].

The electronic transitions for different types of anions are shown schematically in figure 2.5.

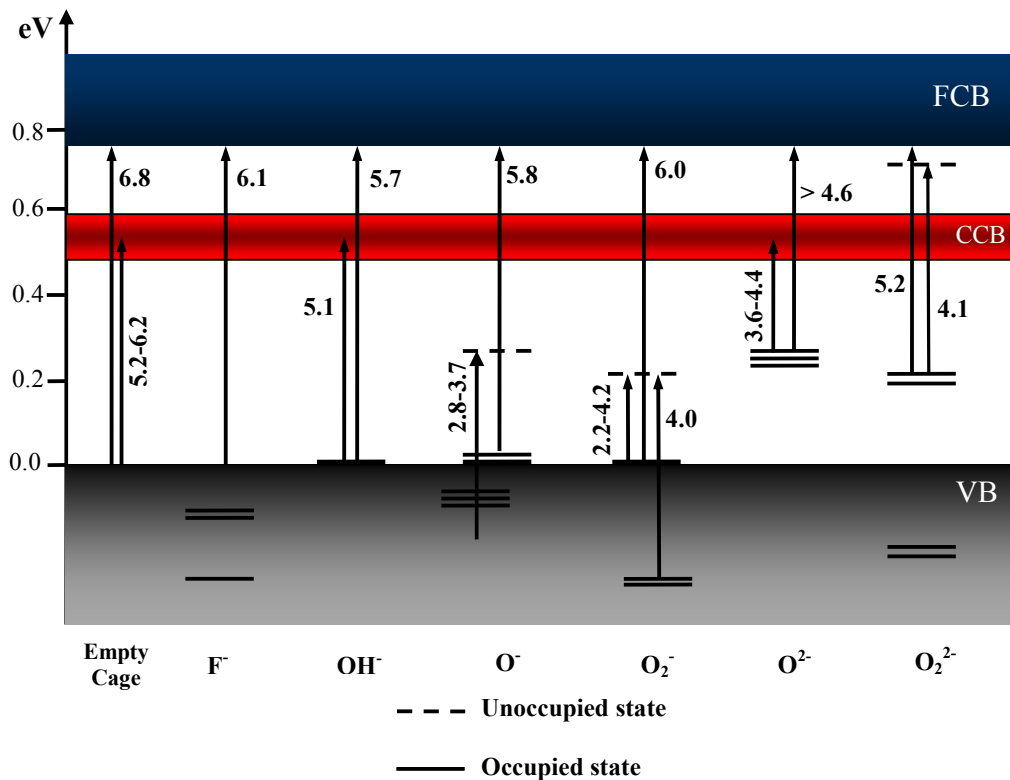


**Figure 2.5** Electronic transitions for C12A7 incorporated with different ionic species. The excitation energy for each transition is also given [15].

The excitation energy for each transition depends on the type of extra-framework species occupied inside the cages. Since the  $O^{2-}$  ion is located at a state which is displaced from the centre of the cage, the cage conduction band formed is different from that of the cages occupied with other types of species. The cage conduction band is not filled in the case of occupation with all types of species, except for the intrinsic  $O^{2-}$  and  $OH^-$  ions. The transition from the valence band to the cage conduction band occurs for empty cages only, and the

entrapped anions do not have an effect on the excitation energies of this type of transition. The transition from the valence band to the framework conduction band, however, is affected by the type and charge of the extra-framework species.

Three types of electronic transitions can occur in the case of  $O^{2-}$  ion incorporation: (i) occupied ion state to cage conduction band, (ii) occupied ion state to framework conduction band, and (iii) valence band to framework conduction band.

The energy levels of active oxygen ions are lower than that of  $O^{2-}$  ion, and a transition from these states to the framework conduction band is less likely to occur as it needs a high excitation energy. Hence, possible transitions for these anions are valence band to the unoccupied ion states and intra-molecular transitions from the occupied to the unoccupied states of each anion.

$O^-$  and  $O_2^-$  occupied states are positioned near the valence band, while  $O_2^{2-}$  has two separate occupied states located above the top of the valence band, and therefore, the excitation energy needed for the transition of this ion is lower. Another type of transition associated with active oxygen ions ( $O_2^{2-}$ ,  $O_2^-$  and  $O^-$ ) is the excitation from the 2p state of framework oxygen ions to the unoccupied states of the entrapped species.

The unoccupied state of  $O_2^{2-}$  is near the framework conduction band; therefore, a high excitation energy is needed for a transition from an occupied state to an unoccupied state. On the other hand,  $O_2^-$  has an unoccupied state close to the top of the valence band and the excitation energy for the transition is relatively low.



In the case of OH<sup>-</sup> occupation, two types of transitions can occur which correspond to (i) an electron transfer from the anion to the cage conduction band of a neighbouring cage, and (ii) a transition from an occupied state of OH<sup>-</sup> near the top of the valence band to the framework conduction band which causes an absorption edge shift of the material.

The presence of F<sup>-</sup> ion inside the cage changes the 2p states of the cage-wall oxygen ions and results in the upward shift of the top of the valence band to higher energy levels [15].

## **2.3 Electron-incorporated C12A7**

### **2.3.1 An introduction to C12A7 electride**

Electride is an ionic compound in which electrons act as anions [1]. Stabilization of the electrons inside the structure can lead to the fabrication of conductive materials with unusual optical or magnetic properties [7]. There are various kinds of applications for electrides including reducing agents, cold-cathode electron field emitters, thermionic power generators and refrigeration devices [1, 2, 7].

Electrides can be composed of organic or inorganic materials. Common electrides are alkali metal adducts of organic cage compounds or inorganic molecular sieves [7, 9, 40]. Most of the organic electrides are not stable at room temperature and degrade upon exposure to air or moisture [1, 2, 7]. Although there are a few recently-found organic electrides that are more stable under these conditions, the instability of organic electrides has generally limited their applications [1]. Various transparent transition and post-transition metal oxides,

such as indium-tin oxide (ITO), are made conductive via ion doping, but this technique cannot be utilized for the abundant transparent main-metal oxides [24].

Alumina and its complexes are also known to be good electrical insulators and their large band gap and strongly ionic bonding between cations and oxygen ions make them almost impossible to be transformed to conductors [42]. However, C12A7 can be converted to an electride due to its unique nanoporous cage structure. This compound has the advantage of chemical and thermal stability at room temperature [1, 2] and therefore can have various applications where a combination of optical transparency and electrical conductivity along with chemical stability is needed, such as flat panel displays and solar cells [2].

It is worth mentioning that according to the electride model, the electrons are highly localised inside the structure and act as anions. It has been suggested that for a low electron concentration in C12A7, the electrons follow the electride model, but as the concentration increases, the electrons are displaced from their original states and might not be strictly localised anymore. Therefore, a highly electron-incorporated C12A7 cannot be considered an electride due to delocalisation [2].

The introduction of electrons into the structure fills the cage conduction band and produces a persistent conductivity [27, 41, 43]. A high concentration of electrons in a material does not always guarantee an electrical conductivity; however, the electron-incorporated C12A7 is conductive mainly due to the presence of the cage conduction band below the framework conduction band [40].

The maximum number of electrons that can be accommodated inside the cages is  $2.33 \times 10^{21} \text{ cm}^{-3}$  theoretically [1, 24]. In reality, the concentration of electrons can exceed this value by optimizing the process parameters, such as the partial pressure of oxygen, and/or modifying the process such as the inclusion of additives in the melt [1]. C12A7 electride has been reported to have high chemical stability at temperatures up to  $300^\circ\text{C}$  [44] and a low work function of approximately 2.4 eV [17].

### 2.3.2 Atomic and electronic structure

Upon the introduction of electrons into the structure, the positively-charged cages act as trapping centres for electrons, similar to positive oxygen vacancies in some oxides. The properties of electrons in positively charged cages are comparable to the properties of electrons in anion vacancies or F centres. These defects can be neutral with respect to the lattice, like in alkali halides, or singly charged, such as  $\text{F}^+$  centre in MgO. Each electron inside the cage behaves like an anion with a spherical 1s wave function of an  $\text{F}^+$ -like centre and migrates as a polaron [7, 45, 44]. The main difference between the cages in C12A7 and  $\text{F}^+$  centres in other oxides is that these cages are part of the material structure and are available at much greater concentration compared to oxygen vacancies in other oxides.

The introduction of an electron inside a cage, and therefore the relaxation of the cage, is realised by the change of distance between the  $\text{Ca}_{(1)}$  ions at opposite sides of the cage. The distance between  $\text{Ca}_{(1)}$  ions in an empty cage is approximately 0.58 nm and it drops to 0.51 nm for an occupied cage, while other ions at the cage wall displace away from the cage centre. These

displacements are mainly caused by *polaron effect* and result in the stabilization of the electron inside the structure and lattice relaxation [23].

The distance between calcium ions inside electron-filled cages is larger than that of oxy-mayenite and the substitution of extra-framework oxygen ions with electrons results in the expansion of the unit cell. The thermal expansion coefficient of the electride is smaller than the one of oxy-mayenite [2].

A schematic illustration of the cage and framework conduction bands and the position of electrons states in C12A7 is shown in figure 2.6. The framework conduction band is approximately 7.0 eV above the valence band. The cage conduction band, due to s-like states of each empty cage, is located at  $\sim 5.4$  eV above the valence band. When the electrons occupy the cages, the level of the occupied electronic state drops as much as 0.6 to 1.1 eV as a result of cage relaxation. This occupied state is located at  $\sim 4.3$  eV above the top of the valence band, although the distance can vary according to thermal fluctuations, the average distance from the occupied cages, and the effect of other entrapped electrons [23]. The presence of oxygen ion species inside the structure also affects the top of the valence band [43].

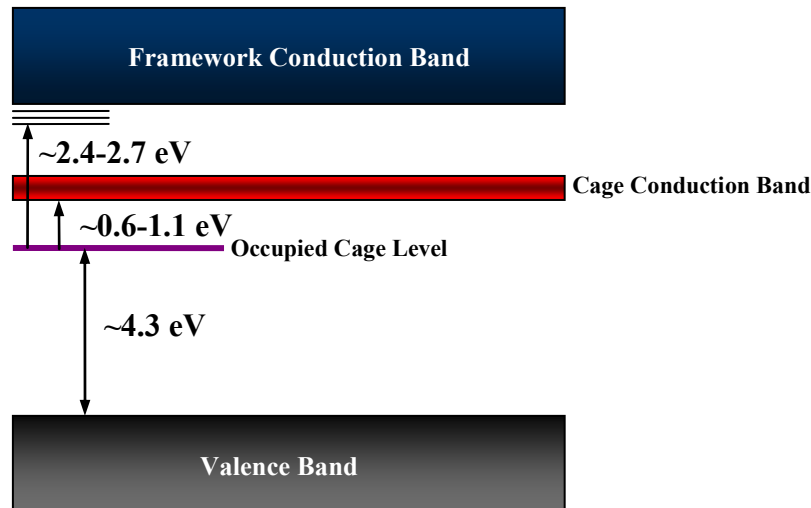


**Figure 2.6 Schematic illustration of cage and framework conduction bands energy levels and the position of electrons state in C12A7 electride [9]**

The electronic transitions in the material include the transitions from entrapped ions to the framework conduction band, from entrapped ions to the cage conduction band, from valence band to entrapped ions, and intra-ionic transitions [15]. The optical transition in infrared region (0.6-1.1 eV) is due to intercage transition of the electrons. The states of the excited electrons, which are occupied as a result of intracage transitions, are very close to the bottom of the framework conduction band. This may allow the electrons to migrate to the conduction band, hence exhibiting photoconductivity [23].

### **2.3.3 Electrical conductivity**

The temperature dependency of conductivity changes according to the level of conductivity in the material. The conductivity of semiconducting and conducting C12A7 as a function of temperature is shown in figure 2.7. When the conductivity is lower than  $10^{-3} \text{ S.cm}^{-1}$ , it follows the Arrhenius-type thermal activation behaviour [46]. In this case, the conductivity increases with the

increase in temperature and the logarithm of conductivity is proportional to  $T^{-1}$  which represents a simple polaron conduction model [7, 42, 44, 47]. This type of behaviour shows that carrier transport occurs via hopping of the electrons between the cages [47]. As the conductivity increases, however, the temperature dependency of the conductivity decreases and the logarithm of conductivity deviates from Arrhenius behaviour showing linearity with  $T^{-1/4}$  [7, 46, 47]. This means that the conductivity is controlled by a mechanism similar to variable-range hopping; i.e. when the concentration of the  $F^+$ -like centres is high and they are randomly distributed, they migrate with varied hopping distances [7, 16, 40, 42]. C12A7 with moderate conductivity is an n-type semiconductor [40] showing negative Seebeck coefficient ( $\sim -100\mu\text{V.K}^{-1}$  for a sample with a conductivity of  $10 \text{ S.cm}^{-1}$  at  $300 \text{ K}$  [48]). At higher conductivity values ( $\sim 100 \text{ S.cm}^{-1}$ ), the conductivity does not show a noticeable change against temperature [7, 46].

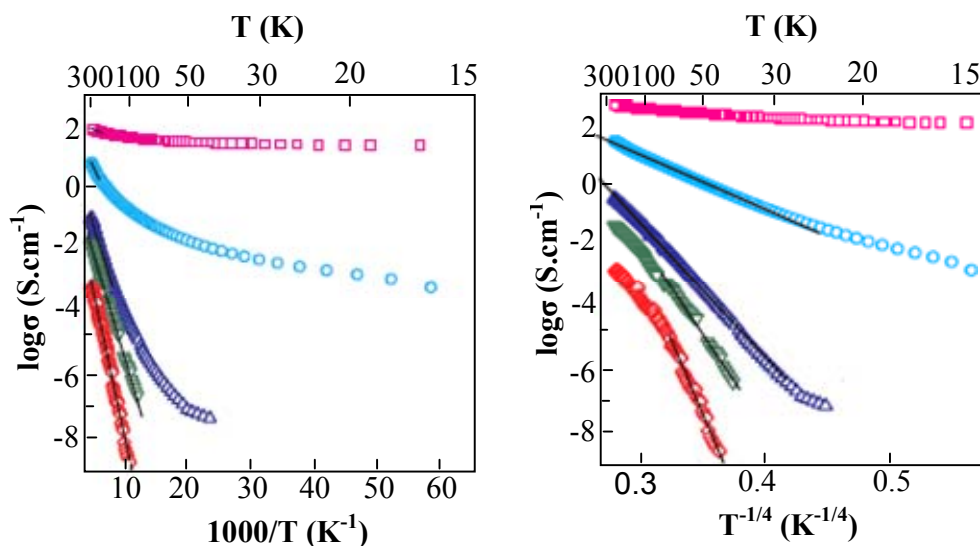
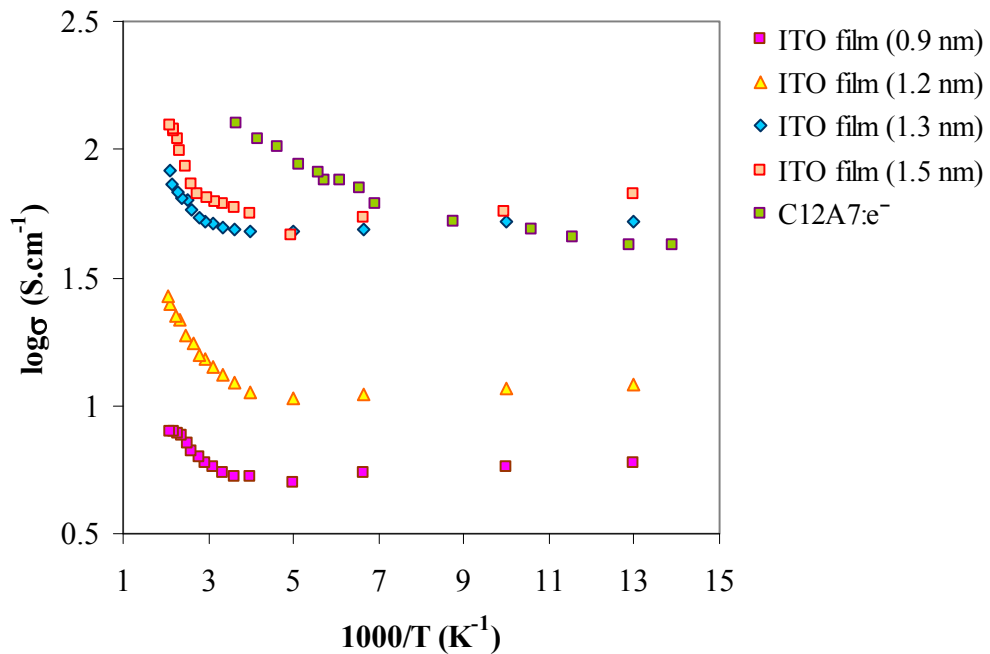


Figure 2.7 Temperature dependency of conductivity for semiconducting and conductive C12A7 [7]

In a highly conductive C12A7 (e.g.  $800 \text{ S.cm}^{-1}$ ), the conductivity is inversely proportional to the temperature. As the temperature increases, the mobility decreases, whereas the carrier concentration remains the same and the conductivity reduces as a result. This type of behaviour is observed in metallic conductors. Furthermore, highly conductive C12A7 exhibits superconductivity at low temperatures, typically between 0.2 to 0.4 K. The transition temperature depends on the carrier concentration. The increase in the number of electrons increases the transition temperature [47, 49]. The Seebeck coefficient also changes to positive values for highly conductive material ( $+8 \mu\text{V.K}^{-1}$  for a sample with a conductivity of  $\sim 600 \text{ S.cm}^{-1}$ ) [48].

The temperature dependency of conductivity for an electron incorporated C12A7 (electron concentration of  $9.7 \times 10^{20} \text{ cm}^{-3}$ ) in comparison with ITO thin film is plotted in figure 2.8.



**Figure 2.8** Temperature dependency of conductive C12A7 [50] in comparison with ITO thin films in a temperature range of 70-500 K. ITO films were prepared in four different thicknesses using electron beam evaporation and subsequent heat treatment at 800 °C for 3 hr [51].

As can be observed from the above figure, the conductivity of C12A7 is comparable to the one of ITO film. However, the level of conductivity can vary with preparation method and microstructure. The conductivity of highest quality thin films of ITO (prepared via physical vapour deposition at a substrate temperature of 300-400 °C) has been reported to be in the range of  $5-10 \times 10^3 \text{ S.cm}^{-1}$  [50]. This value is higher than the maximum reported conductivity for electron incorporated C12A7, i.e.  $1500 \text{ S.cm}^{-1}$  [17, 45]. ITO is still considered as the most successful and commonly used transparent conductive oxide. However, indium is likely to become a commodity in short supply. Although the electrical conductivity of highly electron-incorporated C12A7 is lower than ITO as a transparent conductive oxide, C12A7 exhibits unique physical properties such as low work function (minimum value of 2.4 eV compared to  $\sim 4.7 \text{ eV}$  for a typical ITO film) and superconductivity [50].

## **2.4 Optical properties of C12A7**

### **2.4.1 Optical absorption**

The interpretation of the optical absorption behaviour of C12A7 is one of the most beneficial methods in order to have a better understanding of the electronic structure of the material and evaluating the energy band diagram. The optical absorption curve of C12A7 consists of three main regions:

(1) A high absorption region in which the value of absorption coefficient is more than  $10^4 \text{ cm}^{-1}$  and the photon energy absorbed by the material is higher than the energy band gap [52, 53]. In this region, the absorption coefficient as a



function of photon energy for a simple parabolic band can be expressed by Tauc's formula [22]:

$$\alpha = \frac{B}{h\nu} (h\nu - E_g)^r \quad (2.1)$$

where  $h\nu$  is the photon energy,  $E_g$  is the optical band gap and  $r$  is an exponent which can take values of 1, 2, 3, 1/2 or 3/2. The value of  $r$  shows the nature of the electronic transition responsible for the optical absorption of the material. The energy band gap of C12A7 as well as the best value for  $r$  can be determined from the linear  $(\alpha h\nu)^{1/r} - h\nu$  plot.  $B$  is a constant which is given by the following formula [53]:

$$B = \frac{4\pi\sigma_0}{nc\Delta E} \quad (2.2)$$

where  $c$  is the speed of light,  $\sigma_0$  is the extrapolated dc conductivity at  $T = \infty$ ,  $\Delta E$  is a measure of the extent of band tailing and  $n$  is the refractive index.

(2) An intermediate absorption region with an absorption edge between 1 to  $10^4 \text{ cm}^{-1}$ . In this region, the energy of the photons absorbed by the material is lower than the band gap energy and the absorption coefficient follows an exponential relationship with both the photon energy and the temperature according to Urbach's formula [54]:

$$\alpha(h\nu, T) = \alpha_0 \exp\left[\frac{\sigma(h\nu - E_0)}{kT}\right] \quad (2.3)$$

where  $\alpha_0$  and  $E_0$  are the characteristic parameters of the material,  $\sigma$  is the steepness parameter,  $k$  is the Boltzmann constant and  $T$  is the temperature. This

equation implies that below the energy band gap, the absorption is due to Urbach tail [15]. Urbach tail, also known as Urbach energy, is defined as the width of the band tails of the localised states which extend into the band gap [53]. The parameter  $\frac{kT}{\sigma}$  corresponds to the width of this exponential absorption tail [15]. The logarithm of absorption coefficient as a function of photon energy within the Urbach region, gives a straight line. The extrapolations of the lines for different temperatures usually converge at one single point, also known as *the converging point*, which gives the values of  $E_0$  and  $\alpha_0$  for x and y coordinates respectively [55]. The steepness parameter,  $\sigma$ , which is determined from the slope of the straight line near the absorption edge, is expressed by the following equation [56]:

$$\sigma = \sigma_0 \cdot \left( \frac{2kT}{\hbar\omega_p} \right) \cdot \tanh \left( \frac{\hbar\omega_p}{2kT} \right) \quad (2.4)$$

where  $\sigma_0$  is a temperature independent (but material dependent) parameter characterizing the corresponding optical excitation and  $\hbar\omega_p$  is the energy of the phonons associated with Urbach tail [55, 56].

The structural disorder of C12A7 is attributed to the random distribution of extra-framework anions which alters the crystallographic location of the ions at the cage wall ( $\text{Ca}^{2+}$  ions in particular) and results in the distortion of the filled cages. A temperature increase leads to a further fluctuation of these ions. The structural disorder is more severe in the case of incorporation with doubly charged species such as  $\text{O}^{2-}$  ions. In addition to the charge, the off-centre position of  $\text{O}^{2-}$  ion inside the cage displaces the cage-wall  $\text{Al}^{3+}$  ions and increases the structural disorder.

In order to reflect the contribution of structural disorder as well as thermal disorder in C12A7, the following equation has been introduced for the Urbach energy [15]:

$$E_U = \frac{kT}{\sigma} = \frac{\hbar\omega_p}{2\sigma_0} \left[ \coth\left(\frac{\hbar\omega_p}{2kT}\right) + X \right] \quad (2.5)$$

where  $X$  is a dimensionless measure of the structural disorder normalized to the zero-point vibration energy of  $\frac{\hbar\omega_p}{2}$ . The Urbach tail in C12A7 is mainly due to structural disorder at low temperatures; however, at temperatures higher than  $\sim 100$  °C, the effect of thermal fluctuations becomes more dominant. The value of  $X$ , however, is not as significant as the structural disorder caused by anion vacancy formation in a typical crystal [15].

(3) A weak absorption region with an absorption coefficient of less than  $1 \text{ cm}^{-1}$ . The shape and magnitude of absorption in this region depend on the purity, thermal history and preparation conditions of the material [53].

The fundamental optical absorption edge of C12A7 framework is close to 6.8 eV with electronic transitions of  $\sim 6$  eV from the valence band to the tail of the conduction band. The presence of extra-framework species, however, shifts the absorption edge of the material towards lower energies. The absorption edge shift depends strongly on the type of the incorporated species.

The smallest shift of the fundamental absorption edge corresponds to the incorporation of  $F^-$  ion species inside C12A7 framework [15]. The value of  $\sim 6.1$  eV has been reported for the absorption edge of C12A7:F<sup>-</sup> [57]. In addition, the occupied  $F^-$  states are located well below the top of the valence

band. Therefore, the optical absorption edge is mainly due to electronic excitation from the valence band to the framework conduction band and the  $F^-$  ions do not contribute in the transition directly. Therefore, the absorption edge of  $C_{12}A_7:F^-$  can also be considered as the fundamental absorption edge of  $C_{12}A_7$  framework (i.e. without any extra-framework ions incorporated) [15].

The absorption edge shifts to a lower value of  $\sim 5.7$  eV upon  $OH^-$  ion incorporation [57]. The presence of a high concentration of  $OH^-$  ions in  $C_{12}A_7$  can also lead to the appearance of an additional optical absorption band at 0.44 eV [18, 47].

The absorption edge shift to a lower energy of  $\sim 4.6$  eV is the result of anion-to-framework conduction band transition in  $O^{2-}$ -incorporated  $C_{12}A_7$ . The transition to the cage conduction band has a low density and therefore does not affect the absorption edge energy considerably.

The superoxide-incorporated  $C_{12}A_7$  has a low absorption edge energy close to 3.7 eV. Upon heating the material above 200 °C, the absorption edge shifts to even lower energy levels and enters the visible region which results in the appearance of an absorption peak at  $\sim 3$  eV and the sample colour changes to yellow. The presence of active oxygen radicals, such as  $O^\cdot$ ,  $O_2^\cdot$  and  $O_2^{2\cdot-}$ , also leads to the formation of two additional absorption bands at  $\sim 4.3$  and 4.7 eV. The appearance of these bands is attributed to the transitions from the valence band to the occupied state of the radicals and the intra-molecular transitions of these species [15].

Figure 2.9 shows a comparison between the optical absorption spectra of the stoichiometric and electron-incorporated  $C_{12}A_7$ .

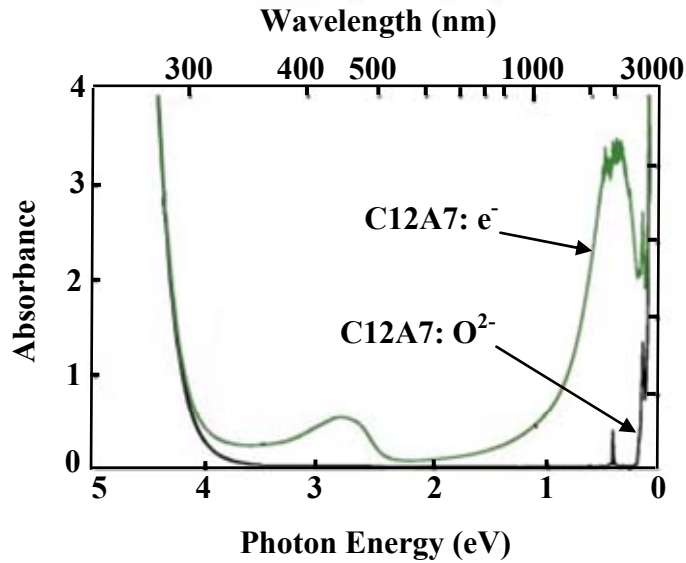


**Figure 2.9 Comparison between the optical absorption spectra of the  $O^{2-}$  and electron-incorporated C12A7 [24]**

Two additional absorption bands are observed for the electron-incorporated material. The appearance of these additional absorption bands is attributed to the formation of  $F^+$ -like centres. These centres are formed when electrons replace extra-framework  $O^{2-}$  ions and produce partially positive centres in the structure. The intercage and intracage transitions of the electrons produce the optical absorption bands. Furthermore, the migration of these electrons is responsible for the electrical conductivity of the material [9].

The position of the trapped electrons is 4.3–4.7 eV above the top of the valence band. There is a small barrier for the hopping of the electrons between the cages, i.e. the distance between the occupied states of the electrons and the cage conduction band. The optical absorption band at 0.4 eV is attributed to this intercage s-to-s transition.

The optical absorption band at 2.8 eV corresponds to the barrier for the electrons to migrate to the framework conduction band and is interpreted as the

intracage s-to-p transition [1, 9]. This absorption band is responsible for the green colour of the conductive C12A7 [7]. The intensity of the absorption band at 2.8 eV (intra-cage transitions and absorption of light in the visible region) is adversely related to optical transmittance and determines the optical transparency of the material [42]. The intensities of both bands change with the level of conductivity treatment [7]. A highly conductive C12A7 does not show a distinctive optical absorption band at 0.5 eV and exhibits a Drude-type absorption profile instead, due to the absorption of free carriers [47].

The value of optical absorption edge, and hence the energy band gap of the material, also depends on the temperature. The optical absorption shift as a function of temperature is shown in figure 2.10 for a hydroxide-loaded C12A7 sample.

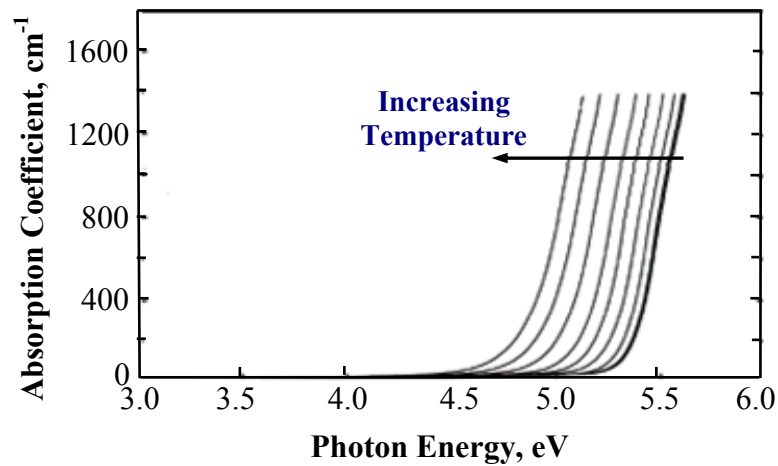


**Figure 2.10** Dependence of optical absorption edge on temperature for C12A7 annealed in moist atmosphere. The absorption edge shifts towards lower energies with an increase in the temperature [15]

The temperature dependency of the band gap energy can be expressed by the following equation [52]:

$$E_g(T) = E_g(0) - \frac{\alpha T^2}{T + T_0} \quad (2.6)$$

where  $E_g(T)$  is the band gap energy at temperature  $T$ ,  $E_g(0)$  is the band gap energy at 0 K and  $\alpha$  and  $T_0$  are material-dependent parameters.

### 2.4.2 Reflectivity

A comparison between the reflectivity spectrum of a C12A7 sample with the ones of CaO and Al<sub>2</sub>O<sub>3</sub> is given in figure 2.11. In contrast to simple oxides like CaO and Al<sub>2</sub>O<sub>3</sub>, no sharp reflectivity peak is observed in C12A7, probably due to the large unit cell and lattice disorder which results in an inhomogeneous broadening of the peaks; although there is a significant increase in the reflectivity above ~ 5 eV [43].

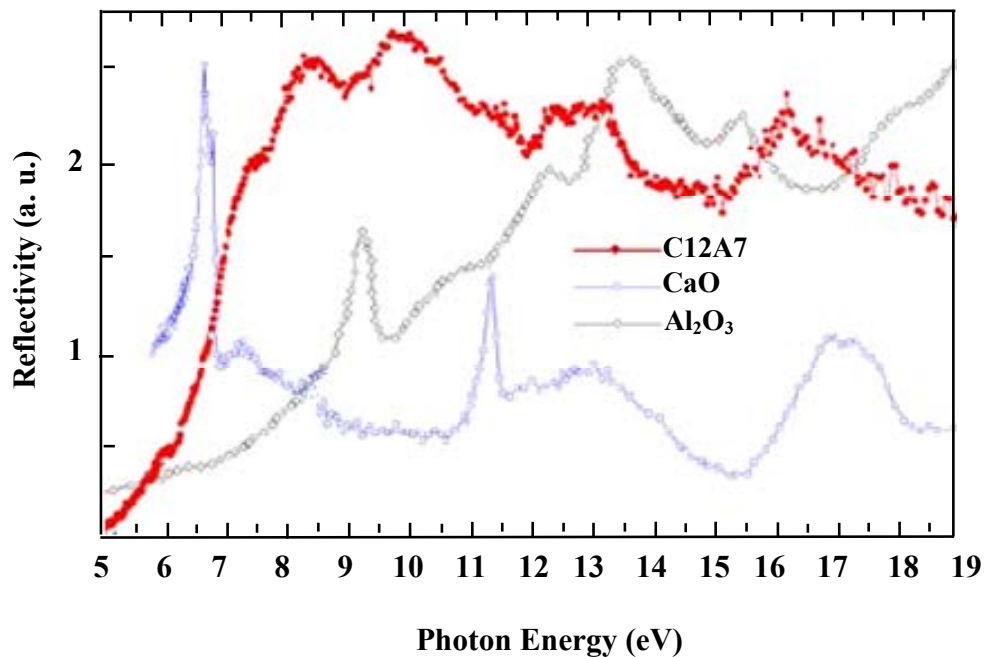


Figure 2.11 Reflectivity spectrum of a C12A7 single crystal [43] compared to the reflectivity of the constituents Al<sub>2</sub>O<sub>3</sub> [58] and CaO [59]

### 2.4.3 Luminescence

The nature of the species trapped inside the cages can change the luminescence behaviour of C12A7. The photoluminescence band at 4.5 eV is only dominated in  $O^{2-}$ -incorporated C12A7, which has been heat treated in a moisture-free atmosphere. The material containing  $OH^-$  species shows complex bands between 3.3 to 4.1 eV [60], while most of the other entrapped species, such as  $O_2^-$ , show no luminescence due to strong electron-phonon interactions with the cage and non-radiative relaxation [27]. A comparison between the luminescence spectra of  $O^{2-}$  and  $OH^-$ -incorporated C12A7 is depicted in figure 2.12.

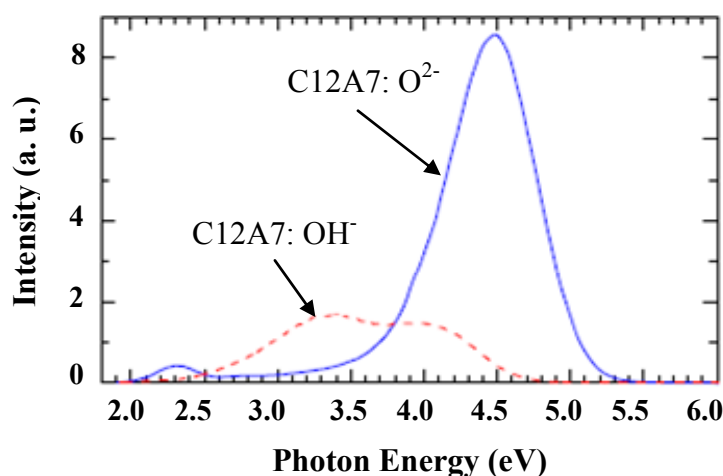


Figure 2.12 Comparison between the luminescence spectra of  $O^{2-}$  and  $OH^-$ -incorporated C12A7 at 10 K excited by 6.9 eV photons [60]

$Au^-$  ion has been reported to be the only known incorporated species in C12A7 that exhibits photoluminescence. This is due to a lower electron-phonon interaction between this anion and the framework, and therefore, less non-radiative relaxation of this anion compared to other negative ionic species. The



reason for this behaviour can be attributed to the fact that  $\text{Au}^-$  ion has a close diameter to that of the cage.

The energy of the luminescence peak is equivalent to the energy difference between the excited and ground states [27]. The luminescence band for  $\text{C12A7}:\text{O}^{2-}$  is located at  $\sim 3.3$  eV, while the luminescence band at 4.9 eV appears only for the electron-loaded material. The latter energy is equal to the distance between the occupied states of the entrapped electrons and the top of the valence band. Therefore, this band can be related to the recombination of entrapped electrons with the valence band holes. Another sharp increase in the emission intensity is observed at 6.8 eV, which represents the framework band gap. The framework conduction band is dependent upon random distribution of the entrapped species and is estimated to be higher than 6.8 eV [43].

#### **2.4.4 Photochromism**

A glass phase formed as a result of quenching C12A7 melt in a reducing atmosphere (e.g. in a carbon crucible) exhibits photochromism. The as-formed glass is transparent; however, upon exposure to ultraviolet radiation, it turns grey and once the radiation is terminated, it changes back to transparent. Therefore, the product of quench under a reducing atmosphere is called a *reduced glass*. The heat treatment of the reduced glass under vacuum in a  $\text{SiO}_2$  crucible produces an electrically conductive C12A7 which is green in colour [1]. The mechanism of this transformation is explained in section 2.8.3.

## 2.5 C12A7 fabrication techniques

- **Single crystal**

C12A7 single crystals are fabricated via two techniques: floating zone and Czochralski methods.

In the floating zone method, C12A7 powder is first prepared via a conventional process, such as solid-state reaction, with  $\text{CaCO}_3$  and  $\text{Al}_2\text{O}_3$  as the starting materials. The powder is pressed under a hydrostatic pressure and sintered in a temperature range of 1250–1300 °C in an oxygen atmosphere for at least 12 hr. The sintered polycrystalline compound is then used as the seed for the growth of the single crystal [61]. The melting process is done by the electronic bombardment of the seed in an infrared heating furnace [62]. Although the solubility of oxygen gas in C12A7 melt is quite high, it reduces significantly upon rapid cooling. As a result, the dissolved  $\text{O}^{2-}$  ions precipitate as oxygen molecules during the solidification of the melt and remain in the final product in the form of micropores [62, 63].

In the Czochralski method, pure  $\text{CaCO}_3$  and  $\text{Al}_2\text{O}_3$  are mixed and melted in an induction furnace using an iridium crucible. The crystal is then grown by pulling up a rotating seed (a C12A7 single crystal) from the melt at a constant rate. Since iridium is highly reactive at such high temperatures in an oxidative atmosphere, the amount of oxygen in the atmosphere should be kept at a minimum level in order to prevent the oxidation of the crucible [63]. The disadvantages of this method include technical issues due to prolonged annealing at temperatures above 1400 °C and the interaction between the melt and the crucible [37].

- **Polycrystalline bulk**

Solid-state reaction is the most common technique used for the preparation of polycrystalline C12A7 bulk. High-purity powders of  $\text{CaCO}_3$  and  $\text{Al}_2\text{O}_3$  or  $\text{Al}(\text{OH})_3$  are usually chosen as the starting materials and mixed at a molar ratio of 12:7. The heat treatment is done at  $1350\text{ }^\circ\text{C}$  for a minimum duration of 8 hr in an air or oxygen atmosphere [64]. The formation of C12A7 requires a long heat treatment time due to the poor homogeneity of the mixed powders [65].

Self-propagating combustion technique is an alternative method for bulk fabrication. Calcium and aluminium nitrate are dissolved in distilled water. Urea ( $\text{CH}_4\text{NO}_2$ ) is then added to the solution and heated at a temperature of  $\sim 500\text{ }^\circ\text{C}$ . The dehydration and decomposition processes are normally complete within a few minutes. The product of the combustion, which is the precursor of C12A7, is then heat treated at  $1100\text{ }^\circ\text{C}$  for 48-72 hr in order to obtain a crystallized C12A7 compound [66]. An alternative solution contains aluminium nitrate, calcium carbonate and nitric acid as the starting ingredients. Ethylene glycol is then added to the mixture and gradually heated up to a temperature high enough to start the self-propagating reaction. The product is ground into powder and calcined at  $700\text{ }^\circ\text{C}$  for 1 hr. The calcination product is pressed into pellets and sintered at  $1000\text{ }^\circ\text{C}$  for 72 hr in air. A single-phase bulk is obtained via this technique with a density of typically 95 % of the theoretical density [37]. Although the heat treatment temperature is reduced compared to solid-state reaction method, the annealing time is still high [66].

- **Thin film**

C12A7 thin film can be fabricated via pulsed laser deposition technique. An amorphous layer of C12A7 is deposited on a magnesium oxide single crystal substrate. The deposition is done at room temperature under an oxygen partial pressure of  $\sim 1 \times 10^{-3}$  Pa followed by a crystallization heat treatment at 1100 °C in air atmosphere [4, 67]. A crystalline C12A7 bulk is also needed as the target for the deposition. The thin film preparation can alternatively be done via sol-gel technique. This method is explained in detail in the following section.

## **2.6 Fabrication of C12A7 via sol-gel technique**

Sol-gel technique is a chemical method of fabricating amorphous C12A7 thin films. A crystalline structure is obtained via a subsequent heat treatment in air atmosphere [68]. A schematic outline of this process is shown in figure 2.13.

The advantages of sol-gel method include excellent homogeneity of the films, controlled composition, low heat treatment temperature and high purity of the final product [3, 68, 69].

In addition, some applications utilizing calcium aluminate glasses require low-temperature production techniques due to a high tendency of these glasses to crystallize upon heating. Hence, the synthesis of the glass can be done using sol-gel method [70].

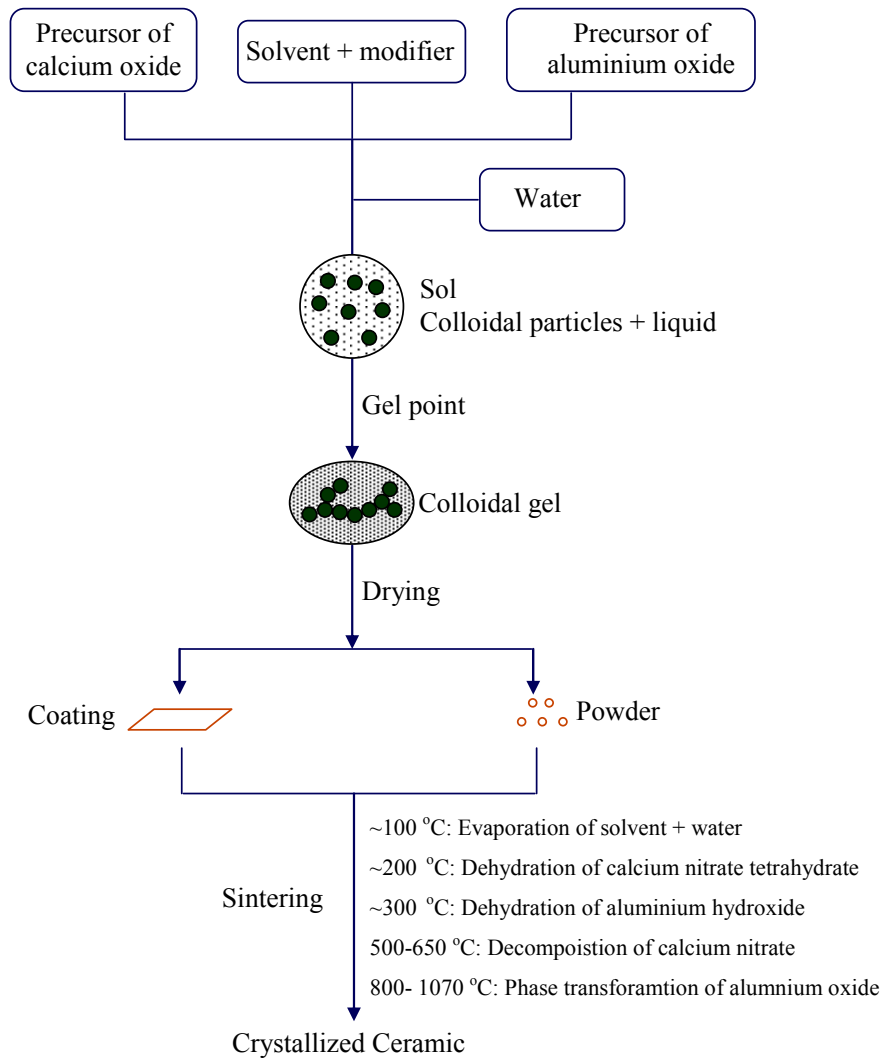


**Figure 2.13 Schematic outline of sol-gel process**

Two limiting factors of this process are relatively low critical thickness (usually less than 100 nm for oxide films other than silica) and rather short life time of the solution [5, 71]. Critical thickness is defined as the maximum thickness of a crack-free thin film produced via one-step coating [72, 73].

### **2.6.1 Ingredients for solution preparation**

- **Aluminium and calcium precursors**

Calcium nitrate tetrahydrate and aluminium sec-butoxide (ASB) can be used as the precursors of calcium oxide and aluminium oxide respectively [68].

Aluminium sec-butoxide is one of the most common aluminium alkoxides used as a precursor of aluminium oxide with the ability to remain in liquid state at room temperature and fabricate relatively pure and homogeneous materials at low temperatures. The main disadvantage of this compound is the high affinity for water absorption and fast hydrolysis which leads to precipitation and is attributed to its electronegative alkoxy groups [68, 74]. Therefore, an organic solution is usually used with a limited amount of added water in presence of a chelating agent, such as ethyl acetoacetate. Organic solutions, on the other hand, often produce highly porous films and hence, utilizing an aqueous solution can be advantageous in terms of obtaining compact structures. Therefore, chemical modification is needed in order to control the hydrolysis and condensation processes and ensure the formation of compact structures [74]. This process is explained in detail in section 2.6.2.

- **Solvent and water**

Organic solvents, such as Isopropyl alcohol, are good mutual solvents for aluminium alkoxide-ethyl acetoacetate mixture and calcium nitrate. Increasing the alcohol content of a solution can prolong the gel formation, although it does not have any effect on the homogeneity of the solution [68].

The addition of water can also prolong gel formation, but it also has a negative effect on the homogeneity of the solution [68]. An increase in water-to-alkoxide ratio results in an increase in the condensation rate and particle size [75].

The hydrolysis of aluminium alkoxide can be observed from the formation of alumina precipitates during solution making [69]. In order to prevent rapid

hydrolysis of the alkoxide and maintain a solution with a reasonable life time, the ratio of water to alkoxide should be kept either very low or very high (around 100:1) [69]. The slowest possible hydrolysis rate can be obtained without the addition of water. In this case, the solution is exposed to a moist atmosphere for the hydrolysis to take place gradually. The gelation process can take up to one day to complete and a highly homogenous gel is obtained [68]. The alumina content in a solution with a high amount of water is not enough for preparing thick films and any thick films produced normally contain cracks. Therefore, the presence of a modifier in the solution is necessary [69].

- **Substrate**

Several materials have been examined as the substrate for C12A7 thin film including MgO, YSZ, sapphire and SiO<sub>2</sub>. MgO single crystal is found to be the only material among others that forms single phase C12A7, while other substrates react with CaO component during the heat treatment [76].

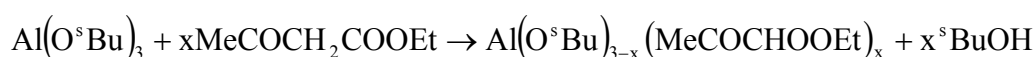
### **2.6.2 Chelation**

As mentioned earlier in this section, electronegativity of the alkoxy groups in aluminium sec-butoxide is the main reason for fast and irreversible reaction of the alkoxide with water, which results in the precipitation of alumina and sec-butanol [77]. The hydrolytic instability of ionic bonds can be modified by addition of carboxylic acids,  $\beta$ -ketoesters or  $\beta$ -diketones to the alkoxide. Organic ligands with unsaturated bonds are more reactive and can produce additional organic networks with the alkoxide [75]. The presence of a chelating

agent can reduce the hydrolysis rate and alkoxide-to-hydroxide transformation can be controlled during sol-gel process [68].

Ethyl acetoacetate (EAA) is a  $\beta$ -ketoester with saturated ligands [75] which predominantly consists of ketons in pure form and its enol content is rather low, but when added to aluminium alkoxide, the enol form reacts with the alkoxy groups bonded to Al and produces chelates, resulting in the formation of more enols. In other words, the chelation process stabilizes the enol form of the ester [68, 77].

The chelation of aluminium sec-butoxide with enol, shown in figure 2.14, occurs via the following exothermic reaction [68]:



The chelating ligands have less affinity for water compared to alkoxy groups and hence, the bonding of these ligands to Al reduces the extent of the hydrolysis and condensation reactions of aluminium alkoxide [68].

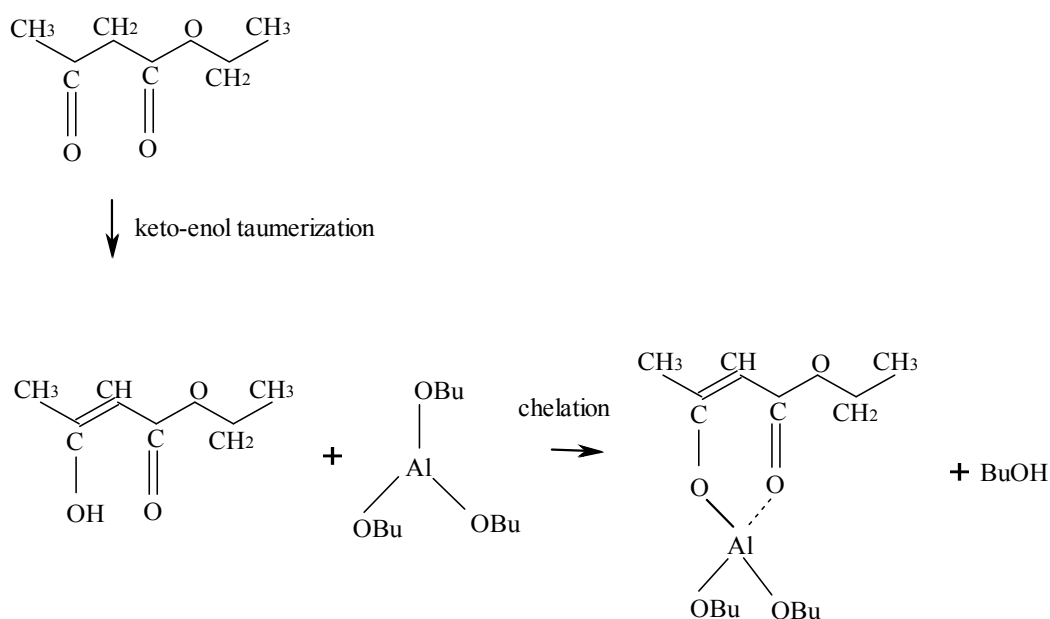


**Figure 2.14 Chelation of aluminium sec-butoxide with ethyl acetoacetate [68, 75]**



For an EAA-to-alkoxide ratio of 3:1, the chelation is nearly complete and the hydrolysis rate becomes extremely low. The practical ratio is normally kept at 2:1 in order to control the rate of hydrolysis as well as the microstructure [77].

Some of the EAA ligands might be released upon hydrolysis and even evaporate from the solid gel. The chelated portion of the mixture exhibits an organic nature [68]. The extent of gelation depends on the amount of chelates that break down during hydrolysis. The nature of the hydrolysis agent added to the solution can have an effect on the rate of chelate removal and therefore, the properties of the final product [77].

If EAA is added after the addition of the hydrolysis agent, the chelation of alumina precipitates is more likely to occur rather than the chelation of aluminium sec-butoxide [69].

### 2.6.3 Hydrolysis

In order for the hydrolysis to take place completely, each mole of aluminium sec-butoxide requires at least 3 moles of water; otherwise, even if the gelation occurs, the hydrolysis will not be complete [77].

The product of aluminium sec-butoxide hydrolysis is  $\gamma$ -aluminium oxyhydroxide  $\text{Al}(\text{OH})_3$ , or gibbsite, which goes through dehydration and phase transformation during the heat treatment resulting in the formation of stable  $\text{Al}_2\text{O}_3$  [78]. The hydrolysis of aluminium sec-butoxide in the absence of a chelating agent occurs through the following chemical reaction [79]:



The by-product of the hydrolysis is butyl alcohol accompanied by an increase in the pH of neutral and alkaline solutions and a decrease of pH in acidic systems [77].

The ratio of water to aluminium alkoxide also affects the product of the hydrolysis. If this ratio is increased to about 25:1, bayerite ( $\alpha - \text{Al}(\text{OH})_3$ ) is more likely to be formed instead of gibbsite. In other words, gibbsite has higher stability in low water content. The presence of impurities, such as high salt concentration of the solution, can also stabilize gibbsite. The hydrolysis of chelated aluminium sec-butoxide is shown schematically in figure 2.15.

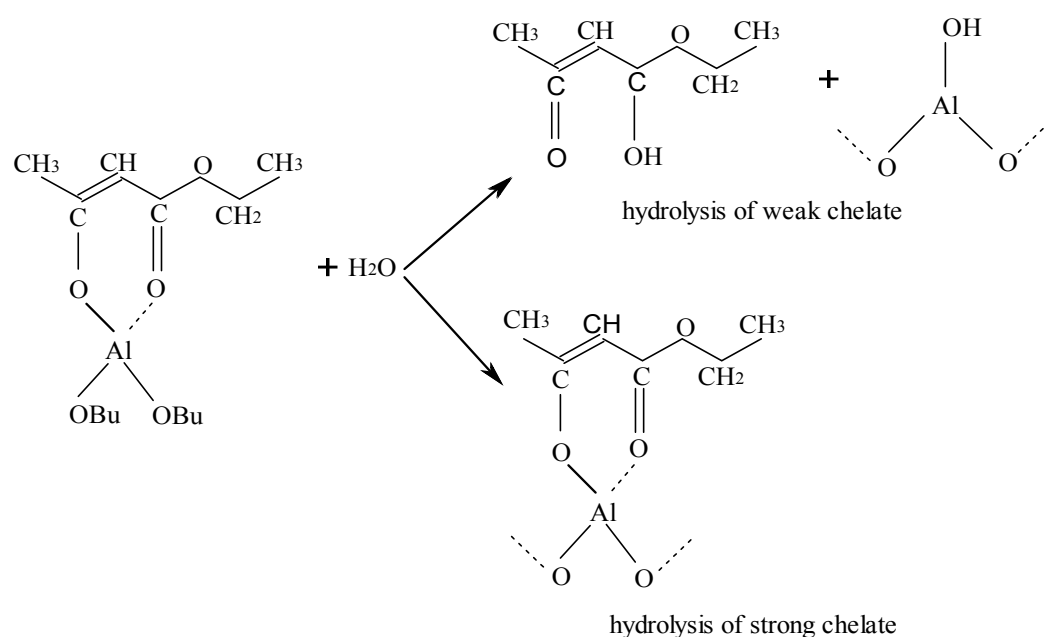
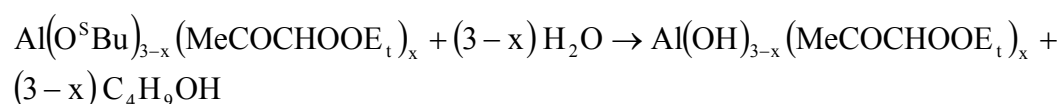


**Figure 2.15 Hydrolysis reaction of aluminium sec-butoxide chelated with ethyl acetoacetate [75]**

In the presence of a chelating agent, the extent of hydrolysis depends on the amount and type of chelates. Since the non-chelated alkoxy groups have higher affinity for water, the hydrolysis starts with free alkoxy groups and only a

fraction of mono/di substituted chelates are released during the process. The tri-substituted chelates are completely resistant against hydrolysis.

Upon the hydrolysis of EAA-modified aluminium sec-butoxide,  $[\text{Al}(\text{OH})_{3-x}(\text{EAA})_x]_n$  oligomers are formed as well as  $\text{Al}(\text{EAA})_3$  which is not hydrolyzed [68]:



It has been reported that adding an excess amount of water as the hydrolysis agent or increasing the temperature of the solution to  $\sim 260^\circ\text{C}$  (the decomposition temperature of EAA) can assist the hydrolysis and gelation processes. Since the latter process is impractical for aqueous solutions, the choice of a proper chelating agent with good hydrolysis/gelling capability is very important [77].

#### **2.6.4 Addition of acid**

Due to the high sensitivity of aluminium sec-butoxide to water, the hydrolysis process results in the rapid formation of alumina colloids which change the colour of the solution from transparent to white, making the solution unstable with a rather short lifetime [70]. Therefore, the addition of an acid, such as nitric or hydrochloric acid, is still necessary to peptize the colloids and obtain a clear solution [3, 70, 73, 80]. Even though the presence of a chelating agent, such as EAA, reduces the rate of hydrolysis, the addition of hydrochloric or nitric acid is still reported in the literature to produce a transparent solution, which shows that adding a chelating agent is not enough in order to obtain a clear solution

[70]. However, during the process of optimizing the solution preparation technique, which is one of the main objectives of this research, a new recipe was obtained with a significant improvement in the stability of the solution (up to a few months) without the need for the addition of acid. The details of the solution ingredients and preparation technique will be explained in detail in section 3.1.

### **2.6.5 Thin film application**

Solution-processed thin films can be prepared by drop casting, dip coating or spin coating techniques. The formation of a thin film through spin coating consists of four stages: deposition which is the dispersion of the solution on the surface of the substrate, spin-up in which the solution flows toward the edges of the substrate, spin-off where the excess amount of solution is spread as droplets and leaves the surface of the substrate, and the last stage which is the evaporation of the solvent [81].

### **2.6.6 Heat treatment**

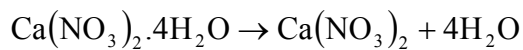
The heat treatment of the dried gels enables the remaining organic solvents and water to be removed completely, followed by condensation and crystallization of C12A7 through a chemical reaction between CaO and Al<sub>2</sub>O<sub>3</sub>. However, if the desired final product is to be amorphous, then the heat treatment should be avoided due to the high affinity of calcium aluminate glasses for devitrification. [70].

The crystallization of a calcium aluminate single phase via heat treatment of the gel is difficult due to a number of reasons, including the variation of the

precursors compositions as a result of sol segregation, high number of possible phases in CaO-Al<sub>2</sub>O<sub>3</sub> binary system that might be formed during the heat treatment, and limited long-term diffusion of ions at moderate temperatures [68].

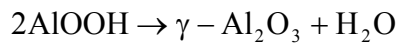
A heat treatment at ~1100 °C for about 3 to 6 hr under an air/dry oxygen atmosphere has been suggested in the literature for the crystallization treatment of the dried films [49, 67].

Upon heating up, the remaining water and organic solvents in the dried gel start to evaporate. This process starts at around 100 °C [68]. The next stage is the dehydration of calcium nitrate tetrahydrate, which occurs between 100 and 200 °C [82]:

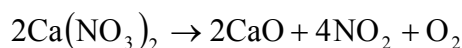


The decomposition of residual alkoxy groups also occurs at around the same temperature range [83].

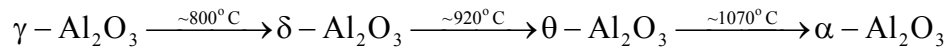
The dehydration of gibbsite starts at around 300 °C leading to the formation of boehmite (AlOOH). Further dehydration of boehmite at ~400 °C occurs according to the following reaction [78]:



The decomposition of calcium nitrate occurs between 500 and 650 °C forming calcium oxide. The crystallization of calcium oxide is complete at approximately 820 °C. The decomposition happens through the following reaction [68]:



$\gamma$  – alumina also goes through phase transformation and crystallization including the formation of metastable alumina phases, which take place as follows [84]:



The final stage of the heat treatment is the chemical reaction of CaO and  $\alpha - \text{Al}_2\text{O}_3$  at a temperature of approximately 1050 °C which results in the formation of  $12\text{CaO} \cdot 7\text{Al}_2\text{O}_3$  compound.

The decomposition of EAA takes place at temperatures between 100 to 250 °C [83]. When chelated to  $\text{Al}_2\text{O}_3$ , however, the decomposition occurs in a wide temperature range between 200 and 700 °C leading to a long-lasting structural relaxation and gradual densification process, hence preventing the formation of cracks and increasing the critical thickness [69].

## **2.7 Anion-incorporated C12A7 fabrication techniques**

### **2.7.1 Incorporation with superoxides**

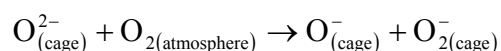
The trapped  $\text{O}^{2-}$  ions in C12A7 can be selectively replaced by other oxygen ion species [8]. By heating the material at 1350 °C and subsequent cooling in dry oxygen atmosphere, various superoxide ions, such as  $\text{O}^-$ ,  $\text{O}_2^-$  and  $\text{O}_3^-$ , can be introduced into the structure [19, 39].  $\text{O}^-$  ion is the most active oxygen ion among all oxygen species [40]. Superoxide-incorporated C12A7 can have potential applications as a strong oxidizing catalyst, oxygen ion conductor, field-induced oxygen ion emitter and in biochemical reactions [39, 40].

An  $O^-$  – loaded C12A7 can produce a high intensity monochromatic  $O^-$  ion beam under the effect of an extraction electric field [25]. The emission of  $O^-$  ions from C12A7:  $O^- + O_2^-$  is different from other ion-conducting materials such as yttria- stabilized zirconia (YSZ). A metal electrode is needed at the surface of YSZ to dissociate  $O^{2-}$  ions. An electric field is applied to YSZ which results in the migration of the  $O^{2-}$  ions from the bulk to the surface of the material. A metal electrode such as platinum is needed at the surface to help with the dissociation of these species into  $O^-$  ions and electrons. The  $O^-$  ions are then emitted thermionically from the surface of the oxide [41].

In  $O^- + O_2^-$  ion-incorporated C12A7, however, the concentration of the superoxides is high enough for the direct extraction of these ions from the surface, and the obtained current densities are considerably higher. Furthermore, there is no need for a metal electrode on the material surface [40].

The superoxide species can be incorporated inside the structure in large concentrations while retaining the chemical and thermal stability of the material, whereas they are very reactive in other metal oxides even at room temperature [15].

Active oxygen species,  $O^-$  and  $O_2^-$ , are formed in a dry oxygen atmosphere according to the following reaction [40]:



The superoxide-incorporated C12A7 has more stability compared to the stoichiometric structure and  $O^{2-}$  ions react easily with oxygen molecules to form superoxides inside the cages. Although the enthalpy of these reactions is negative, the amount is less than that of a gas-phase reaction, probably due to

the interaction of  $O^{2-}$  ions with the lattice, since these ions are not totally free in solid phase.

A schematic illustration of superoxide incorporation in C12A7 is shown in figure 2.16. The  $O^-$  and  $O_2^-$  formation mechanism consists of two stages: bulk diffusion and surface reaction. The  $O^{2-}$  ions diffuse from the bulk to the surface of the material and the reaction with atmospheric  $O_2$  takes place at the surface. Then the resultant  $O^-$  and  $O_2^-$  ions diffuse into the bulk and occupy the empty cages [39].

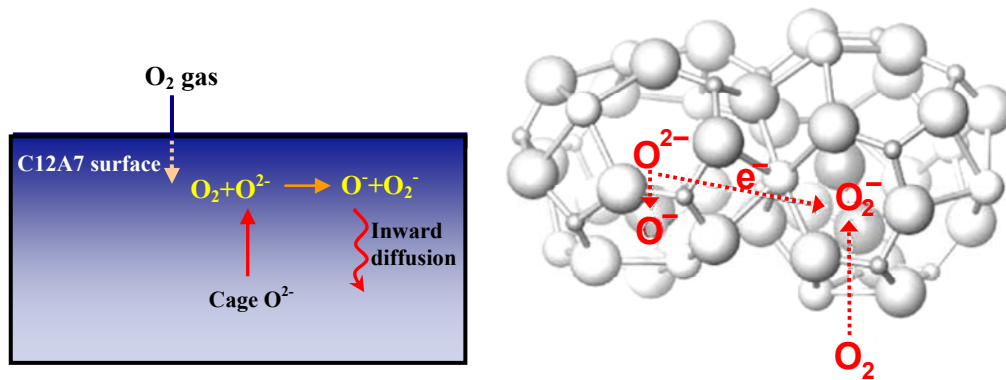


**Figure 2.16 Schematic illustration of superoxide formation. The extra-framework  $O^{2-}$  is oxidized by oxygen molecules at the surface of the material and the products enter the empty cages by inward diffusion in order to compensate for the lack of negative charge in the framework [85]**

The concentration of oxygen ion species at the surface of the material during the annealing process is in equilibrium with the atmosphere. The flux within the surface and the bulk, however, is controlled by diffusion mechanism [85]. Therefore, the latter process has more influence on the superoxide ion formation and is the only rate limiting stage [39, 85].

The concentration of active oxygen ions is dependent upon the degree of humidity, the oxygen pressure and the temperature during heat treatment and



subsequent cooling. The maximum concentration of oxygen radicals increases with the decrease in temperature, and although the concentration of  $O_2^-$  is always more than that of  $O^-$  (probably due to less stability of  $O^-$  compared to  $O_2^-$ ), the difference reduces as the total concentration reaches its maximum value [39].

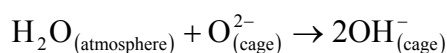
The presence of a large number of  $O^{2-}$  ions in the structure is crucial for the formation of active oxygen species. Since  $O^{2-}$  ions tend to react easily with  $H_2O$  and form  $OH^-$ , the heat treatment of C12A7 in a moist atmosphere leads to the entrapment of a large amount of  $OH^-$  ions and, as a result, the formation of active oxygen anions will be limited [20, 40, 86]. Therefore, the heat treatment of C12A7 during crystallization and superoxide incorporation processes should be done in a moisture-free atmosphere [39]. If the material initially contains  $OH^-$ , heat treatment at temperatures higher than 1100 °C in dry oxygen atmosphere leads to the desorption of this species and the concentration of active oxygen ions will increase as a result in the subsequent heat treatment [20].

### **2.7.2 Incorporation with hydroxide**

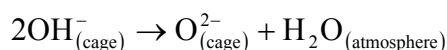
$OH^-$  ions replace extra-framework  $O^{2-}$  species via heat treatment in moist atmosphere and are the most stable incorporated ions in C12A7 [15].

The stability of  $OH^-$  species in C12A7, even after treatment at high temperatures, is a unique characteristic of this compound. No other material has been reported to have the ability to preserve high concentrations of  $OH^-$  at temperatures as high as 1300 °C [18].

C12A7 can absorb water during the annealing process via the following reaction [18]:



Therefore, the presence of water in the atmosphere results in OH<sup>-</sup> incorporation. If the material is sintered in dry oxygen atmosphere, the OH<sup>-</sup> ion is released and removed from the structure [18]:



The dehydroxylation of OH<sup>-</sup> ions in C12A7:OH<sup>-</sup> normally occurs at temperatures more than ~ 650 °C. The release of OH<sup>-</sup> species at the surface, however, starts at lower temperatures [16].

### **2.7.3 Incorporation with hydride**

H<sup>-</sup> ion is one of the strongest reducing species [25]. Applying an external electric field on C12A7:H<sup>-</sup> at high temperatures (approximately 700 °C) leads to H<sup>-</sup> ion emission from the material [24, 87].

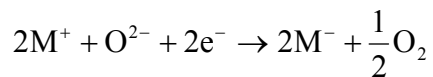
The ultraviolet irradiation of H<sup>-</sup>- incorporated C12A7 results in the photoionization of H<sup>-</sup> ions into H<sup>0</sup> and electrons. The H<sup>0</sup> atom is unstable and ionizes to H<sup>+</sup> which in turn forms OH<sup>-</sup> ion with a cage-wall oxygen plus an electron which occupies the empty space inside the cage, or bonds with an extra-framework oxygen ion and adds to the number of entrapped OH<sup>-</sup> ions and electrons. The latter mechanism is more favoured in terms of energy [16, 88]. This phenomenon is further explained in section 2.8.1.

### **2.7.4 Incorporation with heavy metal ions**

The introduction of heavy metal anions (M<sup>-</sup>) with compatible sizes to the cage space, such as Au<sup>-</sup>, can lead to new fields of applications such as low

temperature oxidation reactions. Au<sup>-</sup> anions are heavy metal species with unique catalytic properties suitable for oxidation reactions, such as low temperature formation of CO<sub>2</sub> from CO [41].

The M<sup>+</sup> ions are incorporated into the C12A7 structure by hot implantation and in the presence of an electron source. The entrapped oxygen ions are released as oxygen gas and M<sup>-</sup> anions remain inside the lattice with one anion in each filled cage according to the following chemical reaction [41]:



The maximum concentration of these monovalent species is 4 ions per unit cell. If the concentration of the implanted anions exceeds this value, the rest of the empty cages will be filled with metal atoms (M<sup>0</sup>) and if this concentration exceeds the amount of framework cages, i.e. 12 atoms per unit cell, metal clusters will form inside the structure. The formation of metal clusters can damage the structure of C12A7 [41].

### **2.7.5 Incorporation with fluoride**

Fluoride anion has potential applications in various fields, such as semiconductor etching, filming and material modification. F<sup>-</sup> ion beam can also be used in hot ion implantation, inertial confinement fusion and particle acceleration [89]. Anion implantation has attracted attention recently, since anions have negative polarity and low affinity for electrons, and therefore, surface charging up of the implanted target is negligible compared to hot implantation of cations [64, 89].

The unique structure of C12A7 allows for the storage of a high concentration of F<sup>-</sup> anions and emission of these species under suitable temperature and extraction electric fields. The F<sup>-</sup>-incorporated C12A7 can be produced by the solid reaction of CaCO<sub>3</sub>, Al<sub>2</sub>O<sub>3</sub> and CaF<sub>2</sub>. The solid ingredients are mixed with a molar ratio of 11:7:1. The mixture is pressed and sintered at 1350 °C for at least 8 hr and the pressed sample is annealed at 780 °C under the flow of F<sub>2</sub>/Ar gas [89].

The anion emission from C12A7 is increased by increasing the temperature and/or extraction electric field due to the enhancement of anion diffusion and desorption from the material surface.

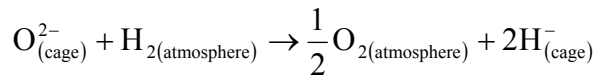
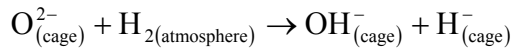
The emission decays with an increase in the emission time as a result of F<sup>-</sup> ion extraction from the material. Therefore, a fluorine gas source is required in order to introduce more F<sup>-</sup> anions into the structure and achieve a relatively pure and stable F<sup>-</sup> ion beam. A supplement of a fluorine/argon gas mixture and a source of electrons by applying a low direct electric field on one side of the material can produce F<sup>-</sup> ions at the surface, which diffuse into the lattice by field-enhanced thermal diffusion and provide the material with more F<sup>-</sup> anions to be emitted [64].

## **2.8 Electron-incorporated C12A7 fabrication techniques**

As mentioned earlier (section 2.3), the incorporation of electrons in place of extra-framework oxygen ions in C12A7 converts the material from an insulator to a semiconductor and conductor. In this section, various methods of electride formation are introduced and explained in detail.

### 2.8.1 Heat treatment in a reducing atmosphere of H<sub>2</sub> plus UV irradiation

This treatment starts with heating the sample up to 1200–1300 °C for typically 1 hr in a 20% H<sub>2</sub> – 80% N<sub>2</sub> atmosphere [9, 90, 91]. At high enough temperatures, the hydrogen molecules in the atmosphere start reacting with the trapped O<sup>2-</sup> ions and H<sup>-</sup> species replace these ions inside the cages. Two chemical reactions can be responsible for the formation of H<sup>-</sup> ions in the structure as follows [40]:



The H<sup>-</sup>-incorporated C12A7 is still colourless and insulating [9]. However, subsequent irradiation with ultraviolet light (wavelength of ~ 300 nm) can ionize H<sup>-</sup> and produce H<sup>0</sup> and electron inside the cage, hence transforming the material into a conductive oxide [88]. The entrapped electrons are loosely bound to the structure and can migrate via hopping [40]. Furthermore, by applying a high enough electric field, electrons are extracted from the cages and emitted at low temperatures.

Since H<sup>0</sup> atoms are unstable, they either join to form H<sub>2</sub> molecules or dissociate into H<sup>+</sup> and H<sup>-</sup> pairs. H<sup>+</sup> ions are then bonded to nearby framework or extra-framework oxygen ions forming OH<sup>-</sup>, while H<sup>-</sup> ions are incorporated inside the empty cages leading to more photoionization and higher electron concentrations [40, 92]. Therefore, the concentration of OH<sup>-</sup> might also increase slightly as a result of this heat treatment [24].

The electrical conductivity persists even after the irradiation is decreased. The insulating-to-conducting transformation is accompanied by the appearance of two optical absorption peaks at 0.4 and 2.8 eV. The incorporation of H<sup>-</sup> ions inside the structure also shifts the optical absorption edge of the material from 5 eV to ~ 4 eV and changes the colour of the material from colourless to green [9, 24]. The absorption intensity and the conductivity increase with increasing the irradiated-photon dosage [24].

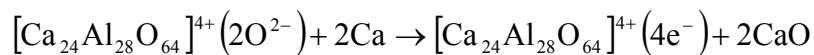
Insulating-to-conducting transformation in C12A7:H<sup>-</sup> is also possible via electron beam irradiation as an alternative to UV irradiation. In this case, the energy dissipation of the primary electrons is responsible for the formation of electron-hole pairs inside the structure. The pairs act as intermediate states that transfer energy to the entrapped H<sup>-</sup> ions and result in the ionization of these species [45, 91].

Previous reports show that conductivities up to 10 S.cm<sup>-1</sup> can be achieved via this technique which maintains up to 320 °C [25]. However, a further increase in the temperature causes the H<sub>2</sub> molecules to recombine with the entrapped electrons and the conductivity starts to decrease, although conductivities up to 0.5 S.cm<sup>-1</sup> are preserved at temperatures as high as 600 °C [40]. In other words, insulating-conducting conversion is reversible as long as the temperature is not high enough for the H<sup>-</sup> ions to be released. In general, the heat treatment of conductive C12A7 at 500 to 750 °C in an inert gas atmosphere transforms the material back to insulating [9, 24].

## 2.8.2 Heat treatment in a metal-vapour atmosphere

The idea of this technique comes from the fact that at a high enough temperature, the affinity of some metals to react with oxygen and form a metal oxide is quite high. The heat treatment of C12A7 in the presence of a metal under vacuum results in the reaction of the metal with  $O^{2-}$  ions inside the cages, while electrons are left behind in order to maintain the charge neutrality of the structure [93].

A schematic illustration of insulating-conducting conversion of C12A7 is shown in figure 2.17. The heat treatment of the compound at a temperature of 700 °C in presence of calcium results in the formation of CaO layer on top of C12A7. Once the top layer is removed, an electron-incorporated C12A7 is obtained. The reaction between C12A7 and calcium metal can be expressed as [93]:



The transformation of C12A7 from an insulator to a conductor can be noticed by the change of the sample colour and could be proven by the appearance of optical absorption bands at 0.4 and 2.8 eV.

Calcium heat treatment for 1-2 weeks can produce conductivities as high as  $100 \text{ S.cm}^{-1}$  at room temperature, which is considerably higher than  $H_2$  heat treatment-plus-UV irradiation technique [25, 40].

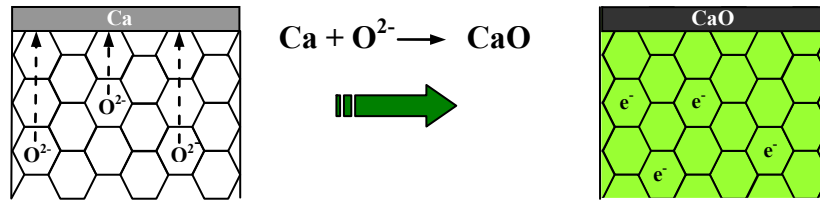
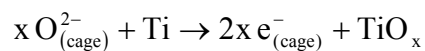


**Figure 2.17 Schematic illustration of electron incorporation mechanism in C12A7 via heat treatment in presence of calcium metal. The extra-framework oxygen ions diffuse to the ceramic-metal interface and oxidize Ca leaving electrons behind in order to compensate for the lack of negative charge of the ceramic framework [40].**

This method is only applicable to single crystals and cannot be used for polycrystalline structures and thin films. In addition, the heat treatment process is time consuming and hence not efficient for large-sized sample fabrication [93].

Titanium can also be used as the reducing agent. The heat treatment is carried out at a temperature of 1100 °C for 24 hr [94] and it has been proved to be more efficient in terms of replacing the oxygen ions and hence reducing the process duration [47, 93, 95]. The following reaction shows the chemical reduction of C12A7 in presence of titanium metal vapour [93]:



An electron concentration of approximately  $1 \times 10^{21} \text{ cm}^{-3}$  can be achieved through this process [93].

The heat treatment of C12A7 at 1000 °C for 24 hr under a vacuum of approximately  $10^{-4}$  torr in presence of vanadium can produce similar results [2].



### 2.8.3 Melt-solidification and glass-ceramic processing in a reducing atmosphere

It has been previously mentioned (section 2.1.2) that the presence of oxygen or hydroxide templates in the atmosphere is essential for the formation of C12A7 [2]. On the other hand, it is also possible to produce electron-incorporated C12A7 directly from the melt under a reducing atmosphere. The choice of a proper reducing atmosphere that can provide the melt with a new template ion is of utmost importance. The previous reports show that  $C_2^{2-}$  ion can act as a new template in a reducing atmosphere and leave electrons inside the structure, hence transforming C12A7 to an electride [1, 93].

The melt-solidification technique consists of two melt and solidification steps under a strongly reducing atmosphere (figure 2.18(a)). C12A7 powder is first melted in a carbon crucible by heating the powder up to 1600 °C in air and holding it at this temperature for approximately 1 hr. This temperature is high enough to produce a reducing atmosphere inside the carbon crucible [1].

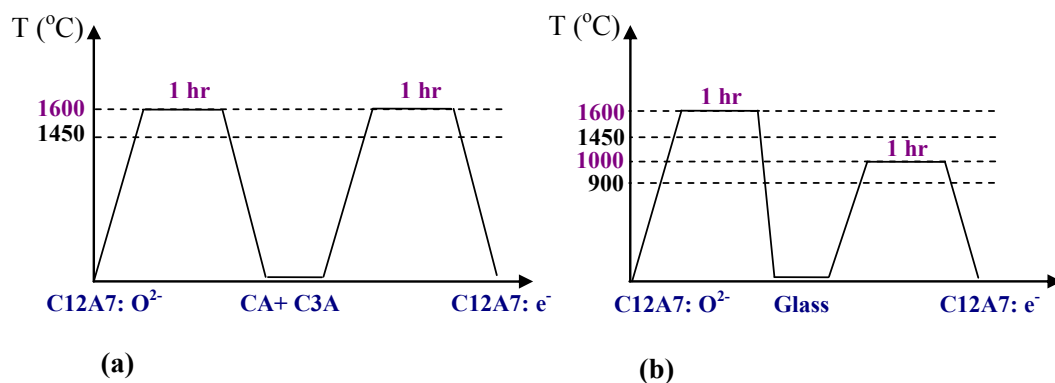
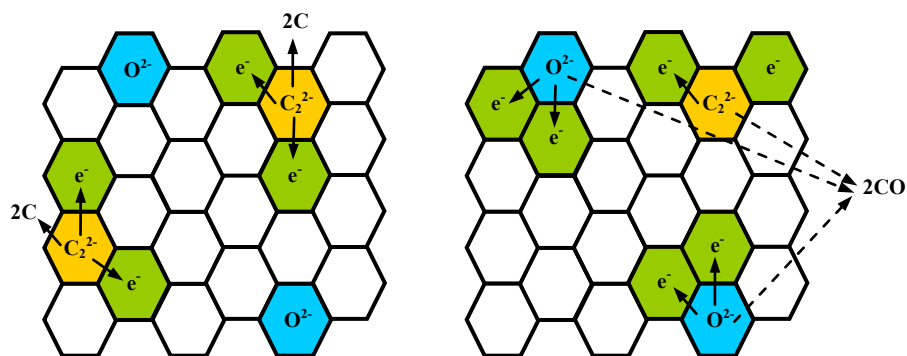


Figure 2.18 Schematic illustration of (a) melt-solidification treatment [96], and (b) glass-ceramic processing [49] of C12A7 under the reducing atmosphere. The temperatures of 900 and 1450°C are the crystallization temperature and the melting point of C12A7 respectively.

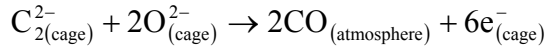
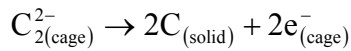
During the first step of the process, the trapped oxygen ions are extracted from the structure due to the reducing nature of the atmosphere. The absence of oxygen templates and the lack of any other templates in the reducing atmosphere eventually lead to the decomposition of C12A7 and the formation of a binary eutectic phase of C3A and CA. At the same time,  $C_2^{2-}$  is introduced into the melt and forms  $CaC_2$  in the resulting solid [1, 49, 93].

During the second step, however,  $C_2^{2-}$  ion is dissolved in the melt and acts as a template for the formation of C12A7 in the reducing atmosphere. The suggested mechanism is that  $C_2^{2-}$  ions replace the role of oxygen templates to form C12A7, but  $C_2^{2-}$  ions are only stable during the initial stage of crystallization and disappear from the final crystal after the completion of the second melt-solidification step. These ions are instead extracted from the cages either as solid carbon atoms or CO gas and leave electrons behind inside the cages. A schematic illustration of C12A7 electride formation is shown in figure 2.19.



**Figure 2.19 Schematic illustration showing the formation of C12A7 electride in a reducing atmosphere with  $C_2^{2-}$  ions acting as templates for oxygen ion removal [1]**

The incorporation of electrons occurs through the following reactions [1, 93]:



This technique can be used for efficient fabrication of bulk polycrystalline C12A7 electrides [1].

Glass-ceramic processing is another two-step method to produce a C12A7 electride from the insulating powder in a reducing atmosphere. This process is shown schematically in figure 2.18(b). The first step includes melting C12A7 powder in a carbon crucible at a temperature of 1600 °C, which is almost similar to the melt-solidification process except for the fact that the melt is quenched from high temperature and a transparent glass is formed. The  $C_2^{2-}$  ions are also introduced into the glass.

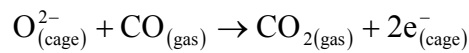
The glass formed during the first step of the process can transform into crystalline C12A7 via heat treatment under vacuum for 1 hr at 900 – 1000 °C, which is higher than the glass-transition temperature, while  $C_2^{2-}$  ions act as templates for the incorporation of electrons inside C12A7 crystal [93, 96].

#### **2.8.4 Heat treatment in a reducing gas atmosphere of CO/CO<sub>2</sub>**

As mentioned in section 2.8.1, the heat treatment of C12A7 in a reducing atmosphere containing H<sub>2</sub> followed by UV irradiation makes the material conductive. Another way of substituting oxygen ions with electrons is the heat treatment of C12A7 in a reducing gas atmosphere of CO/CO<sub>2</sub> gas mixture. The

heat treatment is carried out using a carbon crucible at a temperature between 1000 and 1200 °C for typically 24 hr under the flow of an inert gas. The carbon crucible can produce a strongly reductive atmosphere of CO/CO<sub>2</sub> (with partial pressure of oxygen less than 10<sup>-15</sup> atm) upon heating.

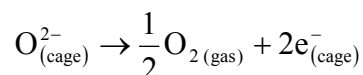
At a high enough temperature, CO gas in the atmosphere starts reacting with oxygen ions inside the structure forming CO<sub>2</sub>, while the oxygen vacancies are filled with electrons instead in order to neutralize the positive charge of the framework. The reaction process takes place as follows [93]:



This process can be used for different types of C12A7 including single crystal, powder, and thin films [93].

### **2.8.5 Hot implantation of inert-gas ions**

The implantation of energetic gas ions, such as Ar<sup>+</sup> or Xe<sup>+</sup>, at high temperatures is a non-equilibrium physical process that can be used to transform an insulating C12A7 to an electride [27]. In this technique, the material in form of a thin film is put under vacuum and Ar<sup>+</sup> ions are shot at temperatures as high as 600 °C. The ions hitting the material collide with the trapped oxygen ions and extract them, leaving free electrons behind inside the cages [47, 93], according to the following reaction:



This process does not damage the structure of the lattice [27, 42, 47, 93], but the stability of the structure is only retained if the implantation is done at high

temperatures and a room-temperature implantation will result in the conversion of the material to an amorphous [93].

In order for oxygen ions to leave the lattice, the fluence of Ar<sup>+</sup> ions should not be less than  $1 \times 10^{17} \text{ cm}^{-2}$ . Although the ion-implanted C12A7 with low Ar<sup>+</sup> fluence shows insulating properties, the conductivity increases after UV irradiation (similar to the material heat treated in H<sub>2</sub> atmosphere) [47].

### **2.8.6 Chemical reduction treatment using oxygen-deficient amorphous C12A7**

In this technique, a layer of C12A7 film is produced on an MgO single crystal substrate via pulsed laser deposition of a C12A7 target plus a subsequent crystallization heat treatment. Then, a thin layer of amorphous C12A7 is deposited on top of the polycrystalline film at 700 °C under the vacuum (oxygen pressure of less than  $10^{-3} \text{ Pa}$ ). The templates needed for the crystallization of this amorphous layer is provided by the crystalline film. However, the electrons are left behind in order for both layer structures to maintain their charge stability. The top layer is then removed via chemical-mechanical polishing [49]. Conductivities as high as  $800 \text{ S.cm}^{-1}$  can be achieved using this method [47].

### **2.8.7 Hot proton implantation plus UV irradiation**

Another method of H<sup>+</sup> ion incorporation into C12A7 structure is H<sup>+</sup> ion (proton) implantation. In this technique, a C12A7 target is bombarded with H<sup>+</sup> ions at around 600 °C and irradiated with UV light. The ion incorporation process is thermally assisted. A number of implanted H<sup>+</sup> ions react with OH<sup>-</sup> species inside the cages while the remaining implanted H<sup>+</sup> ions capture two

electrons to compensate for the positive charge of the lattice and stabilize the structure.

The  $H^-$  species entrapped inside the structure are photoexcited via UV light irradiation and are released as  $H_2$  molecules, leaving electrons behind.

The electrical conductivity increases with the increase in temperature up to room temperature. At implantation temperatures higher than 600 °C, the material is fully incorporated with  $H^+$  species and becomes saturated [42].

## **2.9 Applications of C12A7**

- **Amorphous and crystalline C12A7**

Calcium-aluminate glasses have potential applications for mid-infrared optical fibres and information storage devices [6, 74]. These materials have a superior infrared transmittance compared to other oxide glasses plus the scattering loss for these oxides is small. These advantages make them good candidates for use as mid-infrared fibres. Other potential applications of these glasses include photometric devices for information storage due to photosensitivity [70].

Crystalline C12A7 can be used in solid oxide fuel cells. The body used in such an application should be dense enough to prevent the penetration of gases [18]. The application of C12A7 as a support for partial oxidation of methane into syngas has also been considered. The product of the oxidation has a  $H_2/CO$  molar ratio of 2:1 and therefore can be used as a feedstock for methanol and Fischer-Tropsch syntheses [97].

The transparency of C12A7 is advantageous in optical windows for light sources [18]. This compound is also an ionic conductor [8] with potential applications as an ion conducting solid electrolyte [39].

C12A7-doped indium tin oxide (C12A7:ITO) is a new transparent cathode with applications in top-emission and transparent organic light-emitting diodes (OLEDs) [98].

- **Electron-incorporated C12A7**

C12A7 can be converted to an electride because of its unique nanoporous cage structure while retaining its chemical and thermal stability at room temperature [1, 2]. Different types of applications for electrides include reducing agents, cold-cathode electron field emitters, thermionic power generators and refrigeration devices [1, 2, 25, 46]. The conductive C12A7 can also be used for direct optical signature of conducting wires in insulating transparent media and high density optical memory [19]. Electron-incorporated C12A7 is known as a transparent conductive oxide (TCO) with various applications such as in flat panel displays, solar cells, transparent transistors, electrochromic devices, smart windows and flexible electronics, although the mechanism of conductivity in this material is quite different from other common TCOs [2, 8, 23, 40, 42]. This compound has also been successfully used as a cathode material in OLEDs [99].

Semiconductive C12A7 can be used in conventional field effect transistors (FETs) [46].

The reversible insulating-to-conducting conversion in UV-induced semiconducting C12A7:H<sup>-</sup> is desirable in optoelectronic applications such as in rewritable electric circuits [42]. Another advantage of this technique is that

conductive wires can be applied on insulating transparent media by direct optical writing and a high optical memory can also be achieved [24].

- **Ion-incorporated C12A7**

Different types of anion species can be stored inside the cage structure of C12A7 and can be emitted under appropriate temperatures and extraction fields. The anion-incorporated C12A7 has potential applications in a one-step synthesis of phenol from benzene, reduction of NO, fast micro-organisms inactivation, steam reforming or oxidation of oxygenated organic compounds, increasing the surface hydrophilicity of polymers by producing hydrophilic hydroxyl and carbonyl compounds, and low-temperature surface oxidation of silicon [89, 100].

Superoxide-incorporated C12A7 is a powerful oxidizing catalyst with potential applications in organic compounds (hydrocarbons) combustion, biochemical reactions and as a solid electrolyte with catalytic activity [8, 20, 24, 39]. Mg-doped C12A7:O<sup>-</sup> has been reported to have a very high activity for hydrogen generation from the catalytic steam reforming of bio-oil, naphtha and methane at relatively low temperatures [101, 102]. C12A7:O<sup>-</sup> doped with potassium has also been considered for the production of hydrogen from the steam reforming of ethanol as well as NO gas reduction [103, 104].

Nano/micro particles of C12A7 with entrapped oxygen radicals are more appropriate for catalyst applications because of the high oxidizing power and the large surface area of the particles. A solution process can be used in order to fabricate these particles [29].

C12A7 is also a promising material as a source of O<sup>-</sup> ion emission [3, 39], which can be utilized in desulfurization of flue gas. The ions consumed in the



process can also be recovered using electrocatalytic reactions and make the material reproducible [3].

Fluoride anion emission from  $C12A7:F^-$  can be utilized in semiconductor etching, filming, material surface modifications, inertial confinement fusion, atmospheric chemistry and particle acceleration [64, 89]. Introduction of heavy metal anions ( $M^-$ ) with compatible sizes to the cage space can lead to new fields of applications such as low-temperature oxidation of methane [27].

# Chapter 3

## Experimental procedure

### 3.0 Introduction

This chapter presents the sample fabrication procedure via sol-gel technique, giving full explanation of the variables considered in solution preparation. All the methods and instruments used in the microstructural and chemical composition analyses and the optical characterization of the final products are described. The selected parameters for all the measurements are also provided in this chapter.

### 3.1 Solution preparation

The solutions were prepared using aluminium sec-butoxide and calcium nitrate tetrahydrate as the main precursors of aluminium oxide and calcium oxide respectively [68]. The preparation steps are shown in figure 3.1.

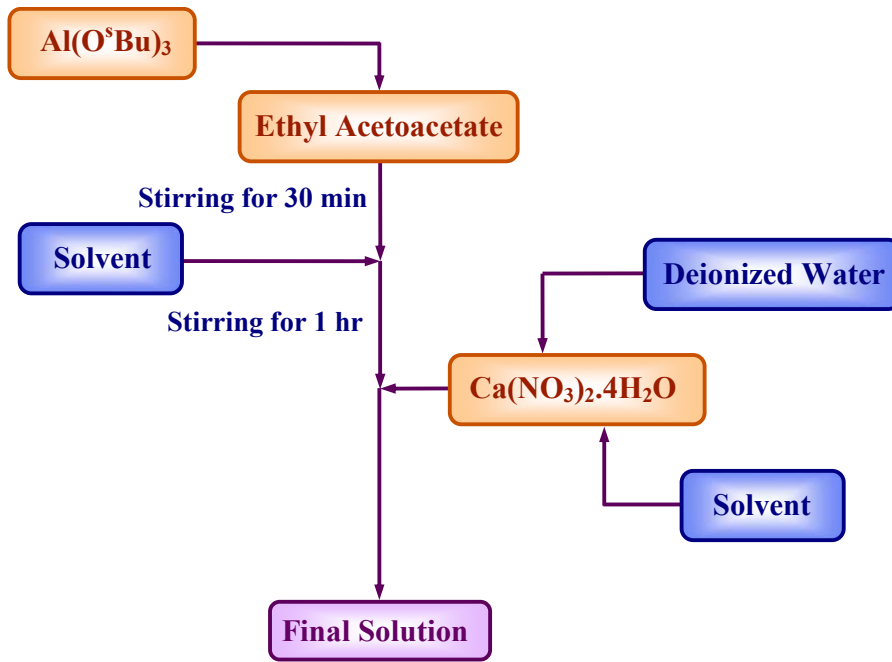


Figure 3.1 Schematic illustration of solution preparation

Weight percent of the main ingredients, aluminium-sec butoxide (ASB) and calcium nitrate tetrahydrate, were calculated according to the position of C12A7 in CaO-Al<sub>2</sub>O<sub>3</sub> binary diagram (figure 3.2) and used as the measuring unit for the preparation of the solution. Requisite variable parameters considered in solution preparation are shown in table 3.1.

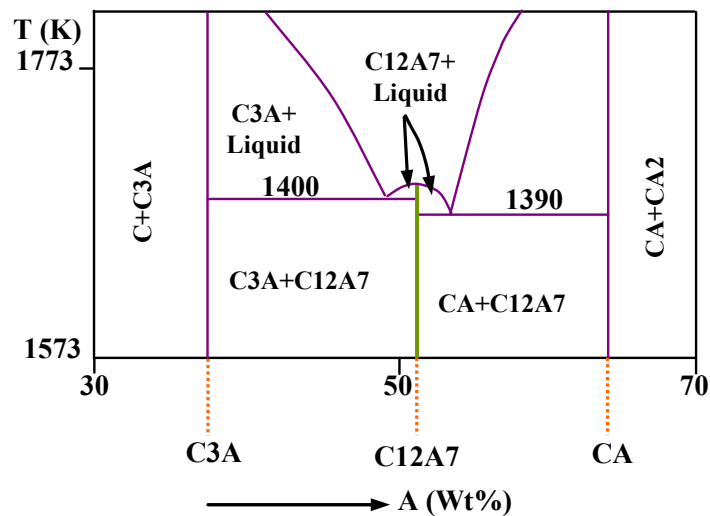


Figure 3.2 Partial phase diagram of the binary CaO-Al<sub>2</sub>O<sub>3</sub> system [10]

**Table 3.1 Molar ratios of the ingredients used for solution preparation. The ratios marked with \* belong to the molar ratios of isopropyl alcohol; while methanol is used as the solvent in the rest of the solutions.**

<i>Number of solutions</i>	<i>Variable solution molar ratios</i>			
	<i>EAA to ASB</i>	<i>Solvent to ASB</i>	<i>Solvent to Ca(NO<sub>3</sub>)<sub>2</sub></i>	<i>H<sub>2</sub>O to ASB</i>
Sol1	3:1	40:1	40:1	10:1
Sol2	3:1	20:1	20:1	10:1
Sol3	2:1	20:1	20:1	10:1
Sol4	2:1	20:1	20:1	5:1
Sol5	2:1	10:1*	10:1*	5:1
Sol6	2:1	5:1	5:1	5:1

Ethyl acetoacetate (EAA) was chosen as the chelating agent with two different ratios of EAA to ASB in order to investigate the role of chelation on hydrolysis and solution stabilization. First step of the solution preparation consisted of the addition of aluminium sec-butoxide to ethyl acetoacetate (figure 3.1). Since the affinity of aluminium sec-butoxide to absorb water is quite high, the addition of alkoxide to EAA was done using a syringe to minimize the exposure of the precursor to air.

EAA-to-alkoxide molar ratios of 3:1 and 2:1 were chosen based on previous studies [68, 77]. The mixture was kept stirring for 30 min at ambient temperature before the addition of other ingredients.

Since aluminium sec-butoxide is highly sensitive to the presence of water, the addition of water to the solution results in rapid hydrolysis of the alkoxide and precipitation of alumina. Therefore, the addition of an organic solvent is important in order to control the hydrolysis rate. Methanol was initially chosen as the solvent for aluminium sec-butoxide and calcium nitrate. However, the

solvent was later changed to isopropyl alcohol due to a better solubility of the main precursors in this organic solvent [68] which lead to a significant improvement in the quality of the final products. The solvent-to-alkoxide molar ratios of 40:1, 20:1, 10:1 and 5:1 were chosen for different solution recipes. The choice of these molar ratios was made based on the microstructural observations of the surfaces. The effect of the amount of solvent on the quality of the films was investigated with a view to optimizing the solution recipe. The solvent was added to the alkoxide-EAA mixture dropwise and the solution was left stirring for 1 hr in each case.

Deionized water was added to the solution as the hydrolysis agent for the alumina precursor. The minimum water-to-alkoxide molar ratio has been reported to be 3:1 theoretically for a complete hydrolysis to take place [77]. Two water-to-alkoxide molar ratios of 10:1 and 5:1 were chosen to ensure a complete hydrolysis of the precursor and observe the effect of water content on the microstructure and the extent of hydrolysis. The water content of calcium nitrate tetrahydrate was also taken into account for the calculations.

The amount of calcium nitrate tetrahydrate for C12A7 fabrication in the form of powder and thin films was calculated based on the stoichiometric weight percent of CaO and Al<sub>2</sub>O<sub>3</sub> in C12A7. The weight ratio of aluminium sec-butoxide to calcium nitrate was determined to be 1.2169.

The molar ratio of solvent to nitrate was also kept the same as the solvent-to-alkoxide molar ratio and the water needed for hydrolysis was added to the nitrate solution. Upon the dropwise addition of this solution to the aluminium sec-butoxide solution, white colloids were observed which showed that the hydrolysis was taking place. It has been mentioned in previous studies that the

addition of hydrochloric acid or nitric acid to the hydrolyzed mixture is necessary in order to peptize the precipitates and obtain a clear solution [70, 73, 80]. However, in all cases of this investigation, a transparent solution was obtained after 1-2 min of stirring and there was no need for the addition of acid to the solution. In the case of solution preparation using isopropyl alcohol as the solvent, the precipitates were barely noticeable and the solution remained transparent during the whole process. All the solutions were tested to remain stable for at least 2 months without any loss of transparency.

### **3.2 Sample preparation**

Samples were prepared in form of thin film and powder. Spin coating technique was utilized for thin film preparation and drop casting was also applied in order to obtain films with higher thicknesses.

- **Substrate cleaning**

Magnesium oxide single crystal was chosen as the substrate for C12A7 film preparation. All the substrates were squares in shape with dimensions of 10 mm × 10 mm and thickness of 0.5 mm. All the substrates were washed thoroughly with distilled water and methanol and then sonicated in deionized water for 5 min. The substrates were then dried and kept in sealed Petri dishes to minimize contamination before the thin film application.

- **Thin film**

Thin films were prepared using a KW-4A spin coater provided by SPI Supplies. Spin coating rates of 1000, 2000 and 3000 rpm and spinning time of

30 s were used for the preparation of spin-coated samples. All the samples were left drying slowly in sealed Petri dishes for at least 2 days prior to the heat treatment.

Samples were also prepared using drop casting technique. A few drops of solution were applied to the surface of the substrates until the whole surface was covered with the solution. These samples were also kept in sealed Petri dishes for minimum 2 days.

- **Thickness measurement**

The thickness of the films on MgO substrates were measured by means of a Dektak 150 surface profiler provided by Bruker and a Woolam M – 2000 V<sup>TM</sup> spectroscopic ellipsometer.

A profiler utilizes a surface contact measurement technique for measuring step heights or trench depths on a surface by dragging a very low force stylus across the surface.

Ellipsometry is a non-destructive and sensitive technique for measuring the optical properties of materials. In this method, the changes in the polarization of the light reflected from a sample surface are measured. The polarization change of the reflected light is characteristic of the surface structure of the sample. These changes, in terms of psi ( $\Psi$ ) and delta ( $\Delta$ ), are then utilized in order to extract the optical parameters of the sample and determine the thickness of the film. The measured  $\Psi$  and  $\Delta$  are fitted to the proper dispersion model. A computer program is normally used in order to search for a set of variable parameters of the dispersion model such that the calculated  $\Psi$  and  $\Delta$  would

match the measured data. The optical parameters and thickness of the film are then extracted using the calculated data [105].

Spectroscopic ellipsometric measurements of C12A7 films were performed in the spectral wavelength range of 360–1000 nm. The angle of incidence was fixed at 60°. The instrument consisted of a quartz tungsten halogen lamp source, a stepper motor driven rotational stage housing a polarizer and CCD detector unit.

- **Powder**

In order to produce samples in powder form, some amount of solution was exposed to air at room temperature for at least one day. The gelation occurred gradually and a clear gel was obtained. The dried gel was then crushed and milled into white powder.

### **3.3 Heat treatment**

The thin films were isothermally annealed at 1100 and 1300 °C under air atmosphere. The heat treatment durations were chosen practically based on the results of the phase analysis. The heating rate was kept at 10 °C/min and the samples were kept in the furnace after the completion of the heat treatment in order to minimize the cooling rate.

A subsequent heat treatment was also applied to a few of the crystallized thin films at 1300 °C for 2 hr under a reducing atmosphere of 5%H<sub>2</sub>-95%N<sub>2</sub> and rapid cooling to room temperature.



The dried powder was heat treated in a temperature range of 700 to 1300 °C for at least 6 hr in order to investigate the effect of heat treatment temperature and time on the formation of C12A7 and other possible secondary phases.

The crucible was selected according to the effect of the crucible material on the surrounding atmosphere. An alumina crucible was used for the crystallization heat treatment of the thin films and powder. Crucible materials which provide a reducing atmosphere, such as graphite, will result in the formation of C3A+CA eutectic mixture instead of crystalline C12A7. A silica crucible was employed for the heat treatment under the 5%H<sub>2</sub>-95%N<sub>2</sub> reducing atmosphere.

### **3.4 Microstructural observations**

The surface of the thin films was observed using JEOL JSM-6300 field-emission scanning electron microscope (FESEM) in a magnification range of 50 – 50000X in order to investigate the effect of the amount of solvent, the chelating agent (Ethyl acetoacetate) and water on the quality of the films and the formation of defects such as discontinuities and cracks.

The essential components of a scanning electron microscope are shown schematically in figure 3.3.

Scanning electron microscopy is a non-destructive surface imaging and analysis technique in which the sample surface is scanned with an electron beam. The energy of the beam can be adjusted in the range of 0.5-40 KeV. The interaction of electrons with atoms produces different types of signals, mostly in form of secondary electrons, which give information about surface topography, chemical composition and other properties of the material. The interaction

volume depends on the energy of the beam as well as the atomic number and the density of the specimen. The data is normally collected over a selected area of the sample surface and a two-dimensional image is produced.

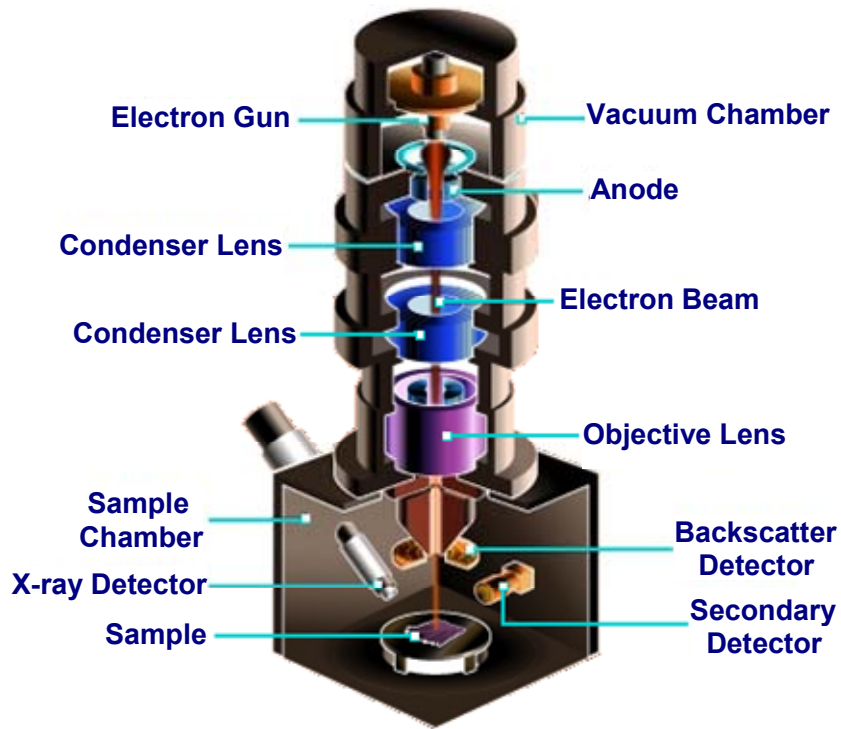


**Figure 3.3 Schematic illustration of scanning electron microscope components [106]**

In a standard electron microscope, electrons are mostly generated by heating a cathode. In a field-emission scanning electron microscope, however, a cold source is employed, i.e. the emission of electrons is caused by a strong electric field applied to the cathode. Since the electron beam produced by a field-emission source is considerably smaller in diameter compared to the one of a normal electron microscope, a much higher resolution is obtained and the quality of the images is significantly improved.

The JEOL-6300 SEM uses a field emission gun with a cold cathode. The resolution is 1.5 nm in secondary electron imaging (SEI) and 3.0 nm in backscattered electron imaging (BEI) at 30 kV. The airlock specimen chamber

allows up to a 32 mm diameter sample, and the size can also be up to 150 mm without the airlock.

Since magnesium oxide substrates and the ceramic thin films both have insulating properties, the edges of each sample was joint to the sample holder using conductive carbon cement and the surface was coated with carbon in order to prevent the charging up of the surface during imaging.

### **3.5 Chemical analysis**

#### **3.5.1 Energy dispersive spectroscopy**

The relative quantities of aluminium and calcium were measured using energy dispersive X-ray spectroscopy (EDS). The measurements were done using JEOL JSM-6300 field emission scanning electron microscopy.

Energy dispersive X-ray spectroscopy is an elemental analysis technique in which an electron beam hits the sample resulting in the excitation of an inner-shell electron. The hole formed as a result is then filled with an outer-shell electron and the energy difference between the outer and inner shells is released as an X-ray. A detector converts the emitted X-rays into voltage signals which are measured and analysed. The accuracy of the analysis is affected by various factors such as over-voltage settings, overlapping of the peaks and the nature of the sample. In addition, elements with atomic numbers less than 4 cannot be detected by this method. This type of analysis is especially useful in quantitative or semi-quantitative determination of the chemical composition.

The samples used for this purpose were coated with carbon to prevent the overlapping of the peaks of the conductive coating with those of the actual

material being tested. An electron-beam voltage of 10 KV was chosen for imaging and chemical analysis.

### **3.5.2 X-ray diffraction**

X-ray diffraction (XRD) analysis was employed for the crystallized samples in powder form using Siemens D5000 X-Ray diffractometer. In addition, the diffraction patterns of the dried gel were obtained in a temperature range of 25 – 1200 °C in the course of crystallization treatment using a Panalytical Xpert Pro diffractometer.

X-ray diffraction is a non-destructive technique to determine the crystallographic structure, chemical composition and physical properties of materials by analysing the intensity of the scattered X-ray beam as a function of the incident beam and scattered beam angle [107].

In powder diffraction method, a fine powder is prepared from the crystal and placed in a beam of monochromatic X-ray. The reason for using an X-ray beam is that the diffraction only occurs when the wavelength of the incident beam is of the same order of magnitude as the distance between the atomic arrays in the crystal (typically ~1-1000 Å). Each powder particle acts as a tiny crystal. For each crystallographic plane, there are some particles in the correct orientation to reflect the beam. Upon the X-ray strike, arrays of atoms forming the crystal produce secondary waves in different directions. The secondary waves mostly cancel each other. However, a few of the scattered waves in specific directions are added together forming a scattered beam. A schematic illustration of destructive and constructive scattering is shown in figure 3.4.

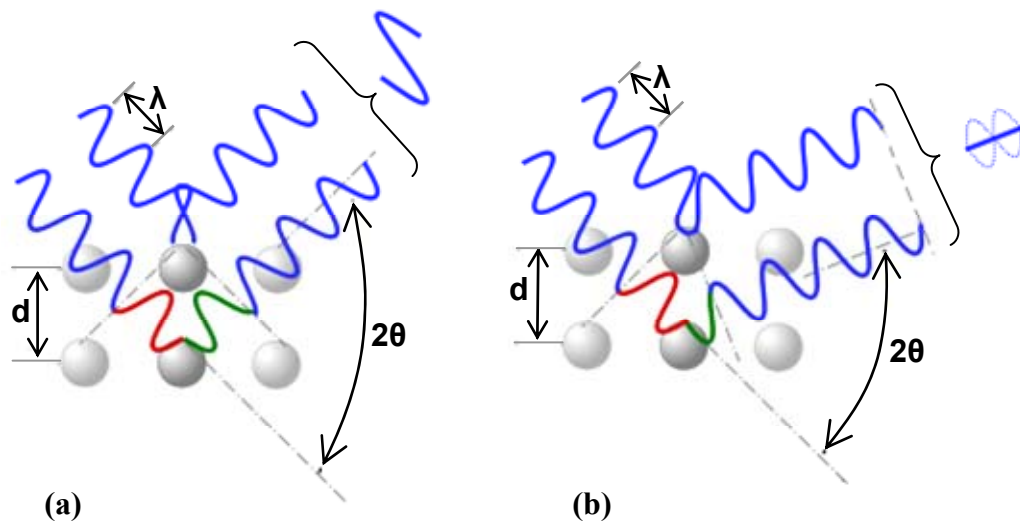


**Figure 3.4 Schematic illustration of (a) constructive scattering which satisfies Bragg's law and (b) destructive scattering of waves which cancel each other [108]**

The diffraction takes place only at those particular angles of incidence which satisfy the Bragg's law [107]:

$$n\lambda = 2d \sin \theta \quad (3.1)$$

where  $d$  is the distance between the scattering planes,  $\theta$  is the incident angle,  $n$  is an integer with the minimum value of 1 and  $\lambda$  is the wavelength of the incident beam.

In order to devise the Bragg's law, either the incident angle or the wavelength is continuously varied during the experiment. In powder diffraction method, the wavelength is fixed and the incident angle is the variable. The angle between the diffracted and the transmitted beam is always  $2\theta$ , also known as the diffraction angle, and this angle is usually measured experimentally.

Samples in powder form were selected for XRD measurements. Since the thickness of the thin films was very small compared to that of the substrate, the X-ray diffraction spectra of the thin film samples showed the diffraction

patterns of the magnesium oxide substrate rather than those of the film. Therefore, the X-ray diffraction technique was only applicable to the powder.

### **3.5.3 X-ray photoelectron spectroscopy**

Thin film samples were analysed using X-ray photoelectron spectroscopy (XPS) in order to determine the chemical composition of the ceramic films. The measurements were done using a VG ESCALAB 210 Photoelectron Spectrometer (figure 3.5).

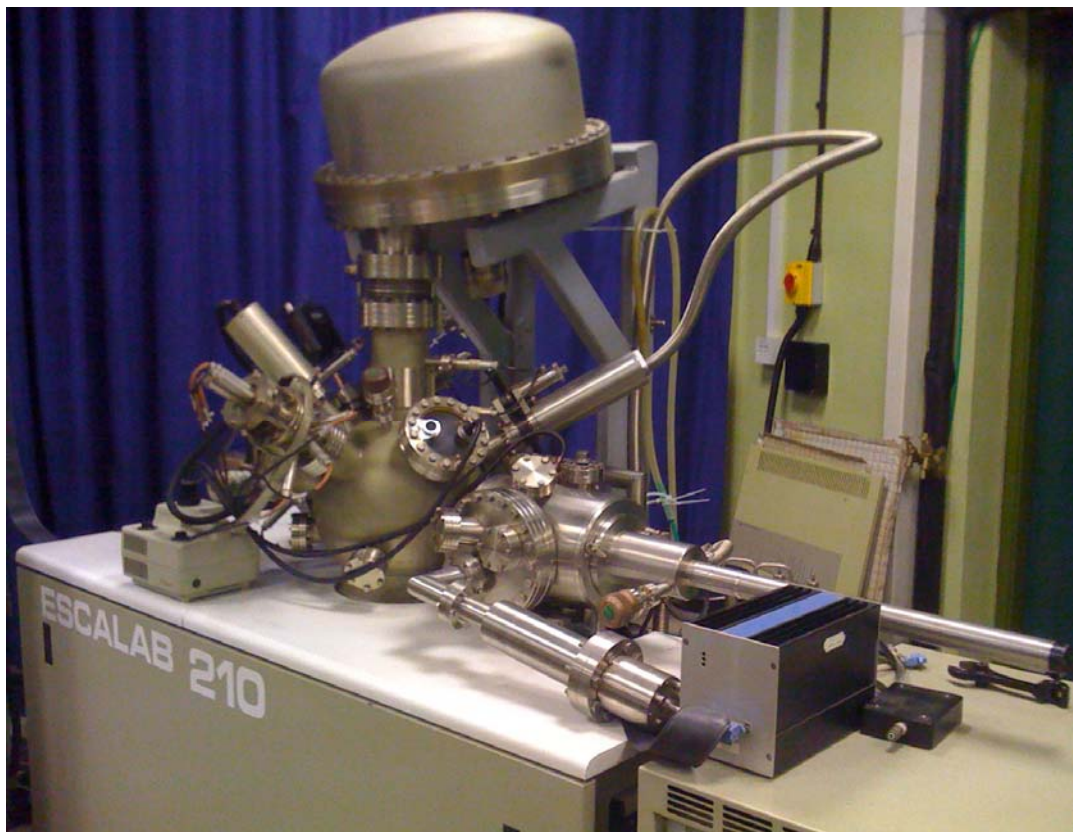


**Figure 3.5 X-ray photoelectron spectrometry setup**

X-ray photoelectron spectroscopy technique uses X-rays within the photon energy range of 200 to 2000 eV in order to analyse the chemical composition and electronic state of the materials. The sample is hit by an X-ray source with a

fixed energy. The photon is absorbed by an atom causing the ionization of the atom and the emission of an inner-shell electron. A schematic illustration of this phenomenon is shown in figure 3.6.

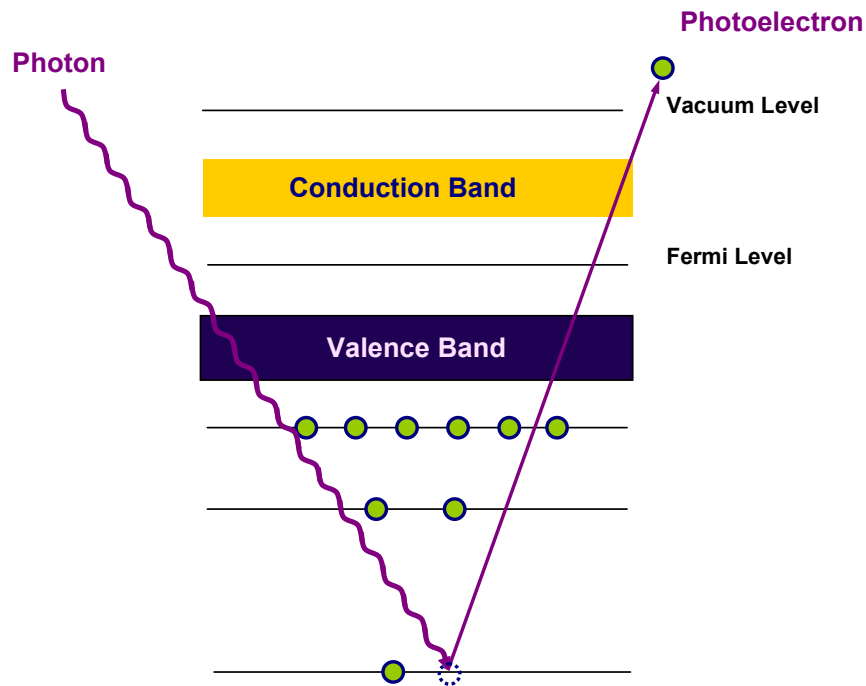


**Figure 3.6 Schematic illustration of X-ray photoelectron spectroscopy [109]**

An ultra-high vacuum is essential in order to prevent the collision of emitted electrons with the gas molecules. The obtained spectrum is a plot of the number of electrons detected per unit of time versus the binding energy of the electrons. The electrons that escape from 1 to 10 nm of the material surface are counted. Each element has a characteristic set of peaks in the spectrum which is determined by the photon energy and respective binding energies. The intensity of the peaks is also related to the concentration of the elements. Therefore, this technique is considered as a quantitative composition analysis.

The electron binding energy of the emitted electrons can be determined by Rutherford equation [110]:

$$E_{\text{Binding}} = E_{\text{Photon}} - (E_{\text{Kinetic}} + \phi) \quad (3.2)$$

where  $E_{\text{Binding}}$  is the binding energy of the electron,  $E_{\text{Photon}}$  is the energy of the incident X-ray photons,  $E_{\text{Kinetic}}$  is the kinetic energy of the emitted electrons and  $\phi$  is the work function of the spectrometer.

The thin films were tested before and after heat treatment to verify the presence of the compounds which are theoretically expected to be formed in the dried gel and the final product. The X-ray source was a non-monochromatic Al  $K\alpha$  source (1486.6 eV), operated with an X-ray emission current of 20 mA and an acceleration voltage of 12 kV. The take-off angle was fixed at  $90^\circ$  with the nominal analysis depth of 10 nm. The area corresponding to each acquisition was a rectangle of  $5\text{ mm} \times 2\text{ mm}$ . Each analysis consisted of wide survey scans (pass energy 50 eV, 1.0 eV step size) and high-resolution scans (pass energy 50 eV, 0.05 eV step size) for component speciation. The numbers of scans were 10 and 5 for the survey spectra and each expansion respectively. The binding energies of the peaks were normalized using the position of the C1s peak at 284.5 eV.

#### **3.5.4 Fourier transform infrared spectroscopy: Attenuated total reflectance**

The phase formation of the thin films as a function of crystallization treatment was further investigated via a Spotlight 400 and a Spectrum 100 FTIR systems provided by Perkin Elmer and equipped with diamond attenuated total reflectance (ATR) accessories. The effect of heat treatment in a reducing atmosphere of  $\text{H}_2\text{-N}_2$  on the FTIR response of the material was also studied.



Fourier transform infrared spectroscopy is a technique in which an infrared spectrum of absorption, emission, photoconductivity or Raman scattering of a sample is obtained. The main difference between this method and absorption spectroscopy is that an incident beam containing different frequencies is used rather than a monochromatic light beam. During each step of the measurement, the intensity of the absorbed beam is measured for a set of incident beam frequencies selected by the device. Once the absorption measurement is complete for the whole frequency range of the incident beam, the obtained raw data is processed and given as the light absorption intensity for each wavelength. The process required to convert the raw data to the final result is in fact an algorithm known as Fourier transform.

Traditionally, infrared spectrometers work by means of transmitting the infrared light through the sample. The attenuated total reflectance technique, which has developed in recent years, overcomes the challenging issues surrounding the traditional infrared spectroscopy, which mainly include sample preparation and spectral reproducibility.

An attenuated total reflectance accessory measures the changes in a totally internally reflected beam during the light-sample interaction. The principle of ATR system operation is shown schematically in figure 3.7.

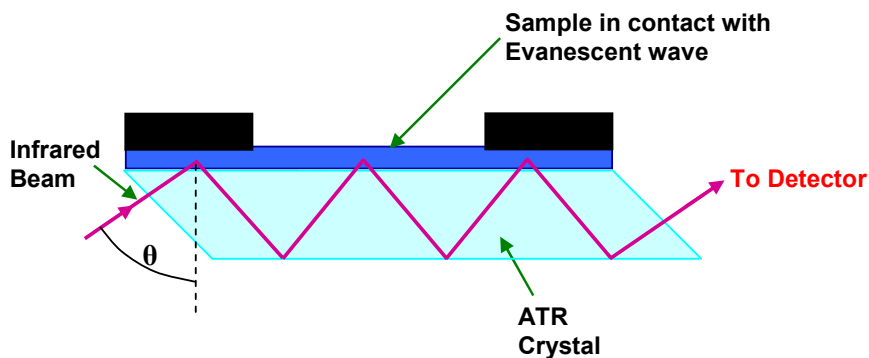


**Figure 3.7 Schematic illustration of ATR system operation [111]**

In this technique, an infrared beam is directed to a dense crystal with a high refractive index, such as diamond, at a certain angle. The internal reflectance of this crystal creates an evanescent wave that enters the sample, which is in contact with the crystal. The penetration of the wave into the sample does not normally exceed a few microns ( $0.5 - 5 \mu\text{m}$ ). The absorption of the infrared beam in certain wavelengths causes the attenuation of the wave, the energy of which is passed back to the infrared beam and exits from the opposite side of the crystal. In order for this method to be effective, the sample must be in direct contact with the crystal. In addition, the refractive index of the crystal must be significantly higher than that of the sample being tested.

Since FTIR-ATR technique mostly gives information about the surface of the material and the depth of penetration is very small, it was found to be very useful in studying the phase analysis of the spin-coated thin films with thicknesses smaller than  $\sim 5 \mu\text{m}$ . The infrared spectra of the films were obtained in a range of  $400 - 4000 \text{ cm}^{-1}$  with a resolution of  $4 \text{ cm}^{-1}$  and accumulation of 100 scans per test. A sample area of  $3 \text{ mm} \times 3 \text{ mm}$  was in contact with the diamond for each measurement and the data was collected at

least 5 times from randomly selected areas of the surface in order to ensure the reproducibility of the results. The ATR stage and the surface of the diamond crystal were cleaned with ethanol before each measurement to prevent the contamination from affecting the results.

### **3.5.5 Raman spectroscopy**

The chemical composition of the drop-casted thin films and powder was studied by means of Nicolet Almega XR Raman spectrometer provided by Thermo Scientific. The spectra were obtained in a range of 40 – 4200  $\text{cm}^{-1}$  for wavenumbers using wavelengths of 532 and 785 nm for the laser beam. The formation of C12A7 and other possible calcium aluminate phases in the powder and thin films as a function of crystallization treatment temperature were determined.

Raman spectroscopy is a non-destructive spectroscopic technique used to study the vibrational, rotational and other low-frequency modes in a system based on the inelastic scattering of a monochromatic light. A laser light, usually in the visible, near-infrared or near-ultraviolet range, is used as the incident beam and interacts with molecular vibrations, phonons and other excitations. The result of these interactions is an upward or downward shift of the laser energy which gives information about the vibrational modes of the system.

The scattered beam is collected by a lens and the wavelengths close to the laser line, which are attributed to the elastic Rayleigh scattering of the laser beam, are filtered via a spectrophotometer. The remaining wavelengths are then sent to a detector.

The interaction between the laser beam and the electrons and bonds of a molecules results in an excitation of the molecule from the ground state to a virtual energy state. The relaxation of the molecule is accompanied by the emission of a photon and a change of rotational or vibrational state of the molecule. The energy difference between this new state and the original state causes a shift in the emitted photon frequency.

A schematic illustration of vibrational energy states involved in Raman scattering is shown in figure 3.8.

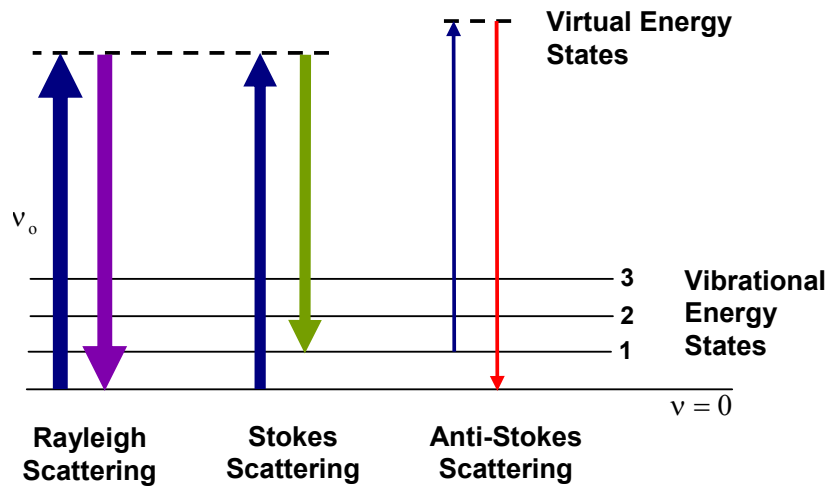


**Figure 3.8 Schematic illustration of the vibrational energy states involved in Raman signal. The thickness of the arrows is a rough indication of the signal strength [112]**

Raman scattering is considered to be an inelastic scattering due to an energy transfer during the photon-molecule interaction. When the incident photon with frequency of  $\nu_0$  is absorbed by a Raman-active molecule in the ground vibrational state, some of the photon energy with frequency of  $\nu_m$  is transferred to the molecule and the scattered light is shifted to a lower frequency of  $\nu_0 - \nu_m$ . This shift in the frequency is also known as Stokes shift.

If the photon energy is absorbed by a molecule which is already in the excited state, the excess amount of energy is released from the molecule upon relaxation and the resulting frequency of the scattered light is increased to  $\nu_0 + \nu_m$ , or anti-stokes frequency.

The Raman shift is typically expressed in wavenumbers. The following formula relates the wavenumbers of shift in the spectrum to the spectral wavelengths:

$$\Delta\omega = \left( \frac{1}{\lambda_0} - \frac{1}{\lambda_1} \right) \times 10^7 \quad (3.3)$$

where  $\Delta\omega$  is the Raman shift in  $\text{cm}^{-1}$ , and  $\lambda_0$  and  $\lambda_1$  are the excitation and Raman spectrum wavelengths in nm, respectively.

Since the vibrational information obtained from Raman spectroscopy is specific to the chemical bonds and the symmetry of the molecules, it can be useful in order to identify the chemical composition of the material.

### **3.6 Differential scanning calorimetry/ thermal gravimetric analysis**

The phase transformations/reactions during the crystallization treatment of the dried gel were identified in a temperature range of 25–1200 °C via differential scanning calorimetry/ thermal gravimetric technique using a Q600 SDT (simultaneous DSC/TGA) provided by TA Instruments.

Differential scanning calorimetry (DSC) is a thermo-analytical technique that measures the difference in the amount of heat required to increase the temperature of a sample and a reference as a function of temperature.

When a sample goes through a physical transformation, such as a phase transition, the amount of heat flow needed to increase the sample temperature with the same rate as the reference will change. The change in the heat flow depends on whether the transformation is exothermic or endothermic. An endothermic transformation results in more heat flow towards the sample and vice versa. The amount of the absorbed or released heat flow during each transition can be measured.

Thermal gravimetric analysis (TGA) determines the changes in the weight as a function of temperature. A derivative weight loss curve can also be obtained that emphasizes the points in which weight loss is more significant. This technique is specifically useful in order to determine the amount of absorbed moisture, the level of organic and inorganic components, and the decomposition of solvent residues in materials.

### **3.7 Optical properties**

#### **3.7.1 Absorbance and reflectance measurements at room temperature**

The absorbance and reflectance spectra of the C12A7 thin films were obtained at room temperature in the wavelength range of 200-900 nm (corresponding to the photon energy of 1.38 to 6.2 eV) using Lambda 950 UV/Vis/NIR spectrometer provided by Perkin Elmer.

Absorption spectroscopy is a technique which measures the optical absorption of materials as a function of frequency or wavelength. Ultraviolet-visible spectroscopy, also known as UV-Vis spectroscopy, is referred to absorption spectroscopy in the ultraviolet-visible spectral range. In other words, the incident light wavelength is varied in the range of visible and near-ultraviolet or near-infrared regions.

The molecules undergo electronic transitions upon absorption of light and the photon energy of the electrons excitation from the ground state to the excited state is measured. The absorption spectrum is normally a plot of absorbance or transmittance versus wavelength. The relationship between the absorbance and incident/transmitted light can be expressed by Beer-Lambert law [113]:

$$A = -\log_{10}\left(\frac{I}{I_0}\right) \quad (3.4)$$

where A is the absorbance and I and  $I_0$  are the transmitted and incident light intensities respectively.

The absorbance is related to transmittance according to the following equation:

$$A = -\log_{10}\left(\frac{\%T}{100\%}\right) \quad (3.5)$$

where T is the transmittance usually expressed in percentage.

Some of the transmitted beam might deviate in relation to the incident beam. A correct transmittance measurement is only possible when the deviated transmitted beam is also taken into account, otherwise the transmitted beam might not be fully picked up resulting in a loss of output signal. The overall

transmittance measurement, i.e. the sum of direct and diffuse transmittance can only be measured using an integrating sphere. The use of an integrating sphere is also necessary when measuring the total reflectance. A schematic configuration of the integrating sphere in transmission and reflection modes and the position of the sample in each type of measurement are shown in figure 3.9.

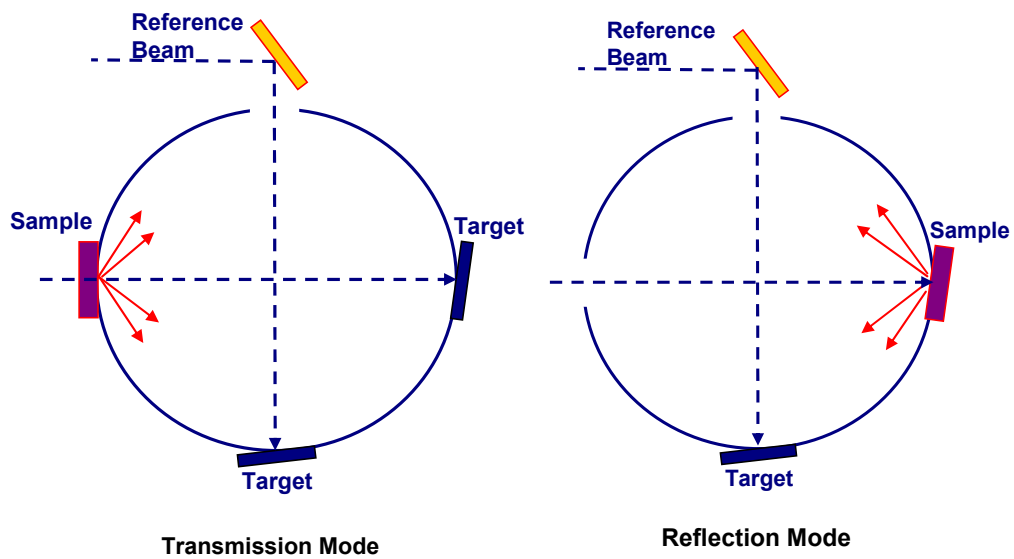


**Figure 3.9 Integrating sphere configuration and the sample position in transmission and reflection modes [114]**

Once the transmittance and reflectance are measured, the value of absorption percentage, which is the percentage of the incident beam that is neither reflected nor transmitted, can be calculated.

### **3.7.2 High-temperature optical absorption**

The absorbance of the thin films was measured in a temperature range of 25–300 °C in order to investigate the effect of temperature on the optical absorption properties of the films. A U-3010 UV-Vis spectrometer provided by



Hitachi and equipped with a hot chamber and a Mettler FP 80 central processor was used for this type of measurement. The absorbance spectra of the samples were obtained for temperature intervals of 10 °C in a wavelength range of 200 – 900 nm. Figure 3.10 shows the setup used for this type of measurement.

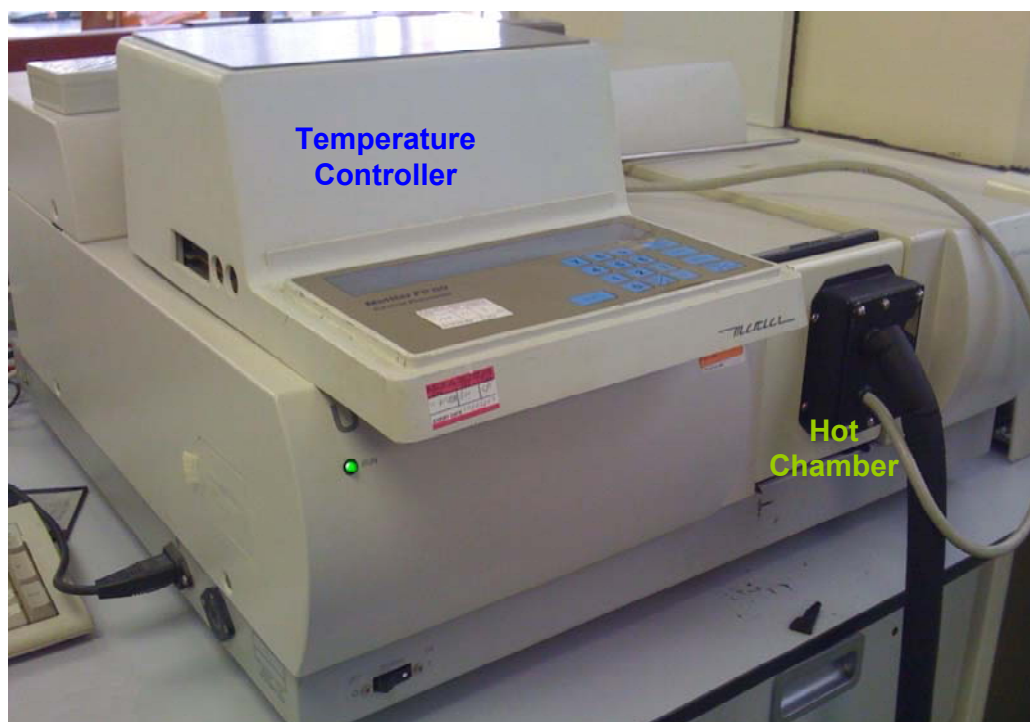


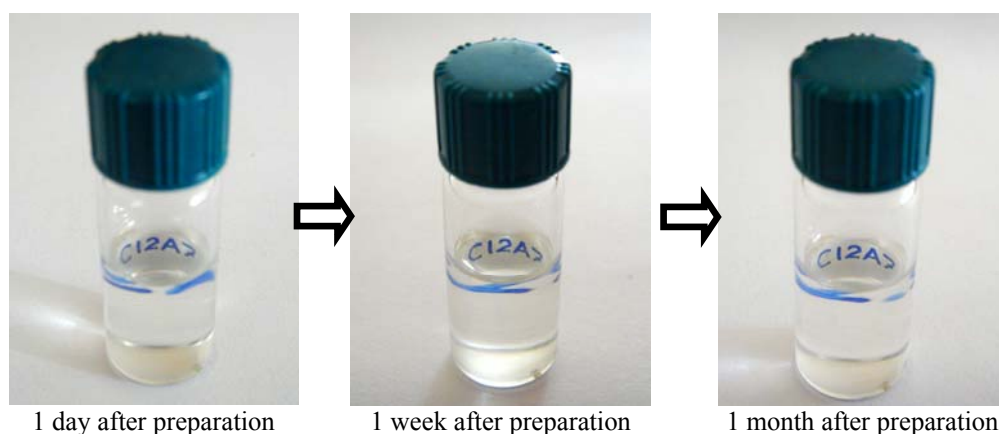
**Figure 3.10 High-temperature UV-Vis spectrometry setup**

# Chapter 4

## Microstructure and chemical composition

### 4.1 Chemical stability of the solution

The transparency of a solution over time is shown in figure 4.1. The molar ratios of the ingredients used for the preparation of this solution are also given.



<i>Solution ingredient</i>	<i>EAA to ASB</i>	<i>Solvent to ASB</i>	<i>Solvent to Ca(NO<sub>3</sub>)<sub>2</sub></i>	<i>H<sub>2</sub>O to ASB</i>
<i>Molar ratio</i>	2:1	10:1	10:1	5:1

**Figure 4.1** Transparency of the prepared solution versus time, the solution ingredients and the molar ratios used for solution preparation.

As is clear from the figure, the transparency of the solution was preserved for at least one month after the preparation. No special routine, such as addition of acid, sonicating or continuous stirring, was required in order to maintain the chemical stability of the solution. Similar results were obtained for solutions prepared with different amounts of ethyl acetoacetate, water or solvent, and only the quality of the films (after complete gelation) was affected by different amounts of ingredients. All the variables considered in the solution recipe are given in section 3.1.

## **4.2 Thin film surface microstructure**

The microstructures of the spin-coated thin films on MgO substrates were observed by scanning electron microscopy. Figure 4.2 shows the microstructure of the thin films prepared with two different methanol-to-ASB molar ratios of 40:1 and 20:1 and water-to-ASB molar ratio of 20:1. The solvent-to- $\text{Ca}(\text{NO}_3)_2$  molar ratios used for all solution recipes were the same as solvent-to-ASB ratios.

As shown in figure 4.2(a), the thin film prepared with a molar ratio of 40:1 for methanol-to-ASB forms islands on the surface of the substrate and the film is discontinuous.

The discontinuity of the film might be attributed to the high molar fractions of the solvent and water in the solution. If the amount of solvent and water added to the solution is more than the required amount for sol stabilization and hydrolysis, the excess solvent and water dilute the solution and reduce the amount of main precursors.

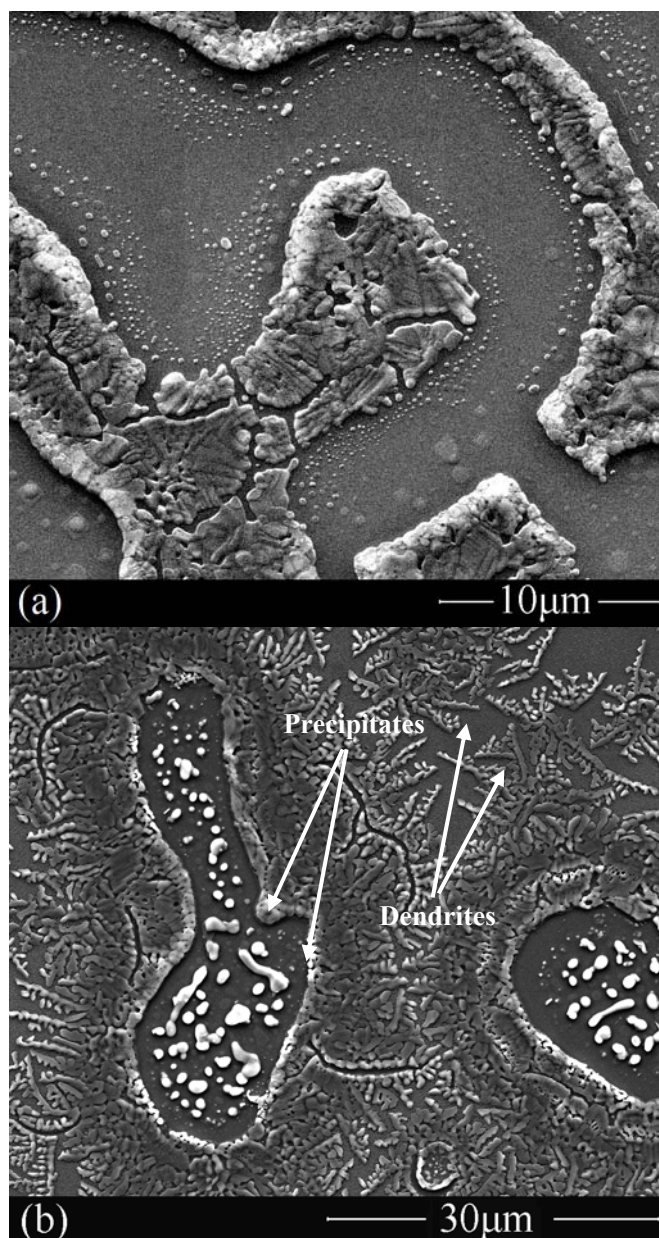


**Figure 4.2** Microstructures of the thin films prepared with methanol-to-ASB molar ratios of (a) 40:1 and (b) 20:1. The molar ratios of 3:1 for EAA-to-ASB and 20:1 for water-to-ASB were used for both solutions. The films were heat treated at 1300 °C for 2 hr in air atmosphere.

The dried gel goes through several phase transformations and chemical reactions during the heat treatment, such as the evaporation of water and solvent, dehydration and decomposition of the ingredients and oxidation of the chelating agent. A diluted solution does not contain sufficient ingredients needed for the formation of a continuous crystalline film. As a result, the



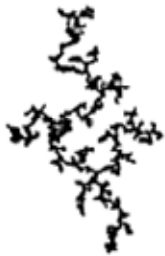
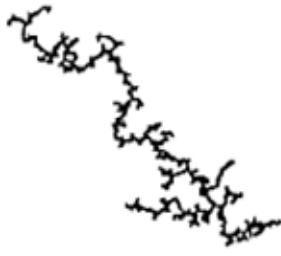
thickness of the film is significantly reduced and separate islands of crystals are formed on the substrate instead of a continuous film [115].

The microstructure of a film prepared from the solution with solvent-to-ASB molar ratio of 20:1 is shown in figure 4.2(b). There are some clear differences observed between the microstructures of the two samples. The decrease in the amount of added solvent, i.e. an increase in the molar fractions of the main ingredients, results in a higher surface area of the substrate to be covered by the crystallized material. However, a continuous film is still not formed. Furthermore, a dendritic structure is observed. Dendritic crystal growth is a type of non-equilibrium pattern formation which is caused by the shape instability during the diffusion of chemical constituents toward and away from the crystal front and results in the formation of small bumps. These bumps concentrate the diffusive fluxes ahead of them and grow faster than a flat surface and form into fingers, also known as dendrites [116].

The heat treatment of a gel at high temperatures results in the chemical evolution of the gel as well as the crystallographic reorganization of the solid network. The heat treatment at intermediate temperatures (typically 100 to 1000 °C) produces a crystalline metastable phase which eventually transforms to the most stable phase at higher temperatures. The formation of stable thermodynamic phases from the intermediate phases often occurs via nucleation and growth mechanism, while the formation of metastable phases at intermediate temperatures is less likely to occur through nucleation and growth. The nucleation of a new phase involves the diffusion of both cations and anions, and anions such as oxygen require high activation energy for diffusion due to their big size. Therefore, new crystalline phases which are formed at

intermediate temperatures maintain the same crystallographic orientation as the initial phases in the original gel [117].

Several aggregation models have been proposed in order to explain the formation of dendrites and the mechanisms responsible for the dendrites to appear in different shapes. A schematic illustration of different types of dendritic growth is shown in figure 4.3.

	<b>Reaction -limited</b>	<b>Diffusion -limited</b>
<b>Monomer-Cluster</b>		
<b>Cluster-Cluster</b>		

**Figure 4.3 Schematic illustration of different types of aggregation growth [118]**

In monomer-cluster aggregation growth, the monomers get separated randomly far from a central cluster and travel by diffusion mechanism joining the growing cluster. In a diffusion-limited aggregation of this type, the monomers cannot penetrate deep into the cluster and the depth of penetration is effectively controlled by the arms of the growing cluster. Therefore, the growth occurs preferentially at the exterior sites and the density of the cluster decreases

radially from the centre of the mass. In a reaction-limited aggregation, however, there is a barrier to bond formation between a monomer and the cluster which reduces the condensation rate. This means that not all the collisions between a monomer and a cluster will result in the formation of a bond between them. The unoccupied sites are selected randomly and occupied with equal probability, and compact, smooth clusters are formed as a result.

In cluster-cluster aggregation growth, on the other hand, a sea of monomers with random movements join and form a collection of clusters that grow by condensation reactions with each other and other monomers. The result of this type of growth is the formation of very open structures with no obvious centres [118].

A comparison between the microstructure of the sample (figure 4.2(b)) with the aggregation models (figure 4.3) shows that dendrites are mostly formed via monomer-cluster aggregations. Furthermore, precipitates and cracks seem to be the preferential sites for the nucleation of the monomers which grow into dendrites as the heat treatment continues [119]. In order to verify this observation, the microstructures of the films were obtained before and after heat treatment, as shown in figure 4.4.

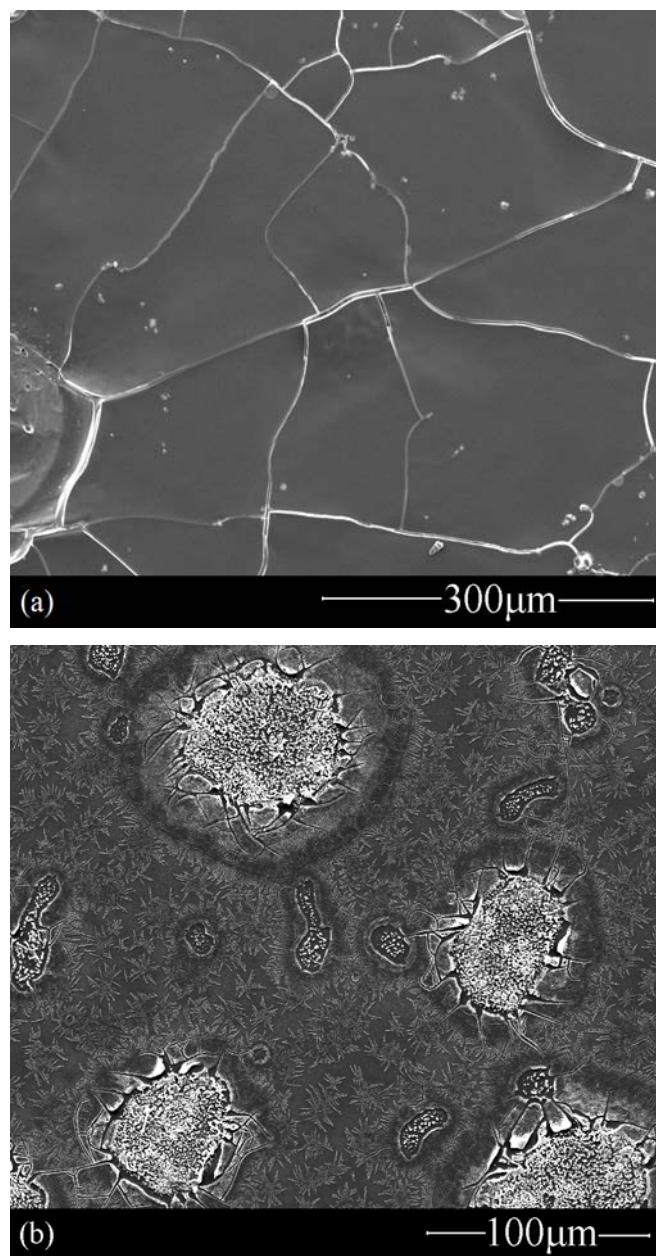


**Figure 4.4** Microstructure of the thin film (a) before and (b) after heat treatment at 1300 °C for 2 hr. The molar ratios of 20:1 for methanol-to-ASB, 3:1 for EAA-to-ASB, and 20:1 for water-to-ASB ratios were chosen for the preparation of the solution.

The microstructure of the dried gel in the as-prepared state clearly shows the presence of cracks, while the precipitates seem to be formed during the heat treatment of the film. The formation of cracks can be attributed to the presence of network structures in the solution and the cohesive force within the film being stronger than the adhesive force at the interface between the film and the



substrate. The reason for this behaviour is that the OH groups in the film, which are necessary for the adhesion to the substrate, are reduced considerably via hydrolysis and condensation [120]. The presence of cracks at this point can further develop the discontinuity of the film during the heat treatment as a large amount of the remaining ingredients are removed through evaporation and decomposition. In order to prevent or minimize the formation of cracks, the tensile stress of the film needs to be reduced. Organic modification of alkoxides, application of chelating agents in the solution, and low degree of alkoxide hydrolysis are some of the possible methods suggested for the structural relaxation and hence the prevention of cracks from appearing during the drying and heat treatment processes [81].

The formation of precipitates, on the other hand, might be due to the removal of the remaining chelating agent and the precipitation of aluminium alkoxide. Since the amount of water is the main factor in controlling the hydrolysis of the alkoxide, a decrease in the molar fraction of water in the solution might prevent the localised precipitation. On the other hand, a decrease in the amount of solvent with respect to the main ingredients, aluminium sec-butoxide and calcium nitrate, from which calcium aluminate compound is formed, might improve the continuity of the film.

During the first step of the modification based on these observations, water-to-ASB molar ratio was reduced while keeping methanol-to-ASB ratio constant (20:1). The EAA-to-ASB molar ratio of 3:1 was found to have no significant advantage over the molar ratio of 2:1 in terms of improving the quality of the films. Therefore, this molar ratio was fixed to a practical ratio of 2:1 mentioned

in the literature [77]. Figure 4.5 shows the microstructure of a heat treated film which was prepared using the new solution recipe.

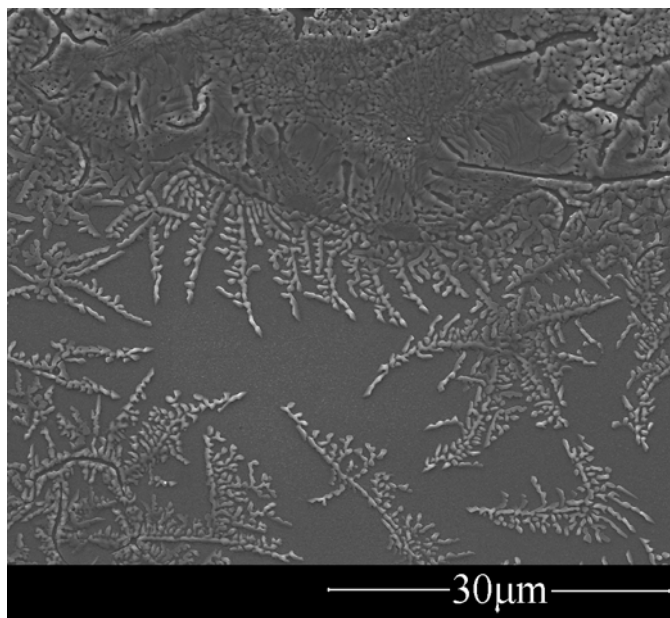


**Figure 4.5** Microstructure of the thin film with a water-to-ASB molar ratio of 5:1 and methanol-ASB ratio of 20:1. The film was heat treated at 1300 °C for 2 hr in air atmosphere.

Although the precipitates are absent from the structure, the film remains discontinuous with dendrites developing on the surface of the substrate. It seems that reducing the amount of water from 20:1 to 5:1 improves the uniformity of the film by increasing the homogeneity of the solution and preventing the undesirable precipitation of the products during the heat treatment. However, the water-to-ASB molar ratio of 5:1 does not seem to improve the continuity of the films.

In order to investigate the effect of solvent on the quality of the films, the molar ratio of methanol to ASB was reduced to 5:1 while keeping the water-to-ASB ratio at 5:1. The microstructure of the obtained thin film after the crystallization treatment is shown in figure 4.6.

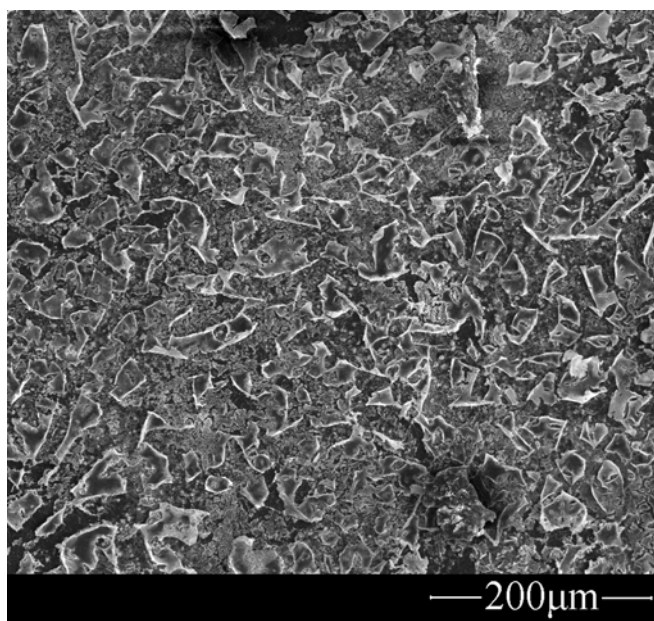


**Figure 4.6** Microstructure of the thin film prepared with a solution containing a molar ratio of 5:1 for methanol-to-ASB and water-to-ASB. The film was heat treated at 1300 °C for 2 hr in air atmosphere.

The result of the microstructural observation shows that decreasing the molar ratio of methanol to ASB from 20:1 to 5:1 leads to a formation of a continuous film. The uniformity of the film, however, is drastically deteriorated. The film is scaled with a loss of transparency, probably due to a high concentration of the ingredients. It was concluded that the molar ratio of solvent to ASB should lie in between 20:1 and 5:1.

In another attempt to improve the uniformity and continuity of the film, isopropyl alcohol was used as an alternative to methanol which has been reported to be a good mutual solvent for aluminium sec-butoxide and calcium nitrate [68]. The microstructure of the film using isopropyl alcohol as the solvent with a solvent-to-ASB molar ratio of 10:1 is shown in figure 4.7.

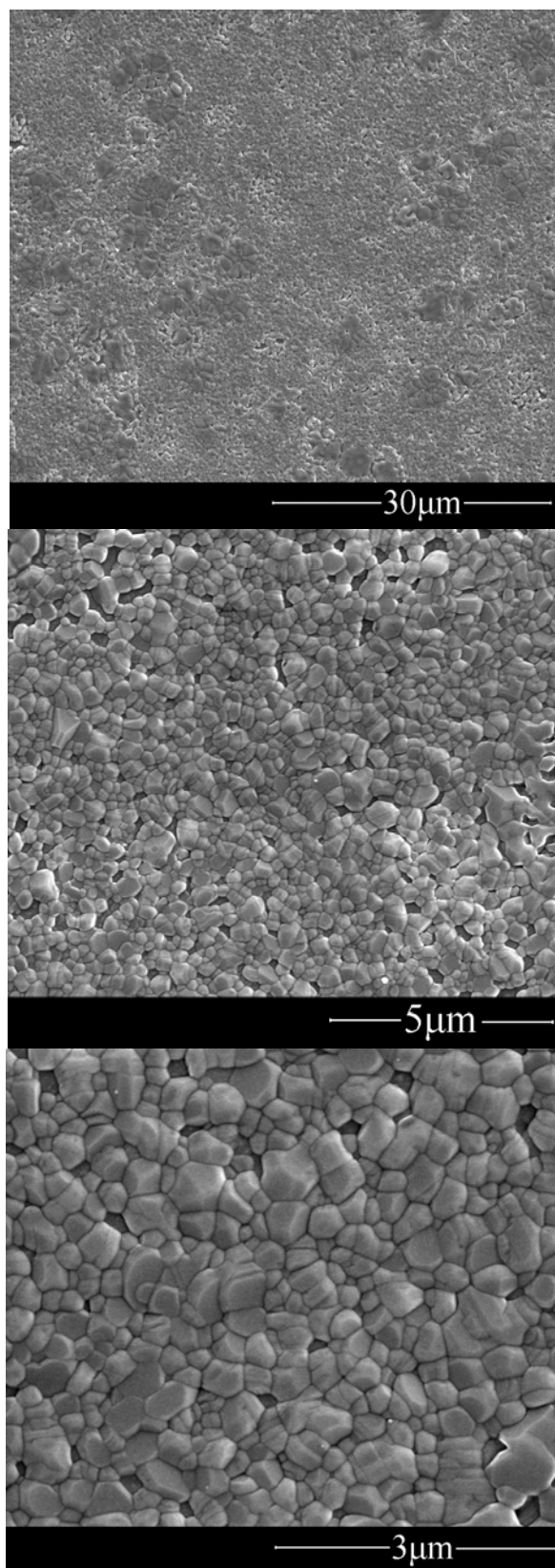


**Figure 4.7** Microstructure of the thin film prepared with a solution containing isopropyl alcohol as the solvent. The molar ratio of 10:1 and 5:1 were chosen for isopropyl alcohol-to-ASB and water-to-ASB respectively. The film was heat treated at 1300 °C for 2 hr in air atmosphere. The figures were taken from the same sample with different magnifications.

At a high enough temperature, the transformation of the intermediate phases progresses towards the most stable thermodynamic phase via nucleation and growth mechanism, the temperature of which depends on the type of ceramic as well as the sol-gel process selected. The transformation to the most stable phase often involves a significant change in the anion packing. When the temperature is high enough for the anions to diffuse and reorganize, the grains of the stable phase grow quickly at the expense of the small crystallites of the previous metastable phase [117]. As can be seen from the above figures, the quality of the film is significantly improved by using a proper amount of isopropyl alcohol as the solvent. This can be attributed to the better solubility of aluminium sec-butoxide in an alcohol with a chemical composition close to the one of the parent alcohol (butyl alcohol) [117]. The surface continuity of the film is preserved even after the heat treatment and no cracks or scales are observed. A completely crystallized structure is formed with well-defined grain boundaries and no trace of dendrite structure. Therefore, the solution recipe containing isopropyl alcohol is chosen as the proper solution for the fabrication of uniform continuous films. The details of the ingredients used in the preparation of this solution are listed in table 4.1.

The thickness of the films prepared by the optimum solution recipe was determined to be a few microns ( $6.5\ \mu\text{m}$  for a thin film spin coated at a spinning rate of 1000 rpm) which is considerably higher than the critical thicknesses generally reported for sol-gel derived thin films [3, 71].

**Table 4.1 Molar ratios and the total weight for the improved solution recipe**

<i>Solution ingredient</i>	<i>Molar ratio with respect to ASB</i>	<i>Molar ratio with respect to Ca(NO<sub>3</sub>)<sub>2</sub></i>	<i>Total weight (g)</i>
Aluminium sec-butoxide (ASB)	-	1.67: 1	4
Ca(NO <sub>3</sub> ) <sub>2</sub>	1:1.67	-	3.3
Ethyl acetoacetate (EAA)	2:1	-	4.24
Water	5:1	-	1.46
Isopropyl alcohol	10:1	10:1	18

### 4.3 Chemical analysis of the thin films and powder

#### 4.3.1 Energy dispersive spectroscopy

The energy dispersive spectrum of a crystalline thin film is shown in figure 4.8. The weight percent of the identified elements are given in table 4.2.

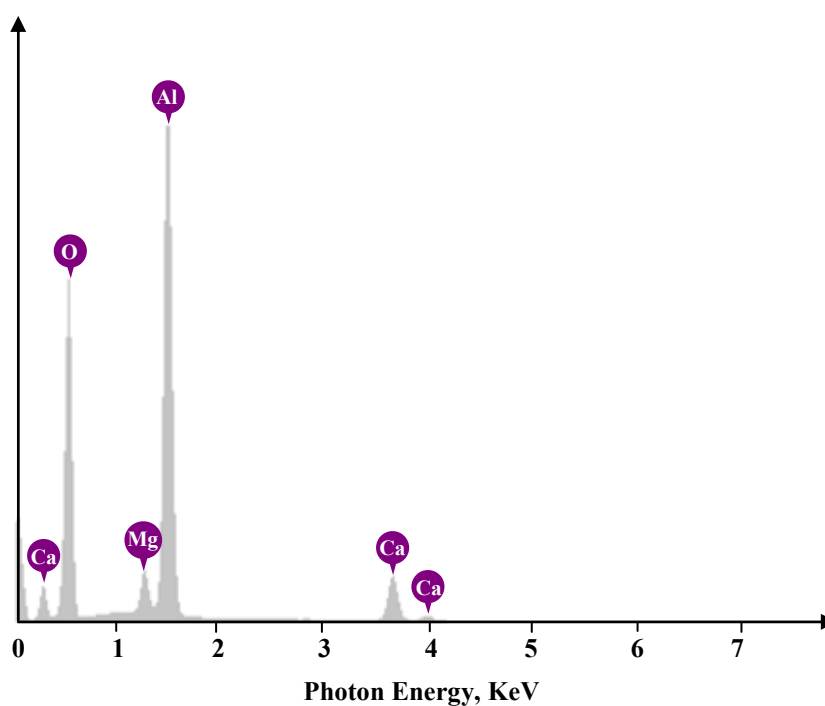


**Figure 4.8 Energy dispersive spectrum of C12A7 thin film**

**Table 4.2 Weight percent of the elements in the thin film identified by energy dispersive spectroscopy**

<i>Element</i>	<i>O</i>	<i>Mg</i>	<i>Al</i>	<i>Ca</i>
<i>Weight percent, wt%</i>	41.46	49.23	4.36	4.95

According to the above spectrum, the film mainly consists of aluminium, calcium and oxygen. The presence of magnesium is attributed to the signal obtained from the MgO substrate. The aluminium-to-calcium weight ratio at 0.88 is comparable to the theoretical value of 0.785 for C12A7.

#### **4.3.2 X-ray photoelectron spectroscopy**

The X-ray photoelectron spectra of the dried gel and the crystallized film are shown in figures 4.9 and 4.10. The results were obtained for the samples before and after heat treatment in order to determine the phases present in the dried gel and the final material.

A comparison between the results obtained from this experiment and the binding energies reported in the literature is presented in table 4.3.

The results of the analysis show that aluminium hydroxide ( $\text{Al}(\text{OH})_3$ ) is formed in the dried film before the annealing treatment is carried out. The presence of aluminium hydroxide is expected as the product of aluminium sec-butoxide hydrolysis. The peak at 289.46 eV belongs to the O-C=O bond of ethyl acetate ( $\text{MeCOOEt}$ ), which is formed as a result of aluminium sec-butoxide chelation with ethyl acetoacetate and remains bonded to aluminium after exposure to air.

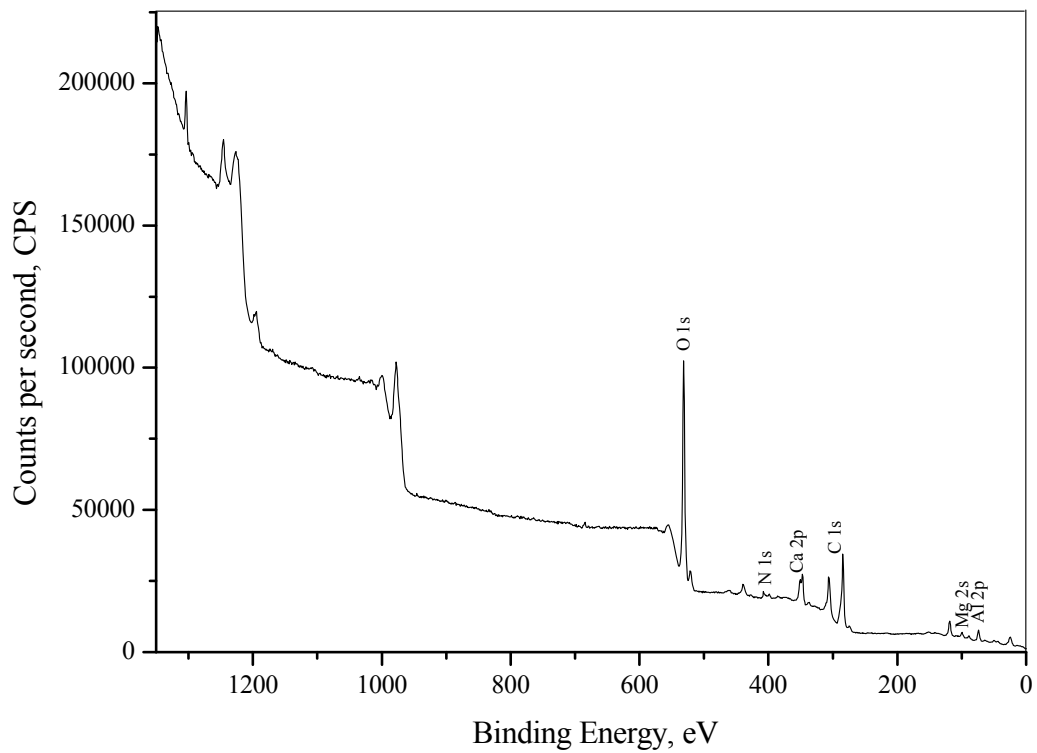


**Figure 4.9 X-ray photoelectron spectrum of the thin film before heat treatment**

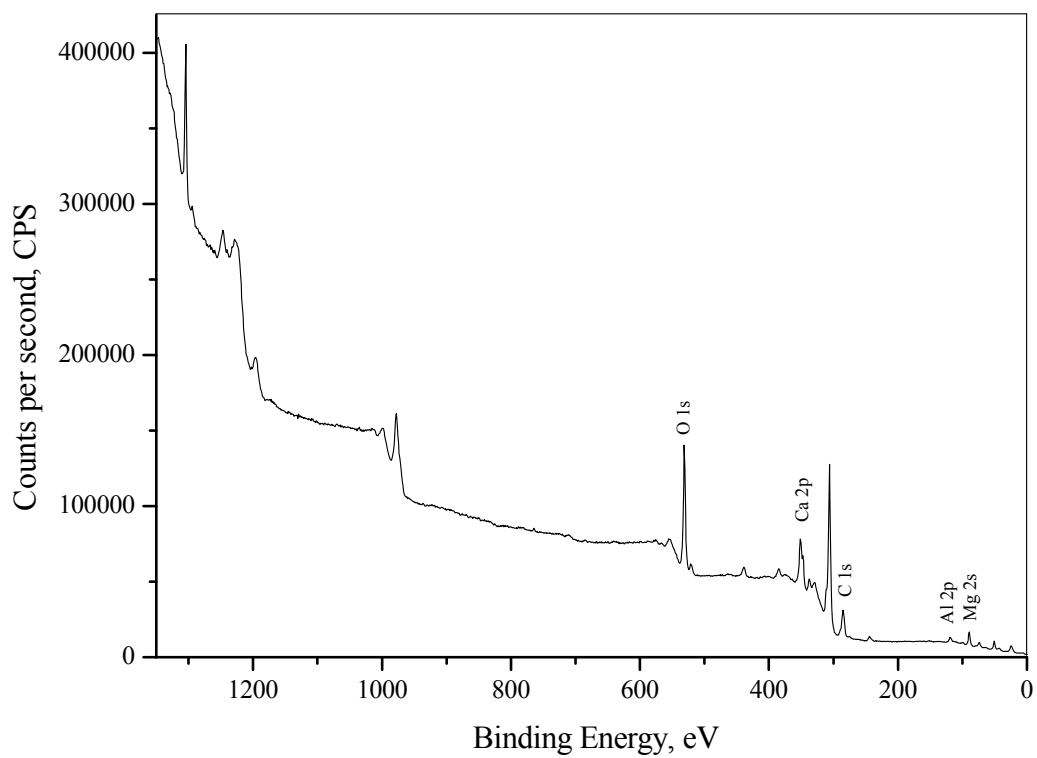


**Figure 4.10 X-ray photoelectron spectrum of the thin film after a heat treatment at 1300 °C for 2 hr in air atmosphere**



**Table 4.3 Binding energy peaks and the phases formed in the film before and after heat treatment**

<i>Sample treatment</i>	<i>Element</i>	<i>XPS peaks</i>		<i>Phase</i>
		<i>Experiment</i>	<i>Reference</i>	
<i>Before annealing</i>	Al 2p	73.5	73.9 [121]	Al(OH) <sub>3</sub>
	Ca 2p	347.5	348.2 [122]	Ca(NO <sub>3</sub> ) <sub>2</sub>
	N 1s	407.5	407.4 [122]	
	C 1s	289.46	289.2 [123]	MeCOOEt
	Mg2p	50.4	50.2 [124]	MgO
<i>After annealing</i>	Al 2p	74.381	74.5 [125]	12CaO.7Al <sub>2</sub> O <sub>3</sub>
	Ca 2p	347.0	347.2 [125]	
	O 1s	531.4	531.5 [125]	
	Mg 2p	50.7	50.5-50.8 [126]	MgO

The XPS spectrum of the thin film after annealing treatment corresponds to the binding energies of C12A7 compound. The peak related to O-C=O bond has completely disappeared which shows the decomposition of the chelating agent during the heat treatment (as previously mentioned in section 2.6.6). No separate peak was observed for the extra-framework oxygen site probably due to the binding energies of the O<sup>2-</sup> 1s level being too close to that of the lattice and/or the concentration of these species being too small compared to the ones of the framework oxygen ions [11].

#### **4.3.3 Room-temperature powder X-ray diffraction analysis**

The effect of heat treatment temperature on the formation of C12A7 powder from the dried gel was investigated in a temperature range between 700 to 1300 °C using powder X-ray diffraction technique.

The X-ray diffraction pattern of the dried gel after a heat treatment at 700 °C for 15 hr is depicted in figure 4.11.

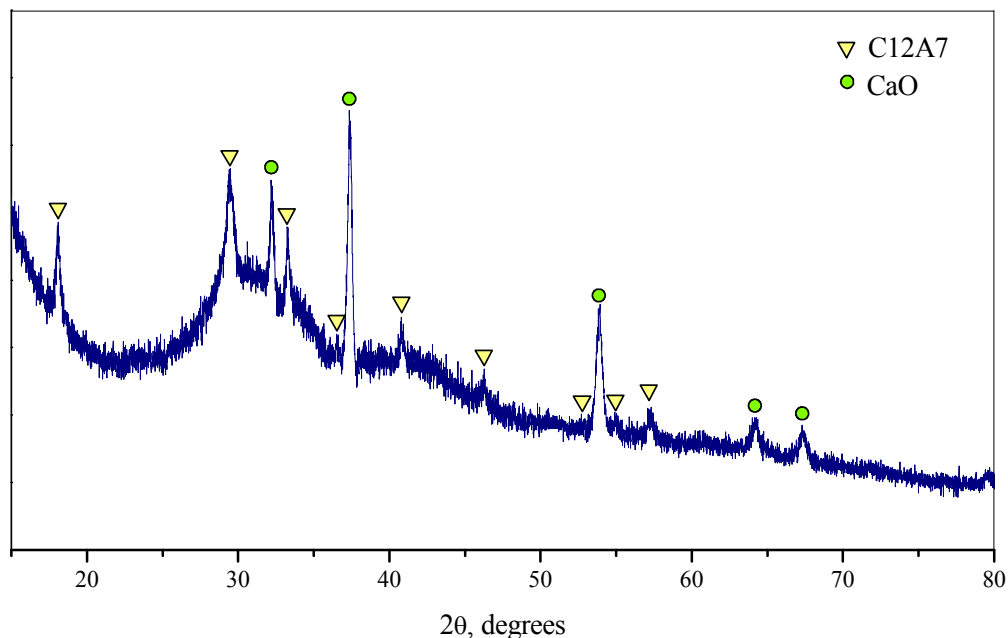


**Figure 4.11 X-ray diffraction pattern of the dried gel after a heat treatment at 700 °C for 15 hr**

The result of the XRD analysis shows that the powder mainly contains crystallized C12A7 and CaO, while some of the powder remains in the amorphous state even after a long heat treatment duration of 15 hr. It seems that the temperature of 700 °C is high enough for the C12A7 phase to start forming. However, a complete transformation from the dried gel to a crystallized phase is unlikely to occur in a reasonable heat treatment duration. It has been mentioned earlier (section 2.6.6) that the conversion of calcium nitrate to calcium oxide starts at ~ 500 °C followed by the crystallization of the oxide [68]. Therefore, the presence of crystalline CaO is expected at this temperature. No free aluminium oxide phase is observed which shows that the oxide formed at the initial stage of the heat treatment is completely converted to C12A7. Since

calcium aluminate compounds are thermodynamically more stable at higher temperatures, it is reasonable to expect that an increase in the heat treatment temperature will result in the complete crystallization of the powder and formation of calcium aluminate compounds instead of CaO. Figure 4.12 shows the X-ray diffraction pattern of the dried gel after a heat treatment at 1100 °C for 6 hr.

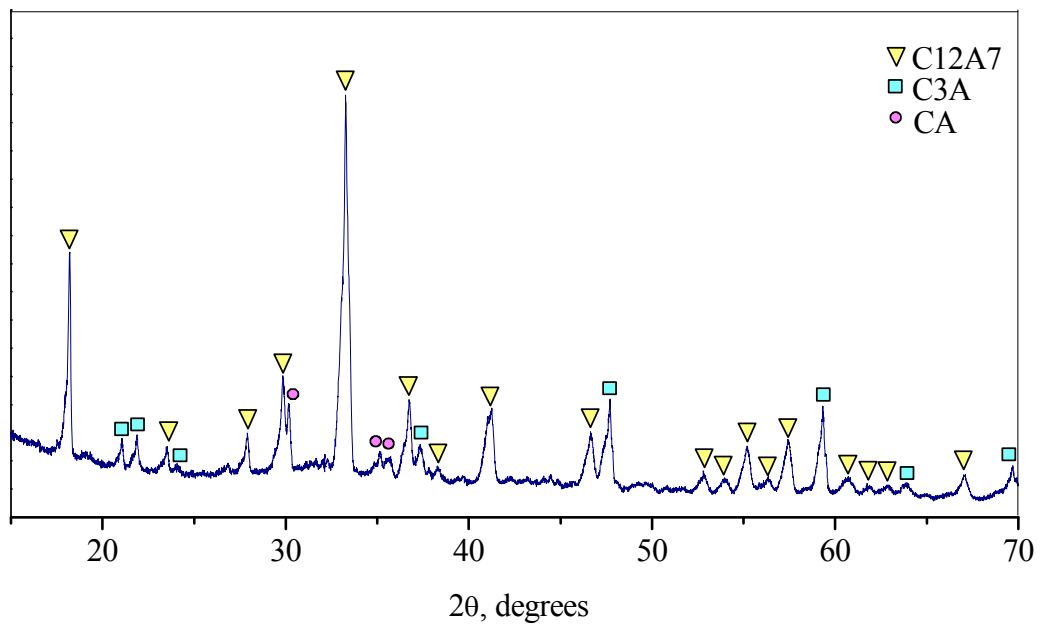


**Figure 4.12 X-ray diffraction pattern of the dried gel after a heat treatment at 1100 °C for 6 hr**

Increasing the heat treatment temperature to 1100 °C resulted in a significant change in the X-ray diffraction pattern of the product. A major increase in the intensity of the C12A7 diffraction peaks shows that increasing the heat treatment temperature is in favour of C12A7 formation. The disappearance of CaO and the formation of secondary phases, CA and C3A, further confirm the formation of crystallized calcium aluminate phases instead of free calcium oxide and aluminium oxide. The crystal structures of these two calcium aluminate compounds are introduced in section 2.1.1.

The X-ray diffraction pattern of the dried gel after a heat treatment at 1300 °C for 6 hr is depicted in figure 4.13.

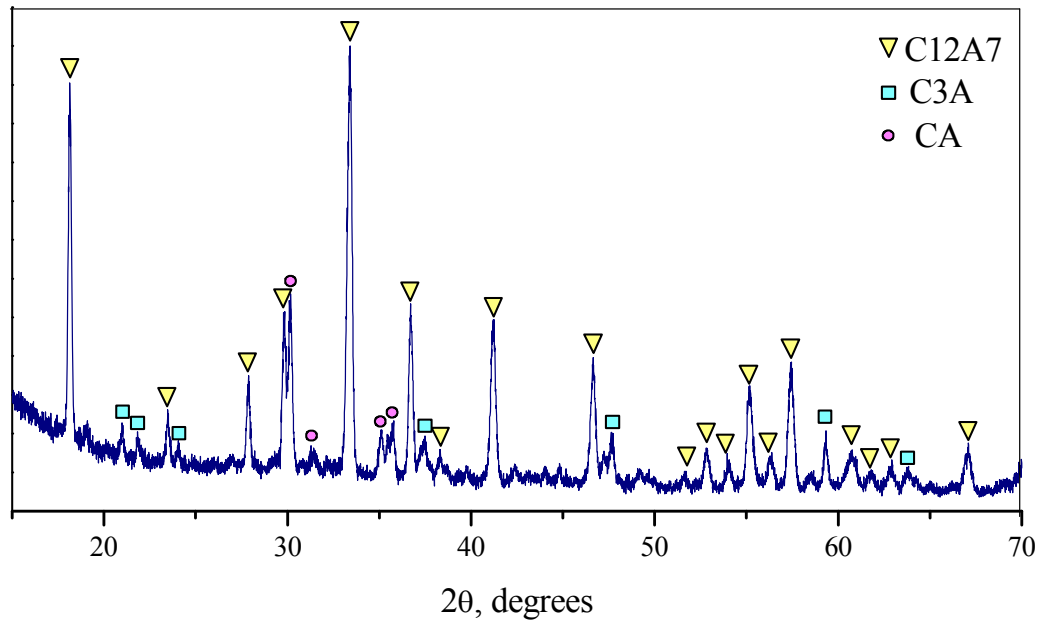


**Figure 4.13 X-ray diffraction pattern of the dried gel after a heat treatment at 1300 °C for 6 hr**

The results of the analysis showed the formation of C12A7 along with CA and C3A. Although the X-ray diffraction patterns after two different heat treatments seem to be quite similar, there are some differences observed. A comparison between the two graphs is shown in figure 4.14.

As can be seen from the figure, an increase in the heat treatment temperature from 1100 to 1300 °C resulted in the preferable formation of C12A7 and CA compared to C3A.

According to previous investigations [127], C12A7 is the first product of the diffusion and crystallization. As the temperature is increased, further diffusion of anions and cations results in the formation of CA. When all the free alumina is converted into CA, C3A begins to form.

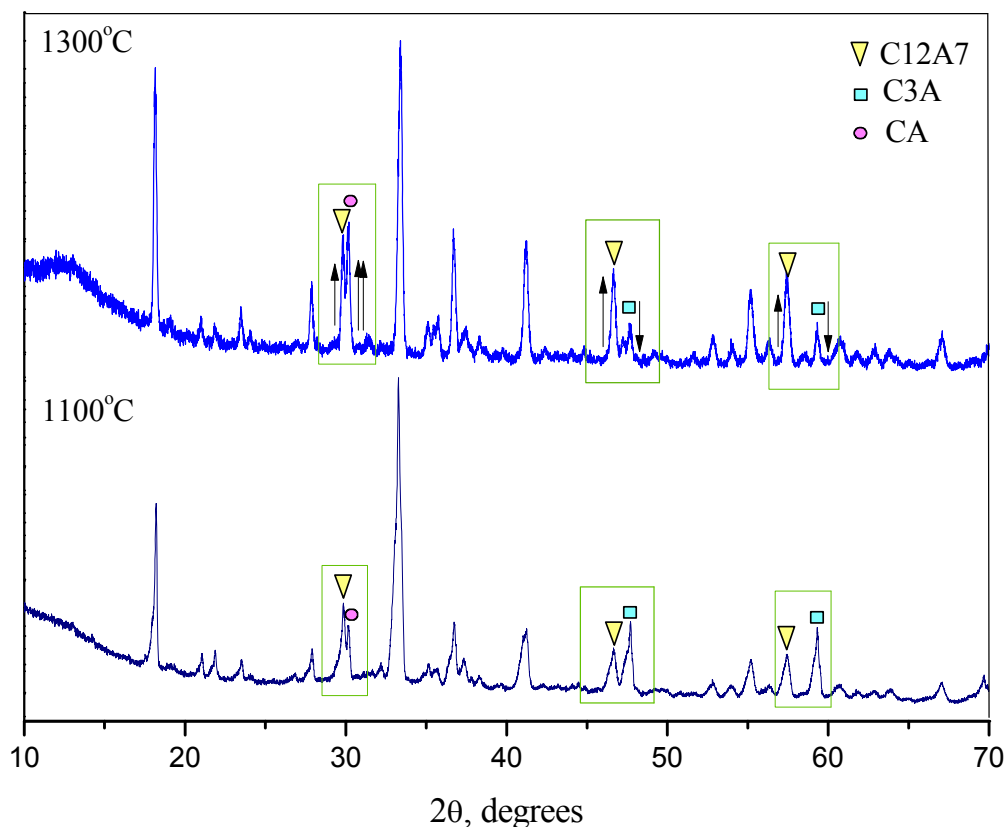


**Figure 4.14 Comparison between the X-ray diffraction patterns of the dried gel after heat treatment at 1100 and 1300 °C**

The conversion into stoichiometric phases continues until all free CaO and Al<sub>2</sub>O<sub>3</sub> are consumed, at which point C12A7 is formed at the expense of CA and C3A (figures 4.13 and 4.14). A complete transformation of CA and C3A to C12A7 requires a heat treatment at a temperature of 1350 °C or higher for at least 48 hr, and even after long-term treatments, the product might still contain secondary phases due to agglomeration, irregularity of the powder and poor sinterability [128].

Table 4.4 shows the d-spacings calculated from the X-ray diffraction pattern of the powder after a heat treatment at 1300 °C in comparison with the ones reported in the literature. The lattice indices have also been determined.

**Table 4.4 D-spacings and the lattice indices of the dominant reflections of C12A7 [129] for the dried gel after a heat treatment at 1300 °C for 6 hr. The angles marked with \* and \*\* belong to the diffraction peaks of CA [130] and C3A [131] phases respectively.**

<i>2θ (degrees)</i>		<i>d (Å)</i>		<i>Indices</i>		
<i>Observed</i>	<i>Reference</i>	<i>Observed</i>	<i>Reference</i>	<i>h</i>	<i>k</i>	<i>l</i>
18.023	18.052	4.916	4.910	2	1	1
18.996*	19.012	4.666	4.664	-1	1	2
20.867	20.935	4.254	4.240	2	2	0
21.720**	21.749	4.087	4.083	2	3	0
23.352	23.391	3.805	3.800	3	1	0
27.764	27.769	3.209	3.210	3	2	1
29.727	29.726	3.001	3.003	4	0	0
30.057*	30.085	2.969	2.968	2	2	0
31.378*	31.350	2.847	2.851	-3	0	1
33.286	33.280	2.689	2.690	4	2	0
35.019	34.967	2.559	2.564	3	2	2
36.578	36.588	2.454	2.454	4	2	2
37.367*	37.468	2.404	2.398	3	1	3
38.211	38.117	2.352	2.359	4	3	1
41.128	41.069	2.192	2.196	5	2	1
46.530	46.485	1.949	1.952	6	1	1
47.612**	47.596	1.908	1.909	8	0	0
49.144	49.071	1.852	1.855	5	4	1
52.758	52.650	1.733	1.737	4	4	4
53.840	53.819	1.701	1.702	7	1	0
55.069	54.972	1.666	1.669	6	4	0
56.261	56.103	1.633	1.638	7	2	1
57.325	57.168	1.605	1.610	6	4	2
59.215**	59.223	1.559	1.559	8	4	4
60.655	60.503	1.525	1.529	5	6	1
61.737	61.526	1.505	1.506	8	0	0
62.755	62.634	1.479	1.482	7	4	1
66.983	66.817	1.395	1.399	8	3	1
69.909	69.820	1.344	1.346	8	4	2

The mean crystallite size and the microstrain of the lattice can be determined by relating these parameters to the width of the diffraction peaks.

A careful observation of the diffraction patterns of the material shows that the diffraction peaks are broad in width. The broadening of the diffraction peaks can be related to a number of reasons including the nature of the crystal and the instrumental factors. For instance, the size of the crystallites and the lattice strain due to the presence of defects can lead to diffraction peak broadening. Scherrer has proposed a simple relationship between the crystallite size and the broadening of the diffraction peaks as follows [132]:

$$\beta_{\text{size}} = \frac{K\lambda}{L \cos \theta} \quad (4.1)$$

where  $K$  is the shape factor with a value close to unity,  $\lambda$  is the X-ray wavelength (0.154 nm for Cu  $K\alpha$ ),  $\theta$  is the Bragg angle and  $\beta_{\text{size}}$  is the full width at half maximum (FWHM) intensity of the diffraction peaks in radians due to size effects. A rather simple formula is also suggested by Stokes and Wilson, which accounts for the effect of lattice microstrain on the broadening of the diffraction peaks [133]:

$$\beta_{\text{strain}} = \eta \tan \theta \quad (4.2)$$

where  $\eta$  is the lattice microstrain,  $\theta$  is the Bragg angle and  $\beta_{\text{strain}}$  is the full width at half maximum intensity due to strain effects.

It is often possible to express the total peak broadening as the sum of size broadening and strain broadening as suggested by Williamson and Hall [134]:

$$\beta = \beta_{\text{size}} + \beta_{\text{strain}} = \frac{K\lambda}{L \cos \theta} + \eta \tan \theta \quad (4.3)$$

Multiplying the above expression by  $\cos \theta$  gives the following relation:

$$\beta \cos \theta = \frac{K\lambda}{L} + \eta \sin \theta \quad (4.4)$$

The plot of  $\beta \cos \theta$  versus  $\sin \theta$ , also known as the Williamson-Hall plot, gives a straight line in which the lattice microstrain is the slope and the mean crystallite size can be determined from the intercept of the line. Figure 4.15 shows the Williamson-Hall plot for C12A7 after a heat treatment at 1300 °C for 6 hr.

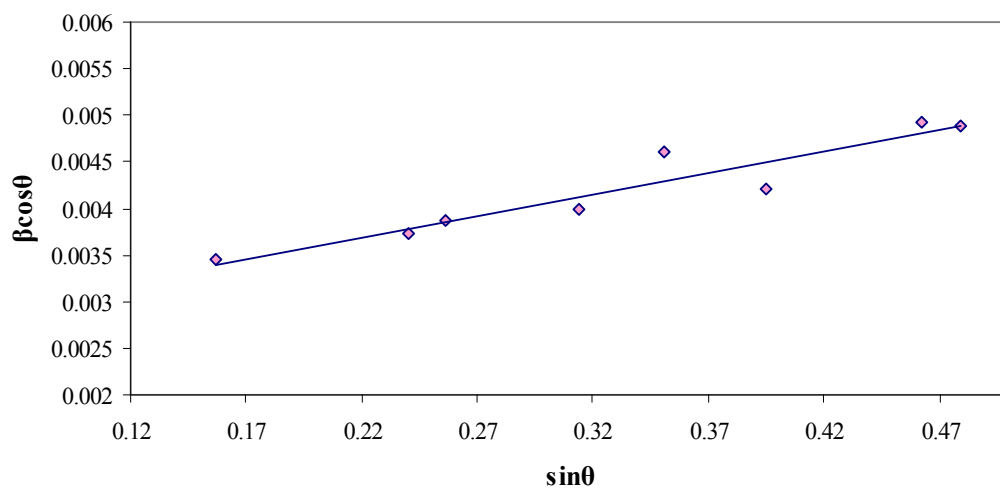


**Figure 4.15 Williamson-Hall plot for C12A7 powder. The data was obtained from the diffraction peaks of the compound after a heat treatment at 1300 °C for 6 hr.**

The values of mean crystallite size and lattice microstrain were obtained from the plot to be 57 nm and 0.47 % respectively. The crystallite size and the lattice microstrain were determined for C12A7 compound after heat treatment durations of 3, 4 and 6hr at 1100 °C. The variations of these parameters with heat treatment time are depicted in figure 4.16.



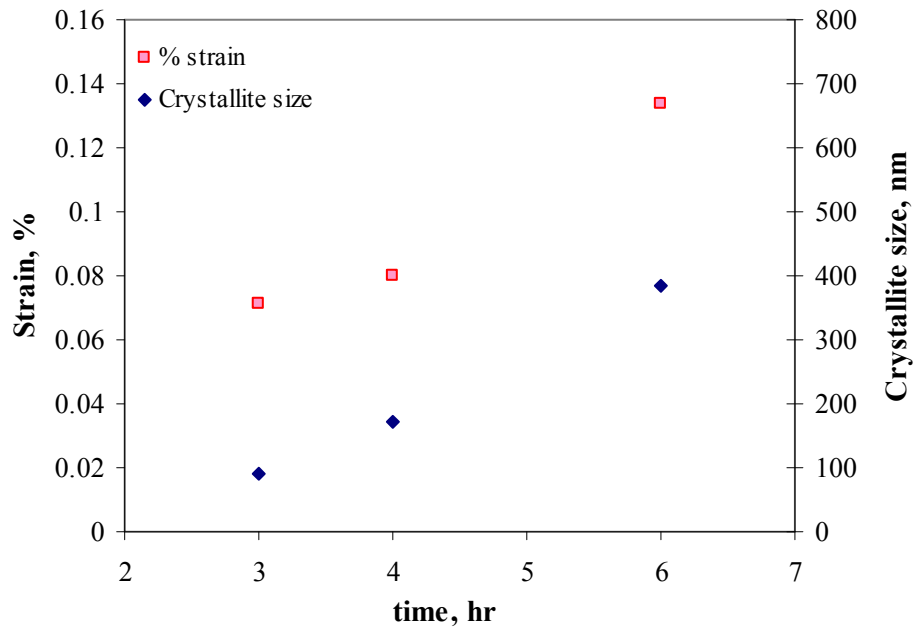


**Figure 4.16 Effect of heat treatment time on the crystallite size and lattice strain of C12A7 for a heat treatment temperature of 1100 °C**

As can be seen from the plots, the crystallite size and the lattice strain have increased with the increase in heat treatment duration at 1100 °C and slow cooling to room temperature. It seems that crystal growth is a more dominant mechanism compared to nucleation at this temperature, probably because the diffusion is facilitated, leading to an increase in the size of the crystallites. The increase in the lattice strain of C12A7 might be attributed to the presence of secondary phases, such as CA and C3A, which crystallize along with C12A7 and are thermodynamically more stable than C12A7 at the temperature of 1100 °C. At higher temperatures (1300 °C and more), C12A7 becomes the most stable compound and C12A7 is crystallized at the expense of CA and C3A [127]. Therefore, a different behaviour in terms of lattice strain might be expected at higher temperatures and this result is simply limited to the heat treatment temperature of 1100 °C.

#### 4.3.4 High-temperature powder X-ray diffraction analysis

In order to investigate the crystallization phenomenon of C12A7 and other possible calcium aluminate phases with the increase in the temperature, the X-ray diffraction patterns of the dried gel were obtained at high temperatures in the range of 700 to 1200 °C. These patterns are depicted in figure 4.17.

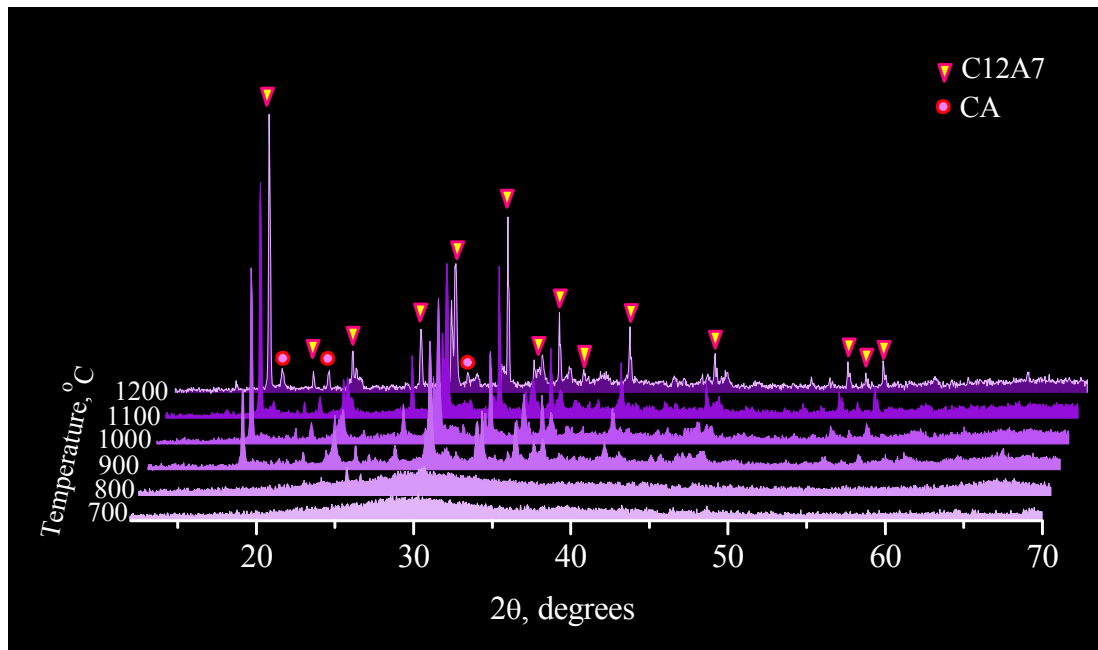


**Figure 4.17 High-temperature X-ray diffraction patterns of the dried gel in a temperature range of 700-1200 °C**

Since the powder is kept at each selected temperature for only a short period of time, the powder remains in amorphous state up to ~ 900 °C. As mentioned earlier, if the dried gel is kept at lower temperatures for several hours, crystalline C12A7 and CaO are formed even at a temperature as low as 700 °C (figure 4.11). As the heat treatment temperature is further increased to 900 °C, C12A7 and CA begin to form. Although C12A7 was originally predicted to be the first product of the CaO-Al<sub>2</sub>O<sub>3</sub> reaction [127], the results show that both phases form simultaneously at this temperature. The concurrent formation of

C12A7 and CA has also been reported in an earlier investigation [119]. It seems that if the powder is held at a temperature of 700 °C for enough heat treatment duration, C12A7 is the only calcium aluminate compound formed. However, if the heat treatment temperature is continuously increased, it is more likely for the crystalline C12A7 to be formed at a higher temperature of 900 °C along with CA.

Further increase in the temperature from 900 to 1200 °C promotes the formation of C12A7 and CA. An interesting observation, however, is the absence of C3A which exists after the powder is kept at temperatures higher than 1000 °C for several hours. It seems that C3A is not formed unless the heat treatment duration is long enough for all the free Al<sub>2</sub>O<sub>3</sub> and CaO to be converted into crystalline C12A7 and CA [127]. The final product of the crystallization treatment after several hours eventually contains C12A7 as the main phase along with CA and C3A as impurities with no trace of calcium oxide or aluminium oxide left in the powder (as reported in the previous section).

#### **4.3.5 Differential scanning calorimetry and thermal gravimetric analysis**

The DSC-TGA plots of the powder are depicted in figure 4.18 for a temperature range of 25–1200 °C.

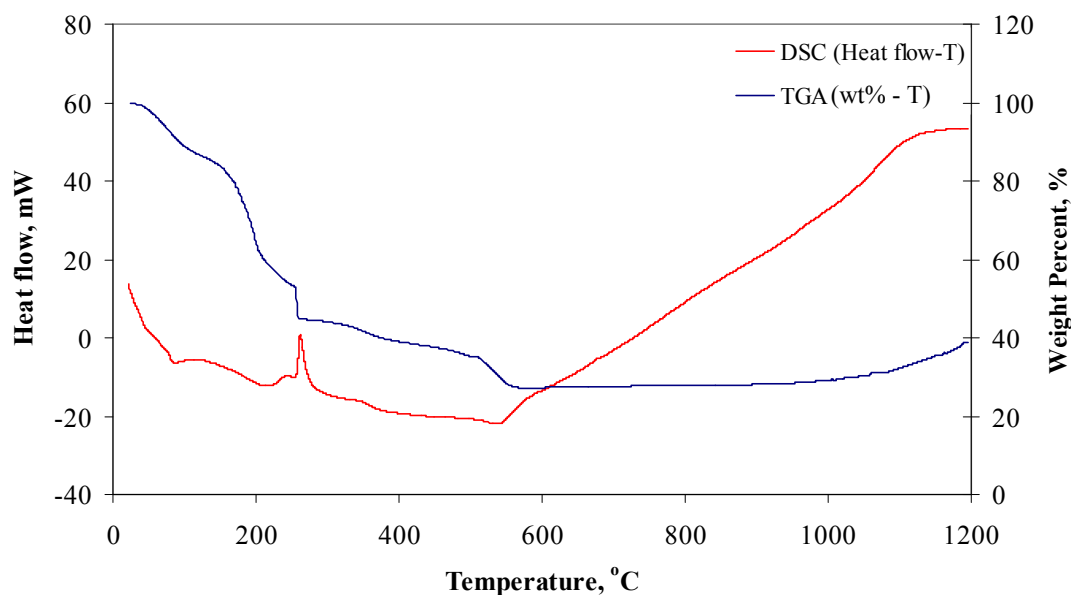


**Figure 4.18 TGA-DSC plots versus temperature for the dried gel during heat treatment at a heating rate of 10 °C/min. A positive heat flow indicates an exothermic process and vice versa.**

The interpretation of TGA-DSC plots along with high-temperature XRD analysis can give a detailed knowledge of the chemical reactions and phase transformations involved during the crystallization treatment of the dried gel. The derivatives of weight percent and heat flow as a function of temperature are plotted in figure 4.19 in order to identify the temperatures at which the weight loss and heat flow changes are more apparent. The chemical reactions and phase transformations predicted to occur during the crystallization treatment of C12A7 based on the TGA-DSC analysis are listed in table 4.5.

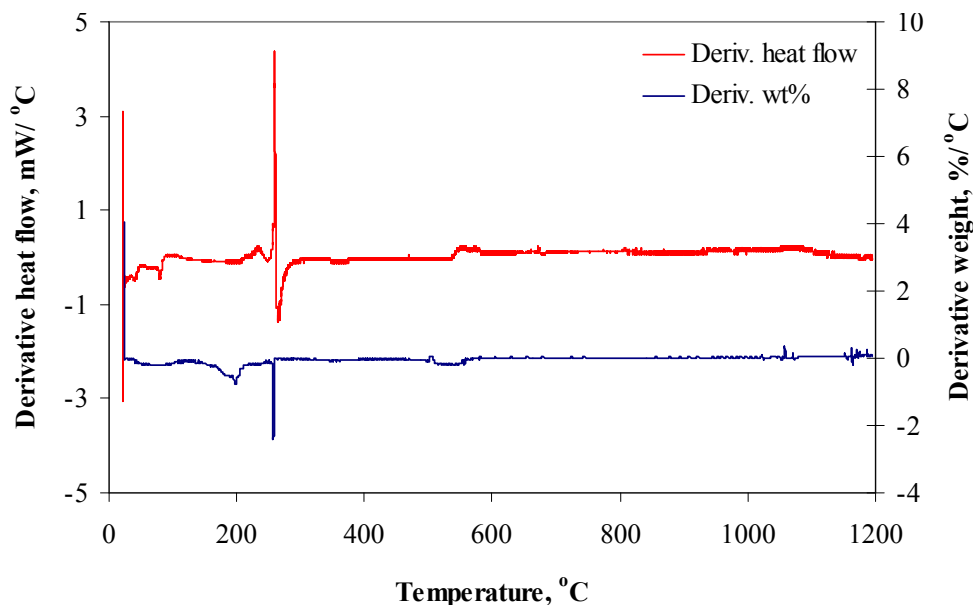


**Figure 4.19** Derivatives of weight percent and heat flow versus temperature for the dried gel during heat treatment at a heating rate of 10 °C/min. A positive heat flow rate indicates an exothermic process.

**Table 4.5** Results of DSC-TGA analysis in a temperature range of 25-1200 °C at a heating rate of 10 °C/min

<i>Temperature (°C)</i>	<i>Weight Percent (%)</i>	<i>Thermal behaviour</i>	<i>Phenomenon</i>	<i>Reference</i>
25-250	63	Endothermic	Evaporation of water and organic solvents, dehydration of calcium nitrate tetrahydrate	[68, 82]
255	53	Exothermic	Oxidation of residual organic compounds	[69]
260-350	43	Endothermic	Dehydration of Gibbsite and formation of Boehmite	[78, 84]
350-500	35	Endothermic	Dehydration of Boehmite and formation of $\gamma$ -Al <sub>2</sub> O <sub>3</sub>	[78, 84]
502	32	Endothermic	Decomposition of calcium nitrate and into calcium oxide	[68]
502-570	27	Endothermic	Further decomposition of calcium nitrate	[68]
1050	36	Exothermic	Crystallization of C12A7 and CA	[47]

Although a slight increase in the heat flow is observed at  $\sim 1050$  °C (figure 4.19), the whole crystallization phenomenon seems to be happening in a wide temperature range rather than a single temperature, leading to a gradual increase in the heat flow. As mentioned in section 4.3.4, the high-temperature XRD results showed that crystalline C12A7 is more likely to be formed rather than crystalline CaO and Al<sub>2</sub>O<sub>3</sub> which is in agreement with DSC-TGA results. No apparent exothermic peaks were observed at  $\sim 850$  and  $\sim 950$  °C that could be attributed to the crystallization of free CaO [68] and Al<sub>2</sub>O<sub>3</sub> [78]. CA phase also showed no separate crystallization peak probably due to simultaneous crystallization with C12A7 [119]. This conclusion is also in accordance with high-temperature XRD observations (section 4.3.4).

# Chapter 5

## FTIR and Raman spectral analysis of C12A7 thin film and powder

### 5.0 Introduction

This chapter presents the Fourier transform infrared (FTIR) and Raman spectroscopy investigations into the effect of heat treatment temperature and duration on the formation of C12A7 in the powder and the thin films.

Two temperatures of 1100 [47, 135] and 1300 °C were chosen as the crystallization treatment temperatures, the latter being reported as a suitable temperature for the solid-state reaction of Al<sub>2</sub>O<sub>3</sub> and CaO mixture [15, 64, 65, 136].

The phase analysis of the spin-coated films was not possible except by Fourier Transform Infrared-Attenuated Total Reflectance (FTIR-ATR) spectroscopy. Raman technique could only be applied to relatively thick films of drop-casted samples with a thickness of 10 μm and higher and X-ray diffraction spectroscopy was not even applicable to very thick films. Two main reasons for the lack of response from the films can be: (1) the films are too thin to be

detected unless a special equipment, such as high-resolution X-ray diffractometer or polarized Raman spectrometer, is used; and (2) the interference from the substrate is too strong. FTIR and Raman spectra only give the vibration bands of MgO substrate and not the film. Therefore, FTIR-ATR technique was utilized in order to analyse the spin-coated and drop-casted films without the interference of the substrate.

### 5.1 FTIR-ATR spectral analysis of the thin films

Figure 5.1 shows the Infrared (IR) spectrum of a spin-coated film (with a thickness of  $\sim 5.5 \mu\text{m}$ ) before the crystallization heat treatment.

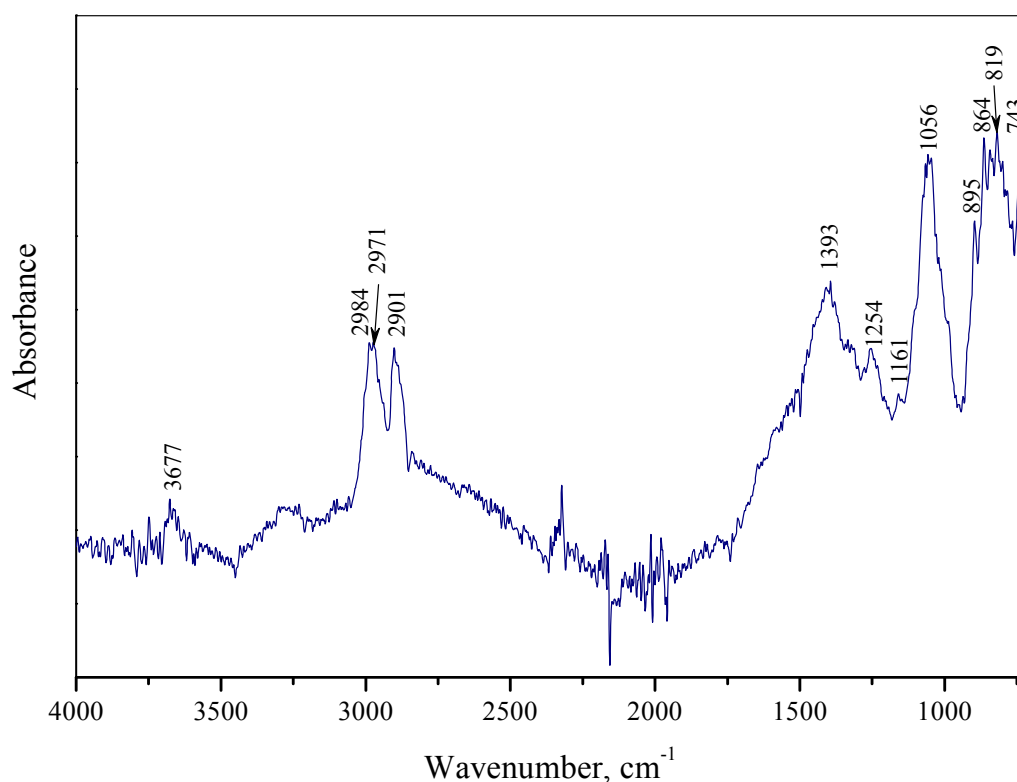


**Figure 5.1 FTIR-ATR spectrum of the as-prepared thin film before the crystallization heat treatment**

The results of the IR spectral analysis in comparison with the peak positions reported in the literature are listed in table 5.1. It is to be noted that the



absorption peaks in the range of 2000-2500  $\text{cm}^{-1}$ , which appear due to environmental effects, were not included in this table.

**Table 5.1 FTIR-ATR absorption bands and the vibrational assignments for the spin-coated films before the crystallization heat treatment**

<i>IR peak position (<math>\text{cm}^{-1}</math>)</i>	<i>Composition</i>	<i>Reference (<math>\text{cm}^{-1}</math>)</i>	<i>Vibration mode</i>
743	Free enolic EAA	740 [68]	C-H bending of alkene
	Chelated EAA	740 [68]	
	Ca(NO <sub>3</sub> ) <sub>2</sub> ·4H <sub>2</sub> O	743 [137]	In-plane bending of NO <sub>3</sub> <sup>-</sup> [138]
	Butyl alcohol	749 [139]	C <sub>3</sub> C-O symmetric stretching [140]
819	Ca(NO <sub>3</sub> ) <sub>2</sub> ·4H <sub>2</sub> O	820 [137]	CH <sub>3</sub> rocking vibrations
	Chelated EAA	818 [68]	
844	Aluminium hydroxide	840 [141]	Out-of-plane bending of Al-OH [68, 142]
864	Free enolic EAA	860 [68]	C-H bending of alkene
895	Butyl alcohol	911 [139]	CH <sub>3</sub> rocking [140]
1056	Free ketonic EAA	1040 [48]	O-C-C stretching
		1042 [69]	
	Ca(NO <sub>3</sub> ) <sub>2</sub> ·4H <sub>2</sub> O	1045 [137]	Symmetric stretching of N-O [138]
	Aluminium hydroxide	1060 [141]	In-plane bending vibrations of Al-OH bonds [141, 142]
		1069 [143]	
Chelated aluminium hydroxide	1059 [68]		
1161	Chelated aluminium hydroxide	1176 [143]	In-plane bending vibrations of Al-OH bonds [142]
		1167 [68]	
		1168 [69]	
	Free ketonic EAA	1153 [143]	-C-C-O stretching of ketonic form
		1155 [68]	
		1160 [69]	

**Table 5.1 Continued**

<i>IR peak position (cm<sup>-1</sup>)</i>	<i>Composition</i>	<i>Reference (cm<sup>-1</sup>)</i>	<i>Vibration mode</i>
1254	EAA	1256 [143]	-CH <sub>2</sub> - vibration (or -CH <sub>3</sub> or -CH <sub>2</sub> ) Methylene (CH <sub>2</sub> ) twisting and wagging vibrations
		1254 [68]	
	Butyl alcohol	1236 [139]	CC <sub>4</sub> skeletal stretching
		1238 [140]	
1380	Chelated EAA	1382 [143]	-CH <sub>2</sub> vibration (or -CH <sub>3</sub> or -CH <sub>2</sub> -)
		1379 [69]	
1409	Free enolic EAA	1415 [143]	C-H rocking vibration of alkene
		1415 [68]	
		1411 [69]	
1528	Chelated EAA	1525 [68]	C-C vibration of six-membered ring of the chelate
		1530 [143]	
		1530 [69]	
1617	Chelated EAA	1610 [68]	C-O of enolic EAA bonded to Al
		1619 [143]	
		1624 [69]	
1713	Free ketonic EAA	1718 [68]	C=O stretching vibrations of two carbonyl groups
		1720 [69]	
		1731 [143]	
2901	Free ketonic EAA	2881 [68]	Symmetrical C-H stretching of CH <sub>3</sub>
2971	Butyl alcohol	2971 [139]	CH <sub>3</sub> asymmetric stretching
		[140]	
2984	Free ketonic EAA	2980 [68]	Symmetrical stretching of C-H bonds in methyl group
	Chelated EAA	2986 [68]	
		2990 [69]	
3677	Aluminium hydroxide	3670 [141]	Stretching vibrations of hydroxyl groups bonded to aluminium [68]

Similar IR peaks have been observed for the dried gel prepared with Ethyl acetoacetate-to-Aluminium sec-butoxide (EAA-to-ASB) molar ratios of 3:1 and 2:1.

A few absorption peaks are in good match with the absorption peaks of non-chelated aluminium hydroxide. The presence of “free” aluminium hydroxide in the dried gel might be due to two possible reasons: (1) aluminium butoxide is not completely chelated in the solution and is hydrolyzed in non-chelated form, and/or (2) some of the ethyl acetoacetate is released upon hydrolysis [68] which leads to the formation of free aluminium hydroxide. However, the former phenomenon is less likely to occur due the relatively high EAA-to-ASB ratio. Free aluminium hydroxide is also present in the dried gel obtained from a solution with the EAA-to-ASB molar ratio of 3:1. It has been reported in the literature [77] that a high EAA-to-ASB ratio of 3:1 might even prevent a complete hydrolysis due to the strong bonding between the alkoxide and the chelating agent. In addition, the presence of free aluminium butoxide in the solution results in a rapid precipitation of aluminium hydroxide upon the addition of water, causing the solution to lose its transparency and become unstable. However, solutions with the EAA-to-ASB molar ratios of 2:1 and 3:1 showed no signs of uncontrollable precipitation upon the addition of water and remained transparent and stable. Therefore, it is concluded that the partial release of ethyl acetoacetate during hydrolysis is more likely to be the reason for the presence of free aluminium hydroxide. The appearance of some peaks that only exist for ester in the free ketonic or enolic form, such as  $740$  and  $2980\text{ cm}^{-1}$ , further confirms the partial release of ethyl acetoacetate. As long as the bonding between the alkoxide and the chelating agent is partially preserved, the solution

remains transparent and stable. The sol-to-gel transformation further promotes the hydrolysis and the release of the chelating agent.

No matching peaks were observed for the solvent used in the solution which shows that the solvent is evaporated almost completely during the drying process. The absorption peaks at 2971, 1254, 844 and 743  $\text{cm}^{-1}$  show the possible presence of Butyl alcohol which is predicted to be the by-product of the hydrolysis of chelated (and non-chelated) aluminium butoxide [77].

Some peaks can be assigned to more than one possible component (given in table 5.1), while some peaks might be located at regions which are overlapped by other high-intensity peaks [68].

The IR spectrum of a thin film which was heat treated at 1100 °C for 4 hr is shown in figure 5.2.

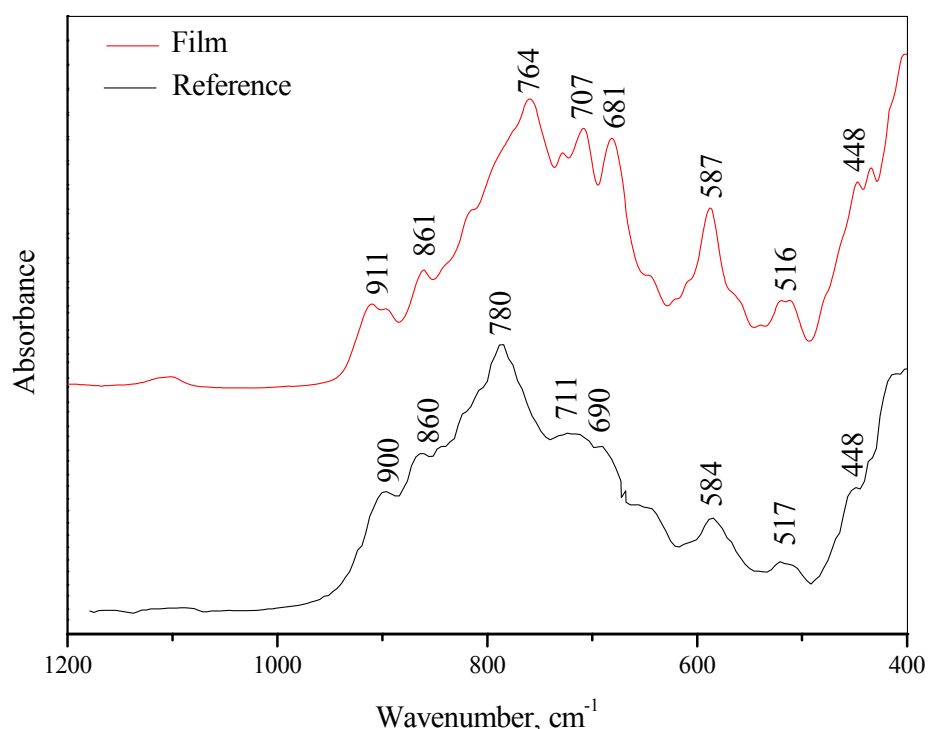


**Figure 5.2 FTIR-ATR spectrum of the thin film after heat treatment at 1100 °C for 4 hr under air atmosphere. The structure mainly consists of C5A3. The reference spectrum [144] is obtained from a C5A3 sample synthesized through a melt-solidification process at 1600 °C in a carbon crucible under the flow of argon.**

A comparison between the IR absorption peaks of the thin film and the ones previously reported in the literature shows that the main phase forming after the heat treatment at 1100 °C is in fact C5A3 and not C12A7. The reason may be attributed to a restrained crystallization of C12A7 on MgO substrate [145].

C12A7 and C5A3 are quite similar in chemical composition with 48.5 and 47.8 % mass of CaO respectively [27, 144]. However, they are not considered as polymorphs and are believed to form under different heat treatment atmospheres [144]. The main difference between these two phases is the absence of a nanoporous structure in C5A3 [27]. Schematic configurations of the Ca polyhedra in C12A7 and C5A3 are shown in figure 5.3. The  $\text{AlO}_4$  tetrahedra in C5A3 form a network of five-membered rings with a layered arrangement of Ca atoms. In C12A7, however, three irregular Ca octahedra share an edge and are joined with an Al tetrahedron through a four-coordinated oxygen atom forming a two-dimensional sheet structure [146].

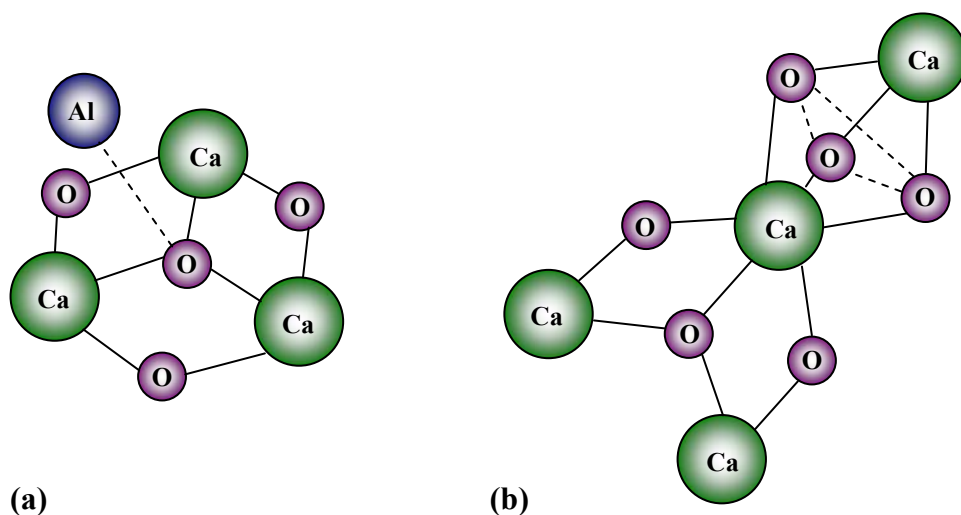


**Figure 5.3 Schematic configuration diagrams of Ca polyhedra in (a) crystalline C12A7, and (b) crystalline C5A3 [146]**

In order to investigate the possibility of a phase transformation from C5A3 to C12A7, C5A3 thin films were additionally heat treated at 1100 and 1300 °C for 5 hr. The IR spectrum of a thin film heat treated at 1100 °C for a further duration of 5 hr is depicted in figure 5.4.

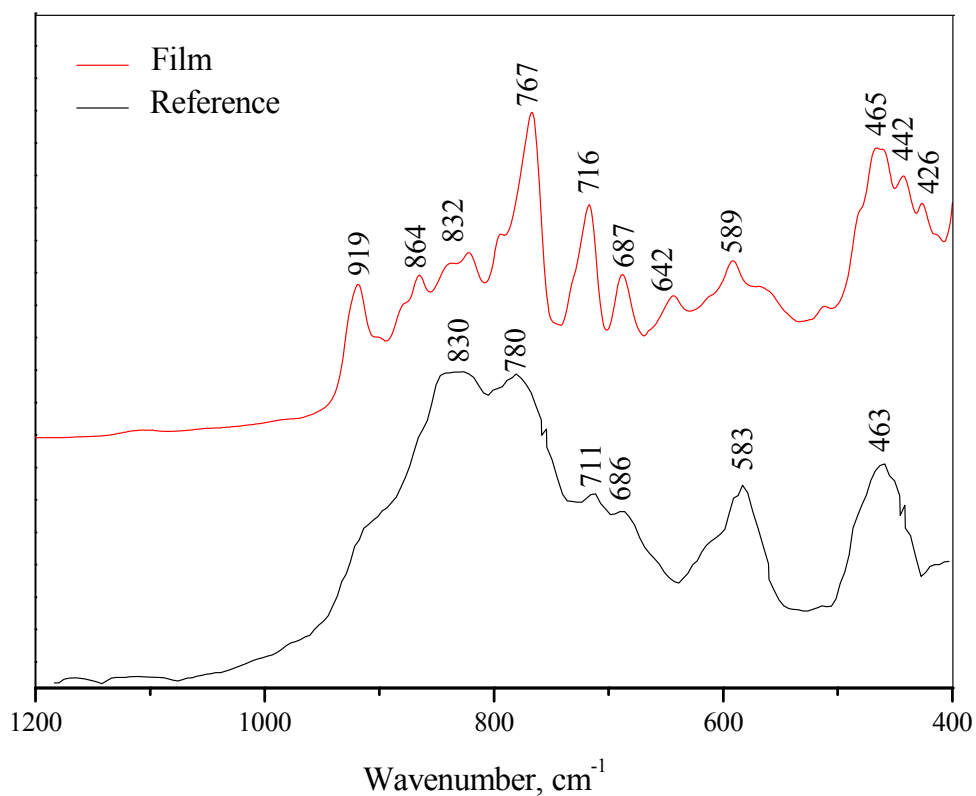


**Figure 5.4** FTIR-ATR spectrum of the thin film treated at 1100 °C initially for 4 hr and then for a further 5 hr under air atmosphere. The structure consists of C5A3 and C12A7. The reference spectrum [144] is obtained from an originally C12A7 bulk which was heat treated at 1300 °C under a vacuum atmosphere and consists of a C12A7-C5A3 mixture.

The phase analysis of the film in comparison with a reference spectrum (obtained from a two-phase bulk) showed a progress towards the formation of C12A7, and a C5A3-C12A7 mixture is formed. Two new peaks appearing at 465 and 832 cm<sup>-1</sup> are in good match with the IR peaks observed for C12A7 [144, 147]. In spite of the appearance of C12A7 absorption peaks, the IR peaks of

C5A3 at 589, 780, 864 and 919  $\text{cm}^{-1}$  are still present which means that the co-existence of this phase in the structure cannot be neglected. The difference between the intensity of the peaks obtained from the sample and the reference might be attributed to the different volume fraction of the two phases in each mixture.

It has been reported that C5A3 transforms into C12A7 in the presence of oxygen in the atmosphere. In this case, however, a complete transformation from C5A3 to C12A7 under normal air atmosphere might need long hours of heat treatment. In addition, the substrate can be a restricting factor in the phase transformation of the film. Therefore, it is concluded that in order to favour the formation of C12A7 over C5A3, either the heat treatment temperature or atmosphere should be changed. Since the presence of oxygen is essential as the template for the formation of the C12A7 cage structure and the entrapment of oxygen ions inside the cages [2, 29], the formation of this phase is facilitated under an oxygen-enriched atmosphere. However, increasing the volume fraction of oxygen is extremely risky due to a possible exothermic reaction of oxygen with hydrogen at such high temperatures. In addition, the aim is to utilize a simple and cost-effective technique for the fabrication of thin films. Therefore, the heat treatment atmosphere was kept unchanged and the effect of heat treatment temperature on the phase formation was investigated instead.

During the first step of the investigation, the thin films of C5A3 were additionally heat treated at a higher temperature of 1300 °C for 2 hr. The IR absorption spectrum of the film is shown in figure 5.5.

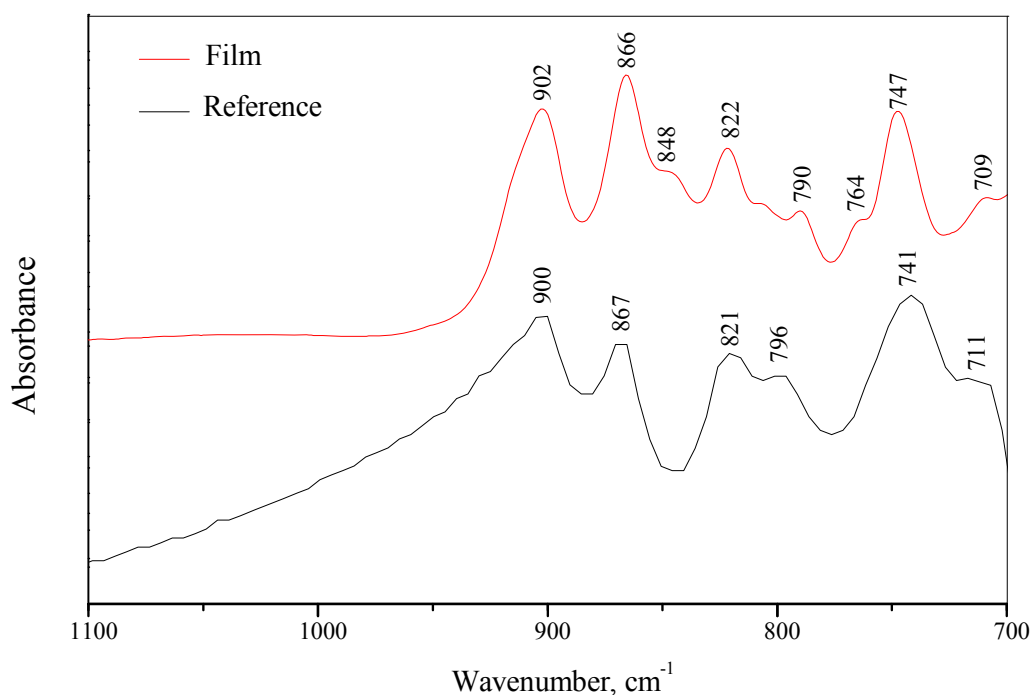


**Figure 5.5 FTIR-ATR spectrum of the thin film initially heat treated at 1100 °C for 4 hr and then at 1300 °C for 2 hr under an air atmosphere. The structure consists mainly of C3A and C5A3. The reference spectrum [21] is obtained from a C3A bulk which was synthesized through a self-combustion technique.**

The heat treatment of C5A3 thin films at 1300 °C resulted in a partial transformation of this phase to C3A. Since C3A is thermodynamically more stable than C12A7 [37], increasing the heat treatment temperature to 1300 °C in an air atmosphere seems to be in favour of a conversion from C5A3 to C3A rather than C12A7. Another possible explanation for the preferable formation of C5A3-C3A mixture over single phase C12A7 might be the lack of essential templates in the atmosphere during the heat treatment at this temperature [2]. It is to be noted that this conclusion might only be valid for thin films and a different phenomenon might occur for the compound in bulk or powder form.

In the second step of the investigation, a new set of thin films were prepared and heat treated at 1300 °C for 2 hr. Since the effect of a temperature as high as



1300 °C on the interaction between the thin film and the MgO substrate has not been reported elsewhere, the heat treatment duration was kept at 2 hr in order to minimize any possible chemical reactions at the film/substrate interface and ensure the crystallization of the film. The FTIR-ATR spectrum of the film is depicted in figure 5.6.

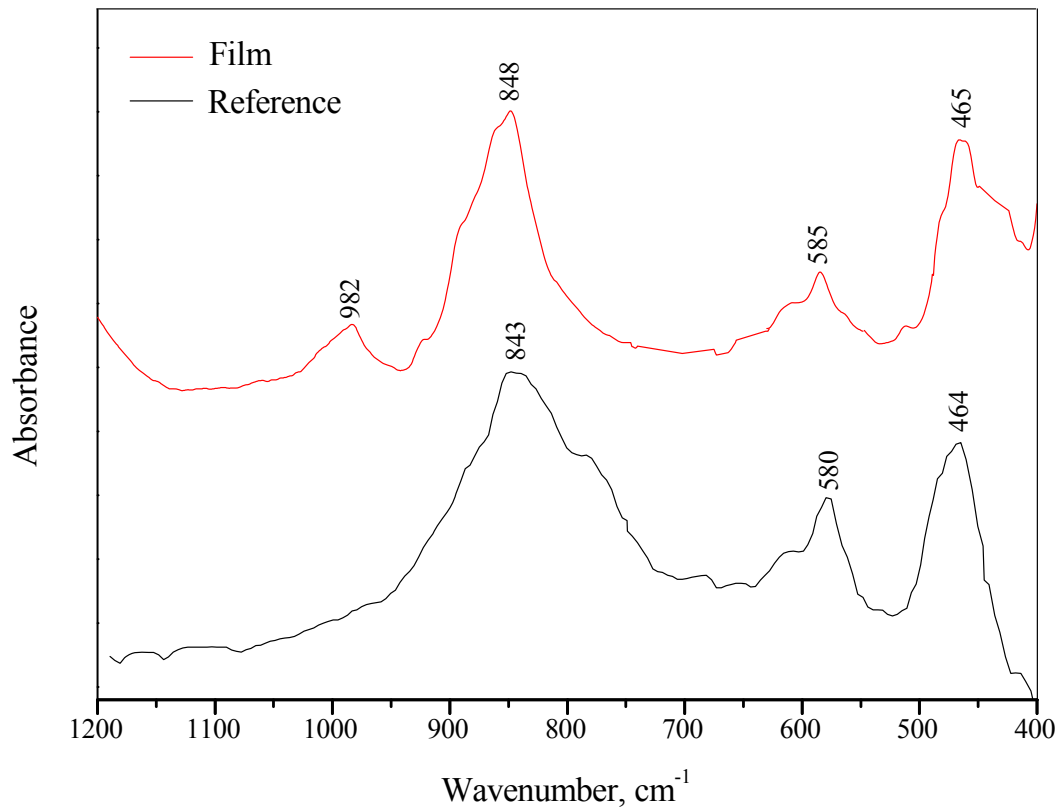


**Figure 5.6 FTIR-ATR spectrum of the thin film after heat treatment at 1300 °C for 2 hr under an air atmosphere. The structure mainly consists of C12A7. The reference spectrum [144] is obtained from a melt-solidification process at 1300 °C under dry oxygen atmosphere.**

The result of the phase analysis shows the formation of a single-phase C12A7 after a heat treatment at 1300 °C under air atmosphere. The appearance of two high-intensity absorption peaks at 465 and 848 cm<sup>-1</sup> and the non-existence of all C5A3 medium-to-high intensity peaks at 448, 516, 587, 681, 707, 764 and 911 cm<sup>-1</sup> confirm that the temperature of 1300 °C is high enough for the

preferable formation of C12A7 even at lower heat treatment duration of 2 hr compared to the previous heat treatments employed. The only main difference between the absorption spectrum of the thin film and the one of the reference (figure 5.6) is the appearance of a peak at  $982\text{ cm}^{-1}$  which has been reported to appear occasionally as well as two additional peaks at  $1020$  and  $1500\text{ cm}^{-1}$  [147]. Although some of the absorption peaks of C12A7 and C5A3 might be positioned at similar frequencies, the sharp absorption peak at  $848\text{ cm}^{-1}$  is characteristic of C12A7 which makes it quite easy to be distinguished from C5A3 [144]. This absorption peak is the fundamental absorption band of C12A7 and corresponds to the vibration modes of the bonded tetrahedra Al-O bonds [147].

In C12A7 lattice, aluminium atoms form distorted tetrahedra with oxygen atoms, while some of the  $\text{AlO}_4$  groups transform to  $\text{AlO}_5$  [147]. The fundamental absorption band of calcium aluminate compound shifts to higher or lower frequencies depending on the type of calcium aluminate phase. This shift can be explained by the change in the coordination number of aluminium as the concentration of CaO in the compound changes.

Aluminium can form different structural functions with the coordination number varying from 4 to 6 through an irregular 5 coordination. This element is the only structurally-decisive element in calcium aluminate binary compounds [147]. The range of vibration frequencies for isolated and bonded Al-O bonds is listed in table 5.2.

**Table 5.2 Vibration frequencies of isolated and bonded Al-O octahedra and tetrahedra [147, 148]**

<i>Al<sup>IV</sup> – O tetrahedra</i> ( <i>cm<sup>-1</sup></i> )	<i>Al<sup>VI</sup> – O octahedra</i> ( <i>cm<sup>-1</sup></i> )	<i>Status</i>
700-900	500-680	Bonded
650-800	400-540	Isolated

As the concentration of CaO in Al<sub>2</sub>O<sub>3</sub> increases, CA becomes stable (according to the CaO-Al<sub>2</sub>O<sub>3</sub> phase diagram, figure 2.1). The structure of this phase consists of a skeleton of Al-O tetrahedra. The presence of CaO in the structure and the strong stress of the lattice induced by excess charge cause the deformation and stretching of the Al-O bonds. Additional bands appearing at low frequencies in the spectrum of CA are due to an extremely stressed structure. In this case, significant deformation and bond stretching of the lattice make the whole spectrum to shift towards lower frequencies. The absorption bands mainly appear in three regions and are attributed to the vibrations of the isolated tetrahedra (650 – 730 cm<sup>-1</sup>) and the bonds with coordination numbers of 5 (580 – 620 cm<sup>-1</sup>) and 6 (540 – 560 cm<sup>-1</sup>) [147].

A further increase in CaO concentration leads to an increase in the lattice stress up to point where the skeleton of CA breaks down and C12A7 structure is formed instead. The reorganisation of the structure causes the aluminium with coordination numbers of 4 and 5 to be stabilized. As a result, the deformation and bond stretching is decreased and the lattice becomes more relaxed. The appearance of medium-to-high intensity absorption bands at 850 and 580 – 620 cm<sup>-1</sup> accompanied by the disappearance of low-frequency absorption

bands further confirm the lattice relaxation through the formation of a new phase [147].

Since the absorption bands of bonded tetrahedra and octahedra are in the regions of  $700-900\text{ cm}^{-1}$  and  $500-700\text{ cm}^{-1}$  respectively (table 5.2), it is reasonable to expect the Al-O bond in C12A7 with an Al coordination number of 5 to show an absorption band lying in between the vibrational frequencies of tetrahedron and octahedron [147].

A further increase in the concentration of CaO results in the formation of C3A. It was previously believed that upon the formation of this phase, the coordination number of aluminium partially increases to 6 and a combination of  $\text{AlO}_4$  and  $\text{AlO}_6$  exist in the crystal structure [147]. However, Mondal et al suggested that the unit cell of C3A is actually built up of six-fold rings, each composed of six distorted  $\text{AlO}_4$  tetrahedra, with  $\text{Ca}^{2+}$  ions holding the rings together [149].

It has been previously mentioned (sections 2.7.3 and 2.8.1) that the heat treatment of C12A7 in a reducing atmosphere of  $\text{H}_2\text{-N}_2$  results in the substitution of extra-framework oxygen ions with hydride (H) and hydroxide (OH) species, most of which are believed to be H<sup>-</sup> ions [9, 40, 90, 91]. In order to investigate the IR absorption behaviour of C12A7 after a heat treatment in a hydrogen atmosphere, the FTIR-ATR spectra of the thin films were obtained after a heat treatment at  $1300^\circ\text{C}$  for 2 hr under a reducing atmosphere of 5% $\text{H}_2$ -95% $\text{N}_2$  and rapid cooling to room temperature. Figure 5.7 shows a comparison between the IR spectra of a C12A7 thin film before and after such heat treatment.

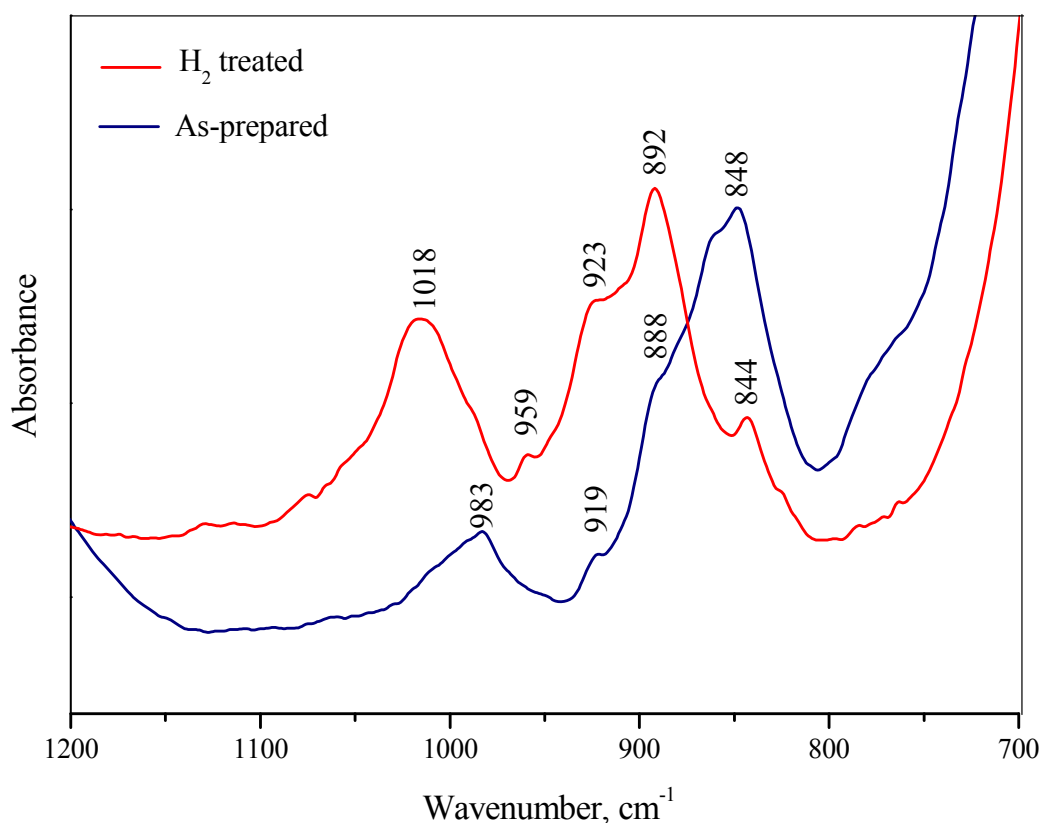


**Figure 5.7 FTIR-ATR spectra of the C12A7 thin film in the as-prepared state and after heat treatment at 1300 °C for 2 hr under a 5%H<sub>2</sub>-95%N<sub>2</sub> atmosphere. The vibration bands shift towards higher frequencies after H<sub>2</sub> treatment.**

The whole spectrum seems to have shifted towards higher frequencies with a new high-intensity band appearing at 892 cm<sup>-1</sup>. The position of the FTIR absorption bands is affected by several inter-related factors such as Al coordination number, the state of the coordination group (being isolated or condensed), and the vibrational frequencies between the neighbouring groups [37]. In general, any factor that has an effect on the force constant of a bond can change the vibration frequency of that bond [150]. It is, therefore, reasonable to expect a shift in the IR absorption bands due to a partial substitution of extra-framework oxygen ions with hydrogen species. Although the FTIR spectral behaviour of C12A7:H has not been investigated elsewhere, a shift in Raman

peaks compared to the ones of the stoichiometric C12A7 has been reported due to the incorporation of  $^{16}\text{O}$  and  $^{18}\text{O}$  species inside the cage structure [26]. In that case, a red-shift of the Raman peaks was observed and attributed to the presence of species with higher mass compared to stoichiometric  $\text{O}^{2-}$  ions. In our case, the appearance of  $892\text{ cm}^{-1}$  peak can be related to a shift from the  $844\text{ cm}^{-1}$  fundamental absorption band of the Al-O bonds at the cage wall due to the incorporation of new species inside the cages [40]. Since  $\text{H}^-$  ions have smaller radius and lower negative charge compared to  $\text{O}^{2-}$ , a blue-shift of the absorption bands is a reasonable behaviour. A peak at  $844\text{ cm}^{-1}$  is also observed which might be attributed to the vibrational frequency of the unaffected Al-O bonds, although the intensity of this band is much lower compared to the one appearing before the heat treatment.

In order to determine whether this type of behaviour is exclusive to C12A7, a similar heat treatment procedure was applied to the C5A3 thin film which has a quite similar chemical composition, but no cage structure. The FTIR-ATR spectra of a thin film before and after heat treatment under the reducing atmosphere are depicted in figure 5.8.

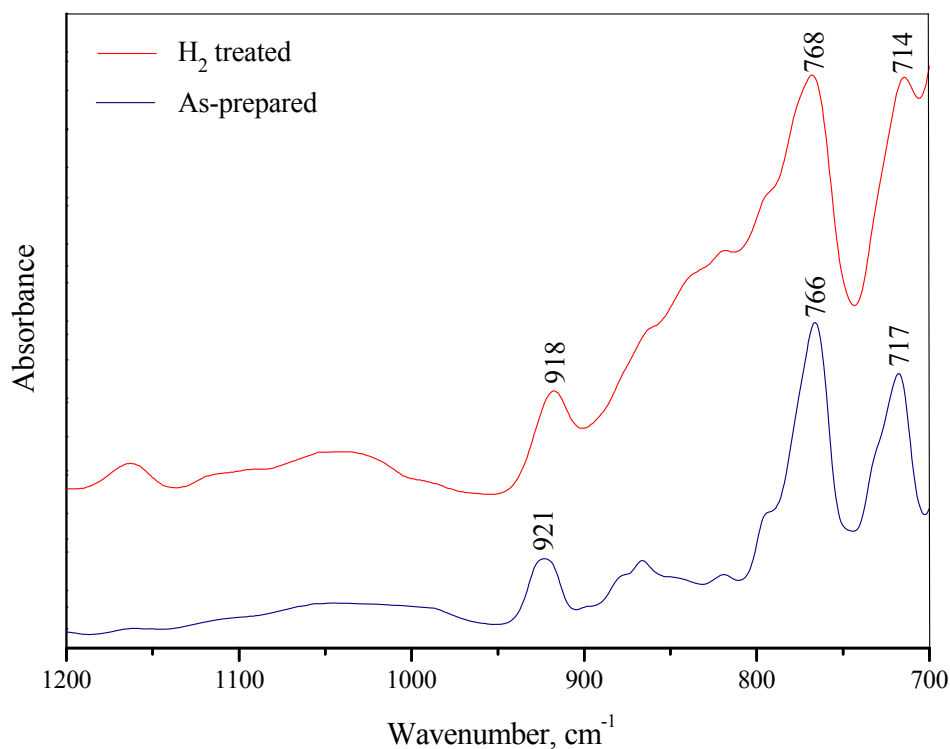


**Figure 5.8 FTIR-ATR spectra of the C5A3 thin film in the as-prepared state and after heat treatment at 1300 °C for 2 hr under a 5%H<sub>2</sub>-95%N<sub>2</sub> atmosphere. The vibration bands have remained in the original positions.**

It is clearly observed that the heat treatment in a H<sub>2</sub>-N<sub>2</sub> reducing atmosphere has no significant effect on the position of the absorption peaks or the chemical composition of C5A3 film. Therefore, the shift of the absorption peaks in C12A7 must be related to the cage structure of this compound.

## 5.2 Raman spectral analysis of the powder and the thin films

Since the thickness of the spin-coated films was too small for Raman spectroscopy, this technique was only employed for the phase analysis of the drop-casted films (with thicknesses higher than 10 μm) and the powder. The Raman spectrum of the dried gel in powder form before the crystallization treatment is depicted in figure 5.9.

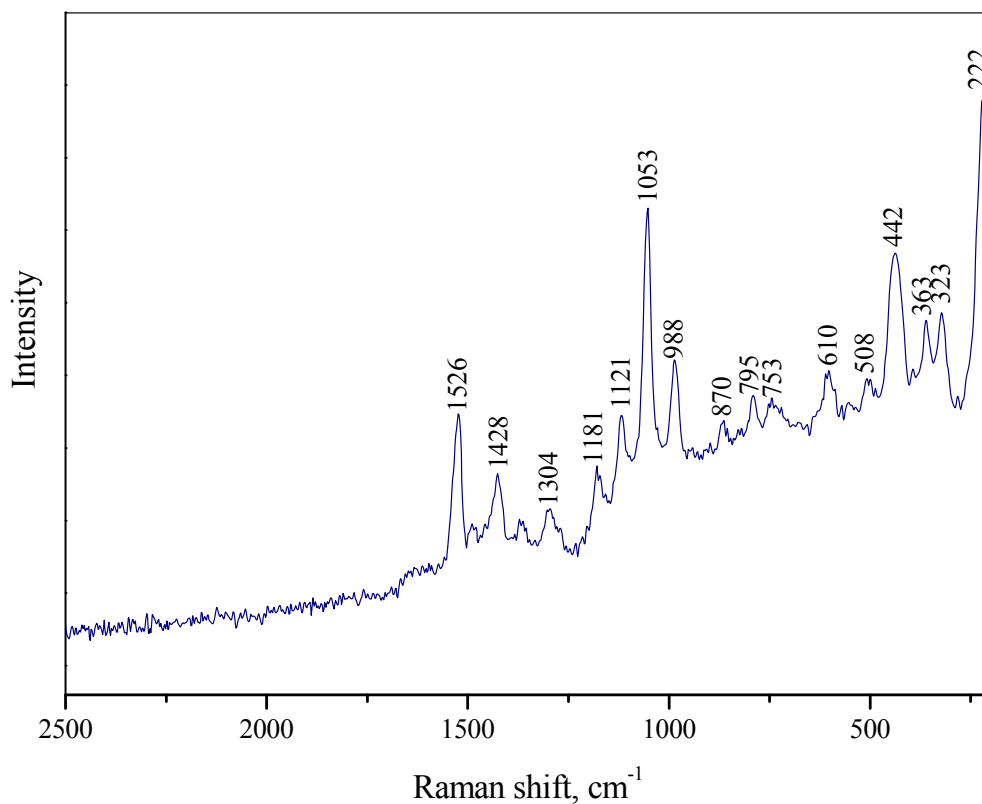


**Figure 5.9** Raman spectrum of the dried gel before the crystallization heat treatment

The results of the Raman spectral analysis along with the vibrational assignments for the observed peaks are given in table 5.3.

**Table 5.3** Raman absorption bands and the vibrational assignments for the dried gel before the crystallization heat treatment

<i>Raman peak position (cm<sup>-1</sup>)</i>	<i>Composition</i>	<i>Reference (cm<sup>-1</sup>)</i>		<i>Vibration mode</i>
222	Aluminium hydroxide	228	[142]	Al-O stretching
323	Aluminium hydroxide	322	[142]	Al-O stretching
363	Aluminium hydroxide	360	[142, 151]	Al-O stretching [142]
442	Aluminium hydroxide	444	[142]	Al-O stretching
		447	[151]	



Table 5.3 Continued

<i>Raman peak position</i> ( $cm^{-1}$ )	<i>Composition</i>	<i>Reference</i> ( $cm^{-1}$ )		<i>Vibration mode</i>
508	Aluminium hydroxide	506	[142]	Al-OH bending
610	Aluminium hydroxide	617	[141, 142]	Al-OH bending [142]
738	Ca(NO <sub>3</sub> ) <sub>2</sub> .4H <sub>2</sub> O	740	[137]	In-plane bending of NO <sub>3</sub> <sup>-</sup> [138]
753	Butyl alcohol	752	[140]	C3C-O symmetric stretching  Out-of-plane OH bending
	Aluminium hydroxide	755	[141]	
		751	[142]	
795	Aluminium hydroxide	788	[142]	Out-of-plane OH bending
870	EAA	878	[152]	Skeletal vibrations of C-C bonds
988	Aluminium hydroxide	980	[142]	In-plane OH bending
1053	Ca(NO <sub>3</sub> ) <sub>2</sub> .4H <sub>2</sub> O	1050	[137]	Symmetric stretching of N-O [138]  In-plane OH bending  O-CH <sub>2</sub> stretching
	Aluminium hydroxide	1051	[142]	
	EAA	1053	[152]	
1121	EAA	1114	[152]	Out-of-plane stretching of C-C
1181	EAA	1185	[152]	C-C backbone bending
1304	EAA	1298	[152]	CH <sub>2</sub> twisting
1374	Butyl alcohol	1365	[140]	CH <sub>3</sub> symmetric deformation  In-plane bending of C-Me <sub>2</sub>
	EAA	1380	[152]	
1428	Ca(NO <sub>3</sub> ) <sub>2</sub> .4H <sub>2</sub> O	1450	[137]	Out-of-Plane stretching of N-O [138]
1526	Chelated EAA	1528	[68]	Corresponding to 1530cm <sup>-1</sup> IR band
2920	EAA	2916	[152]	Asymmetric stretching of CH <sub>3</sub>
2939	EAA	2939	[152]	Symmetric stretching of CH <sub>2</sub>

Since the Raman absorption data of chelated aluminium hydroxide and chelated ethyl acetoacetate has not been previously reported in the literature, the comparison is made with the Raman absorption data available for non-chelated “free” aluminium hydroxide and ethyl acetoacetate. Three absorption peaks at 753, 1053 and 1374  $\text{cm}^{-1}$  can be assigned to more than one chemical bond.

A comparison between the observed Raman and IR absorption peaks reveals that some of the vibration modes are both Raman and IR active. The position of these bands is given in table 5.4 along with the vibrational assignments.

**Table 5.4 Comparison between the results of the spectral analyses for similar Raman-active and FTIR-active peak positions**

<i>Raman-active peak position (<math>\text{cm}^{-1}</math>)</i>		<i>FTIR-active peak position (<math>\text{cm}^{-1}</math>)</i>	
738	Ca(NO <sub>3</sub> ) <sub>2</sub> .4H <sub>2</sub> O [137]	743	Ca(NO <sub>3</sub> ) <sub>2</sub> .4H <sub>2</sub> O [137]
870	Free EAA [152]	864	Free EAA [68]
1053	Free EAA [152] Ca(NO <sub>3</sub> ) <sub>2</sub> .4H <sub>2</sub> O [137] Aluminium hydroxide [142]	1056	Free EAA [68] Ca(NO <sub>3</sub> ) <sub>2</sub> .4H <sub>2</sub> O [137] Aluminium hydroxide [141]
1374	EAA [152]	1380	Chelated EAA [143]
1526	Chelated EAA according to the observed FTIR peak	1528	Chelated EAA [68]

From the comparison in table 5.4, it is apparent that the Raman and IR spectral analyses are in accordance with each other. This type of comparison is useful in order to confirm the presence of an unknown compound. The identity of the Raman absorption peak at 1526  $\text{cm}^{-1}$  has been determined by comparing the position of this peak with a similar FTIR peak position of chelated ethyl acetoacetate [68].

Figure 5.10 shows the Raman spectrum of the powder prepared by the heat treatment of the dried gel at a temperature of 1300 °C for 4 hr. A reference spectrum of a single-phase C12A7 bulk [144] has also been included for comparison.

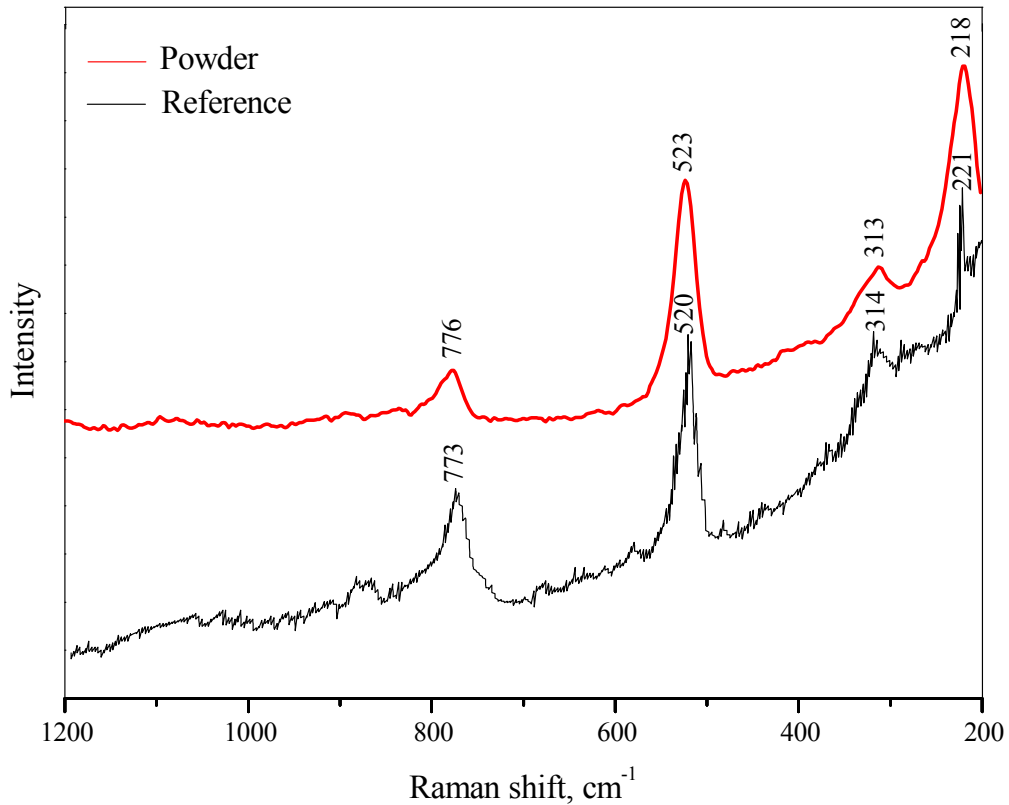


**Figure 5.10 Raman spectrum of C12A7 powder obtained from the heat treatment of the dried gel at 1300 °C for 4 hr. The reference spectrum [144] is from a crystalline C12A7 bulk which was prepared by a melt-solidification process at 1500 °C in a dry oxygen atmosphere.**

As can be seen from the figure, the Raman peaks of the powder match quite well with the ones of the reference confirming the formation of C12A7. However, the results of the phase analysis show the co-existence of secondary phases in the crystallized powder which is mainly due to a non-uniform mixture of the ingredients. The Raman spectra of these secondary phases are depicted in

figure 5.11 in comparison with the Raman spectrum of C12A7 (also obtained from the powder).

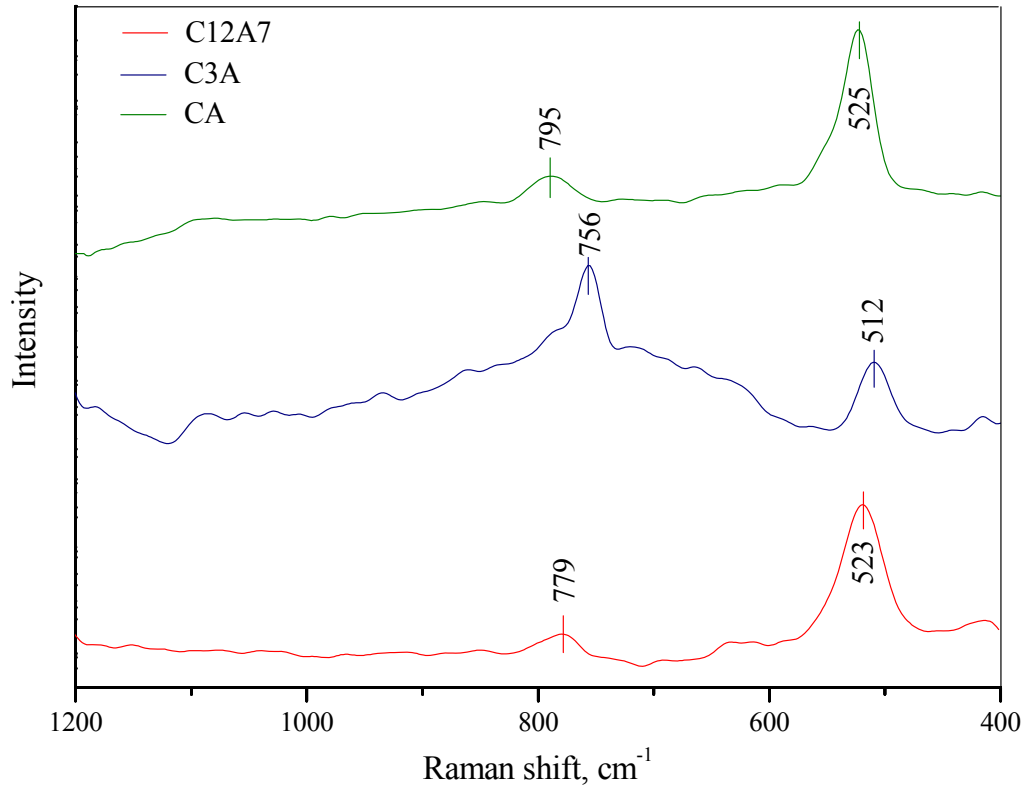


**Figure 5.11 Raman spectra of the secondary phases, CA and C3A, which were formed during the solid-state reaction treatment of the powder. The Raman spectrum of C12A7 is also obtained from the powder.**

As can be seen from the figure, apart from C12A7, two additional phases, CA and C3A, are identified to be present in the powder. The Raman spectra of these three phases can be easily distinguished from each other by the position of two main absorption bands in the regions of  $\sim 500\text{-}530\text{ cm}^{-1}$  and  $\sim 750\text{-}850\text{ cm}^{-1}$  belonging to the stretching modes of Al-O bonds [153]. The presence of secondary phases, such as CA and C3A, has been reported in the literature even after very long hours of heat treatment and has been mentioned to be almost inevitable in the solid-state reaction technique [37, 65].

As mentioned previously (section 5.1), the IR phase analyses of the crystallized films show that the films mainly consist of C5A3 and C12A7 after heat treatment at 1100 and 1300 °C respectively. The Raman behaviour of the films was also investigated in order to confirm results of the FTIR spectral analysis. The Raman spectrum of a thin film heat treated at 1100 °C for 4 hr is shown in figure 5.12. A reference spectrum [144] has also been included for comparison.

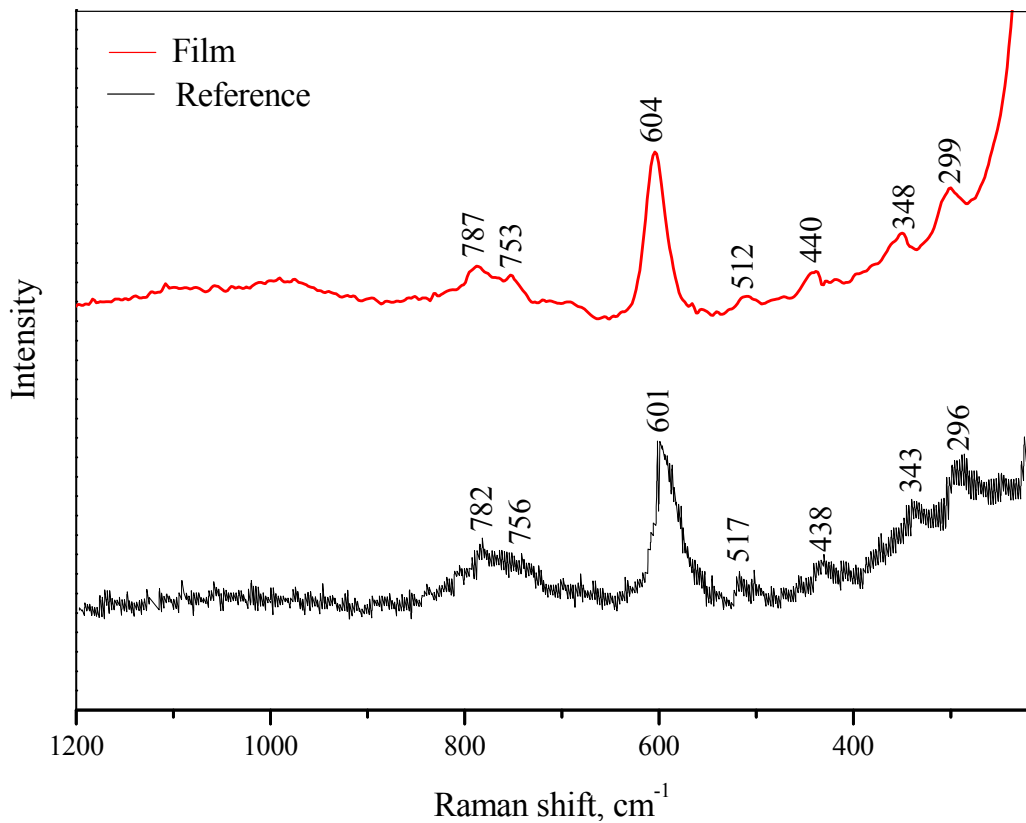


**Figure 5.12 Raman spectrum of the drop-casted film after a heat treatment at 1100 °C for 4 hr in air atmosphere. The reference spectrum [144] is obtained from a crystalline C5A3 bulk which was prepared by a melt-solidification process at 1500 °C in an atmosphere of argon.**

The result of the Raman spectral analysis shows the formation of C5A3 after a heat treatment at 1100 °C which is in accordance with FTIR results (figure 5.2).

Although some of the Raman-sensitive peak positions of C5A3 are rather similar to C12A7, the appearance of a high-intensity peak at  $\sim 600\text{ cm}^{-1}$  is characteristic of C5A3 phase [144]. A few additional bands are also observed in the spectrum of C5A3, such as  $348, 440$  and  $753\text{ cm}^{-1}$ , which can be useful in order to distinguish between the two phases.

The Raman spectrum of a thin film after a heat treatment at  $1300\text{ }^{\circ}\text{C}$  for 2 hr is depicted in figure 5.13.

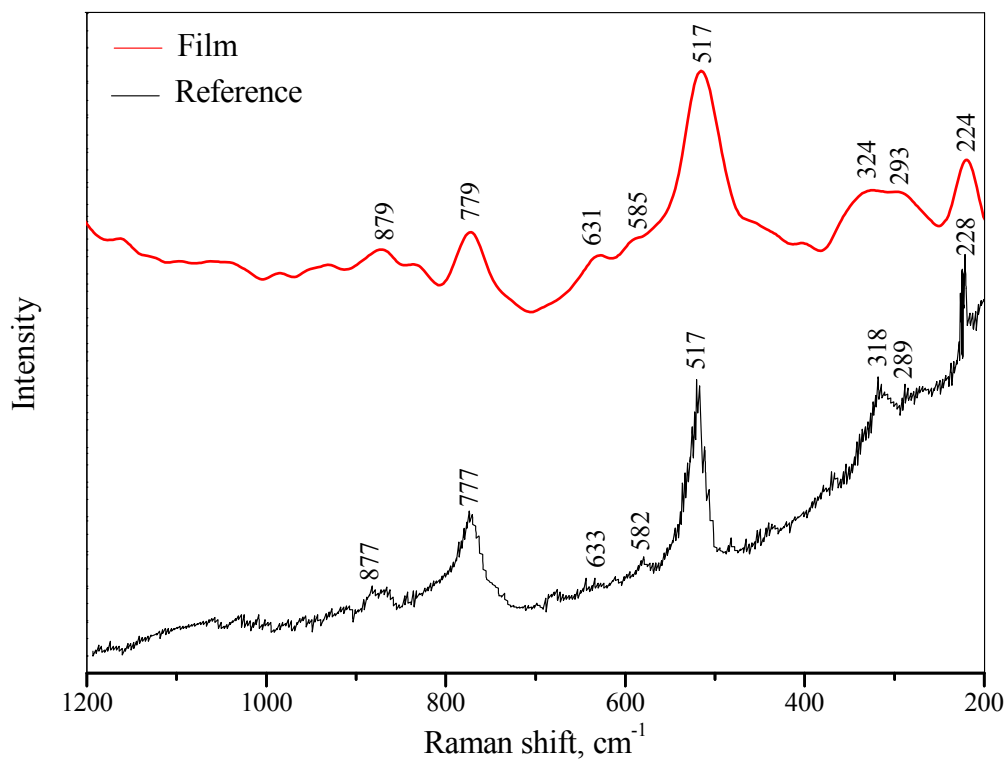


**Figure 5.13** Raman spectrum of the drop-casted film after a heat treatment at  $1300\text{ }^{\circ}\text{C}$  for 2 hr in air atmosphere. The reference spectrum [144] is obtained from a crystalline C12A7 bulk which was prepared through a melt-solidification process at  $1500\text{ }^{\circ}\text{C}$  in a dry oxygen atmosphere.

The result of the Raman spectroscopy of the film is in accordance with the FTIR analysis. Both spectra confirm the formation of C12A7 after a heat

treatment at 1300 °C under air atmosphere. The high-intensity band at  $\sim 520 \text{ cm}^{-1}$  and medium-intensity band at  $\sim 779 \text{ cm}^{-1}$  are exclusively characteristic of C12A7 phase.

A summary of the observed Raman and FTIR absorption bands of the C12A7 thin films along with the possible vibrational modes and the origin of these vibrations are given in table 5.5.

**Table 5.5 Raman and FTIR peak positions for C12A7 thin films. The related symmetry and origin of the peaks [26] are also included.**

<i>Absorption band position (<math>\text{cm}^{-1}</math>)</i>	<i>Symmetry</i>	<i>Origin</i>	<i>Observed in</i>
224	$A_1(+E?)$	Framework Ca	Raman
312	$A_1+F_2$	Framework O	Raman
326	E	Framework O	Raman
465	$F_2$	?	FTIR
517	$A_1$	Framework Al and O	Raman
585	$F_2$	Framework Al and O	Raman + FTIR
631		Extra-framework O	Raman
779	$A_1(+F_2?)$	Framework Al and O	Raman + FTIR
848	$(A_1+F_2?)$	Framework Al and O	Raman + FTIR
879	$A_1$	Framework O	Raman
982	$F_2$	?	FTIR

The symmetries determined for each vibrational frequency (table 5.5) can be represented via the following relation suggested for the total number of vibrational modes for C12A7 framework [144]:

$$\Gamma_v^{\text{opt}} = 6A_1(\text{Raman}) + 7A_2 + 13E(\text{Raman}) + 22F_1 + 22F_2(\text{IR, Raman}) \quad (5.1)$$

Among these vibration modes,  $A_1$ ,  $E$  and  $F_2$  are Raman active and only  $F_2$  is IR active. Since the number of Raman-sensitive vibrational modes in C12A7 framework is higher than the FTIR-sensitive modes, more information can be obtained from the Raman spectrum of this compound compared to FTIR spectrum [144].

It is to be noted that due to the limitations of the FTIR-ATR equipment, the IR spectrum was only obtained down to a wavenumber of  $400 \text{ cm}^{-1}$  and therefore, it was not possible to compare the peaks of Raman spectroscopy to the ones of FTIR spectrum at relatively low frequencies. The lower-energy absorption peaks (below  $400 \text{ cm}^{-1}$ ) are mainly attributed to the vibrational modes of Ca and O atoms at the cage wall [26].

The symmetry of the vibrational modes at  $224$ ,  $779$  and  $848 \text{ cm}^{-1}$  along with the main origin of IR bands at  $465$  and  $982 \text{ cm}^{-1}$  are not assuredly determined. According to Kajihara et al, the absorption peaks at  $779$  and  $848 \text{ cm}^{-1}$  belong to the fully symmetrical mode of  $A_1$  [26]. However, the appearance of this peak in the FTIR spectrum of the film shows that  $F_2$  symmetry might also exist for these types of vibrations.

In general, the high-intensity Raman absorption peaks at  $\sim 520$  and  $780 \text{ cm}^{-1}$  and high-intensity FTIR peaks at  $\sim 465$  and  $848 \text{ cm}^{-1}$  [136] are the most characteristic features of C12A7 vibrational behaviour .

It is worth mentioning that the type of extra-framework species occupying the cages in the C12A7 framework can have a significant effect on the peak positions. The vibrational behaviour of the atoms at the cage wall is affected by



the presence of the species occupying the cage, the extent of which depends on the radius, mass and charge of the occupying species as well as the nature and the crystallographic position of the vibrating atom at the cage wall. For instance, it has been reported that upon the substitution of the extra-framework  $^{16}\text{O}$  atom with  $^{18}\text{O}$ , the Raman absorption bands of the material can shift as much as  $50\text{ cm}^{-1}$  [26].

# Chapter 6

## Optical absorption properties of C12A7 thin films

### 6.1 Optical properties at room temperature

#### 6.1.1 Optical absorption and its relationship with transmittance and reflectance

The optical absorption spectrum of a C12A7 thin film in the wavelength range of 200 – 900 nm is depicted in figure 6.1.

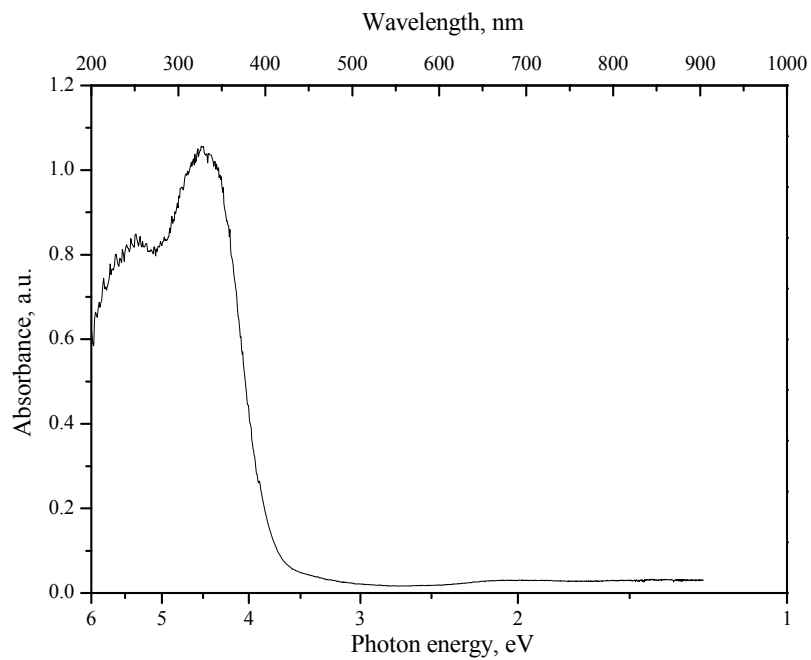


Figure 6.1 Absorbance spectrum of C12A7 thin film

As shown in the above figure, no absorption peak is observed in the visible wavelength range. However, two absorption peaks appeared in the ultraviolet region. These peaks belong to the electronic transitions attributed to the presence of extra-framework  $O^{2-}$  species in the structure of the material [13]. It has been mentioned previously (section 2.2) that a conduction band associated with the s-like states of the empty cages is formed in C12A7 in addition to the framework conduction band (FCB). This band is known as the cage conduction band (CCB). Since the extra-framework  $O^{2-}$  ions are located in a position which is displaced from the centre of the occupied cage, an empty electronic state is formed inside the same cage so called as the *perturbed* cage conduction band (shown schematically in figure 6.2). Therefore, an electronic transition is expected to occur from the occupied electronic state of  $O^{2-}$  ion to the cage conduction band.

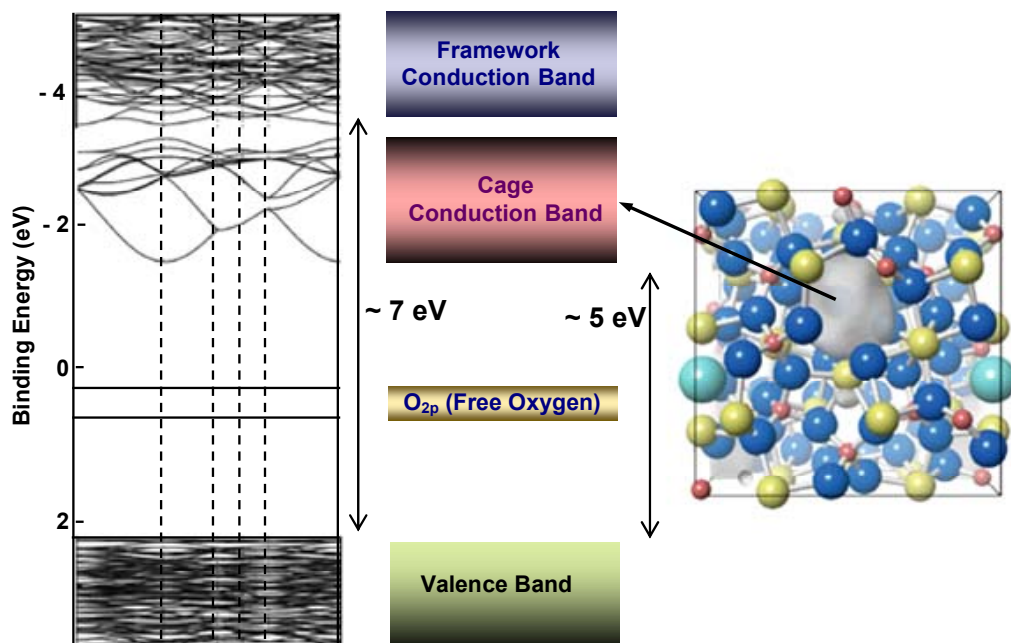


Figure 6.2 Band structure of C12A7 [50]

Such a transition is unlikely to occur in the case of occupation with other ionic species (except for electrons in conductive C12A7). The excitation energy for this type of transition has been calculated to be in the range of 3.6-4.4 eV [15]. The second transition in the range of 4.6-5.6 eV is attributed to the excitation from the occupied state of  $O^{2-}$  to the framework conduction band [57]. It is believed that the two absorption peaks observed for C12A7 films in the ultraviolet region are due to the excitation of  $O^{2-}$  ions trapped inside the structure of C12A7: $O^{2-}$ . The energy values of these electronic transitions were evaluated from the absorbance spectrum to be 4.5 and 5.39 eV for  $O^{2-} \rightarrow$ CCB and  $O^{2-} \rightarrow$ FCB transitions respectively.

It is to be noted that the absorption percentage is defined as the fraction of light which is neither transmitted nor reflected from the sample. Therefore, it can be quite different from the absorbance measured in arbitrary units (figure 6.1).

The percentage of absorption can be calculated from the measured values of transmittance (T) and reflectance (R) according to the following relation [154]:

$$\% \text{ Absorption} = 100 \% - \% R - \% T \quad (6.1)$$

Figure 6.3 shows the optical properties of C12A7 thin film in terms of the percentages of reflectance (% R), transmittance (% T) and absorption (% A).

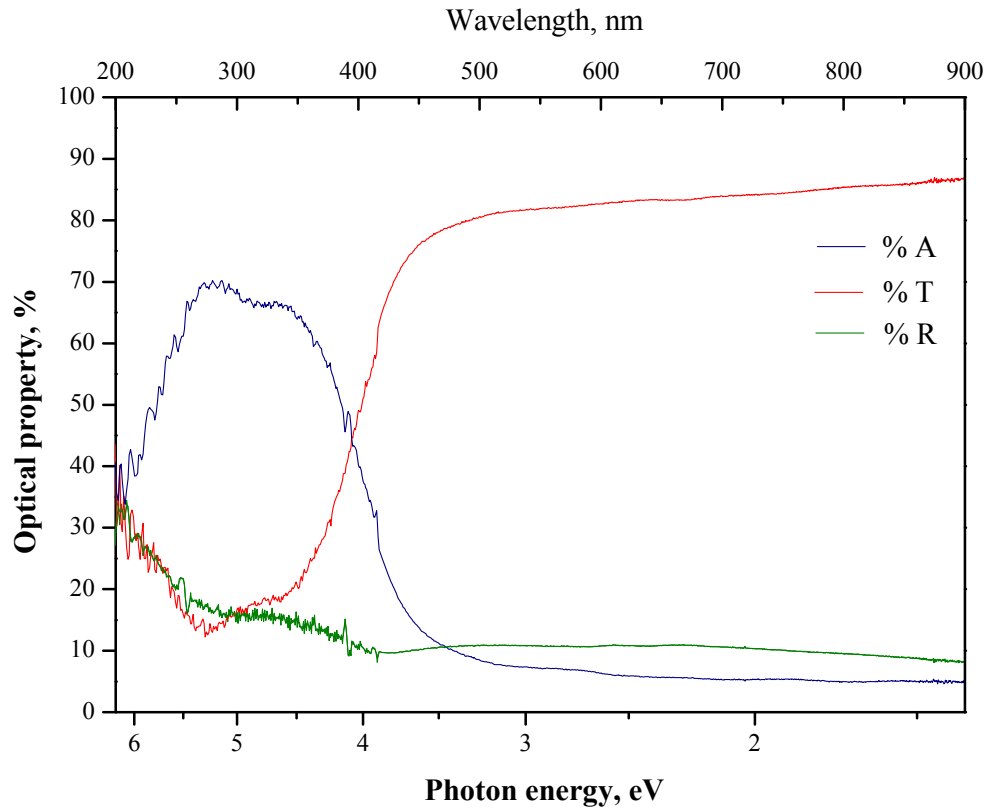


Figure 6.3 UV-visible optical properties of C12A7 thin film

### 6.1.2 Determination of the refractive index, extinction coefficient and dielectric constant

The reflectance (R) and the extinction coefficient ( $\kappa$ ) are related through the following equation [155]:

$$R = \frac{(n-1)^2 + \kappa^2}{(n+1)^2 + \kappa^2} \quad (6.2)$$

where  $n$  is the refractive index of the material. The extinction coefficient at a certain wavelength can be expressed by [156]:

$$\kappa = \frac{\alpha\lambda}{4\pi} \quad (6.3)$$

where  $\alpha$  is the absorption coefficient and  $\lambda$  is the wavelength of the incident light.

The values of  $\kappa$  and  $n$  can be determined from the reflectance and transmittance measurements using the above relations. These values were plotted in figure 6.4 as a function of wavelength.

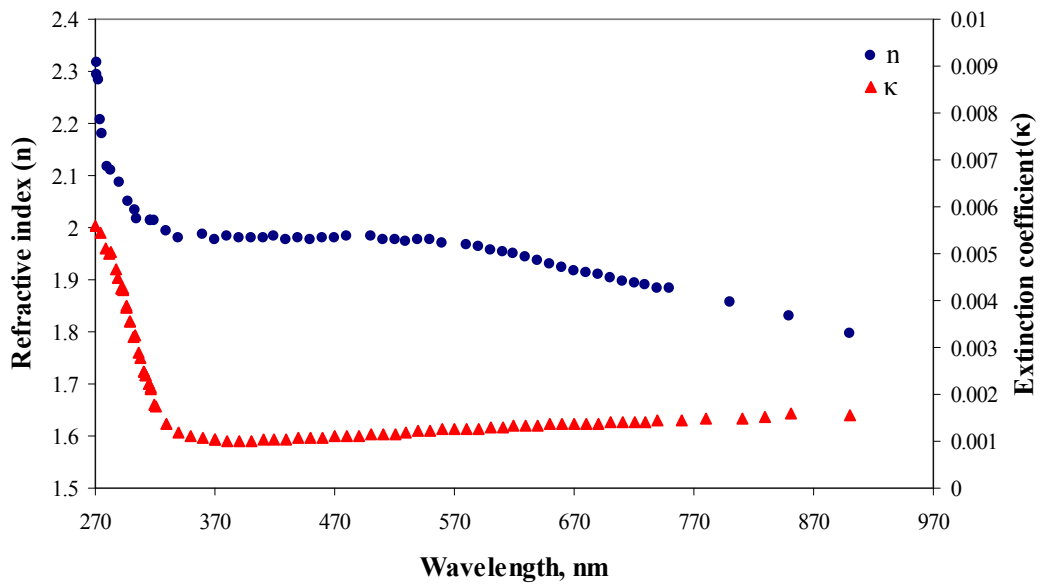


**Figure 6.4** Calculated values of refractive index and extinction coefficient as functions of wavelength for C12A7 thin film

The complex dielectric constant of the material is expressed by [156]:

$$\varepsilon^* = \varepsilon_r + i\varepsilon_i \quad (6.4)$$

where  $\varepsilon_r$  and  $\varepsilon_i$  are the real and imaginary parts of the complex dielectric constant respectively. These two parameters are related to the extinction coefficient and the refractive index according to the following equations [156]:

$$\varepsilon_r = n^2 - \kappa^2 \quad (6.5)$$

and

$$\varepsilon_i = 2n\kappa \quad (6.6)$$

Once the values of the refractive index and extinction coefficient are known, the complex dielectric constant of the material can be easily obtained using equations 6.5 and 6.6. Figure 6.5 shows the real and imaginary parts of the complex dielectric constant versus wavelength which were calculated using the above equations.

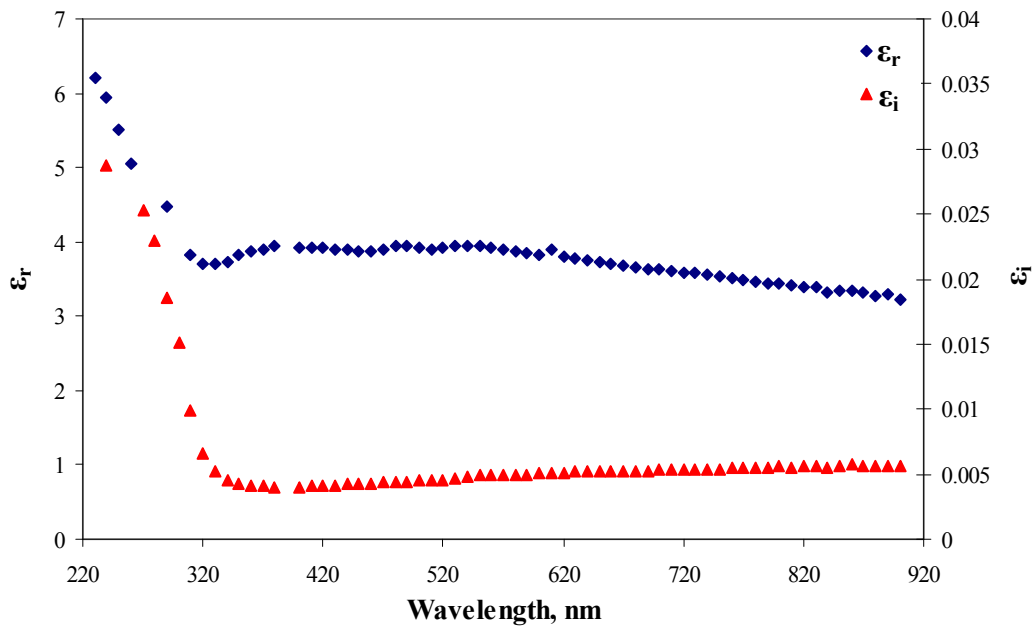


**Figure 6.5 Real and imaginary parts of the complex dielectric constant as functions of wavelength for C12A7 thin film**

For photon energies less than the band gap energy, the variation of the refractive index as a function of photon energy can be fitted into a straight line according to the first approximation of the Cauchy-Sellmair equation [157]:

$$n(h\nu) = n_0 + a_1(h\nu)^2 \quad (6.7)$$

where  $h\nu$  is the photon energy in eV,  $n_0$  is the long-wavelength limit ( $h\nu = 0$ ) of the refractive index and  $a_1$  is a constant. This relation shows that the plot of  $n$

against  $(h\nu)^2$  below the band gap energy, should give a straight line with the slope of  $a_1$  and intercept of  $n_0$ . The plot of the refractive index as a function of  $(h\nu)^2$  is depicted in figure 6.6. The inset shows a straight line which was fitted to the data in the wavelength range below the band gap energy.

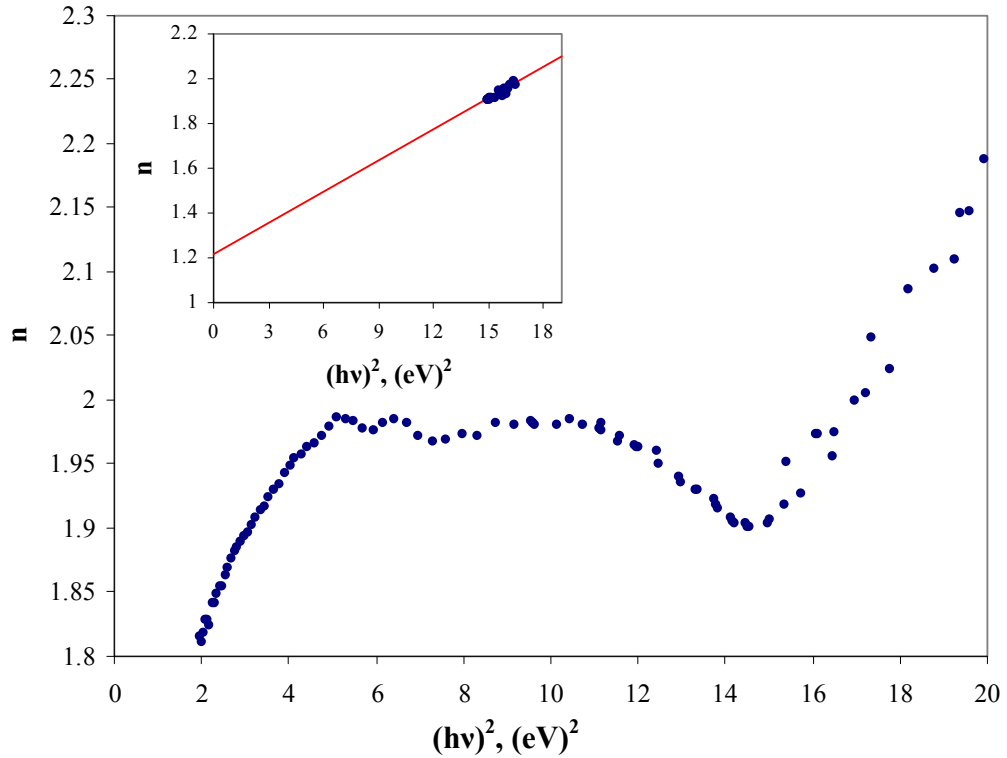


**Figure 6.6 Refractive index of C12A7 thin film as a function of the square of the photon energy. The inset shows the values of the refractive index below the band gap energy and the fitted straight line.**

The refractive index dispersion of the thin films was also studied below the absorption edge in order to check the validity of the single-effective oscillator model. The following equation has been introduced for the real part of the dielectric constant:



$$\epsilon_r = 1 + \frac{F}{E_s^2 - (h\nu)^2} \quad (6.8)$$

where  $E_s$  (also known as single-effective oscillator energy) and  $F$  are two parameters related to the electric dipole strength and the corresponding transition frequencies of the oscillators. The dispersion energy,  $E_d$ , has been introduced by Wemple and Di Domenico in the form [158]:

$$E_d = \frac{F}{E_s} \quad (6.9)$$

Now combining the equations 6.5, 6.8, and 6.9 will give the following relation between the square of the refractive index and the square of the photon energy [158]:

$$n^2 = 1 + \frac{E_d E_s}{E_s^2 - (h\nu)^2} \quad (6.10)$$

This formula is only valid in the transparent region where the value of the extinction coefficient is negligible. The plot of  $(n^2 - 1)^{-1}$  as a function of  $(h\nu)^2$  should give a straight line from which the values of  $E_s$  and  $E_d$  can be determined. This plot is depicted in figure 6.7 for C12A7 thin films. The inset shows the straight line fitted to the actual data below the absorption edge in the transparent region.

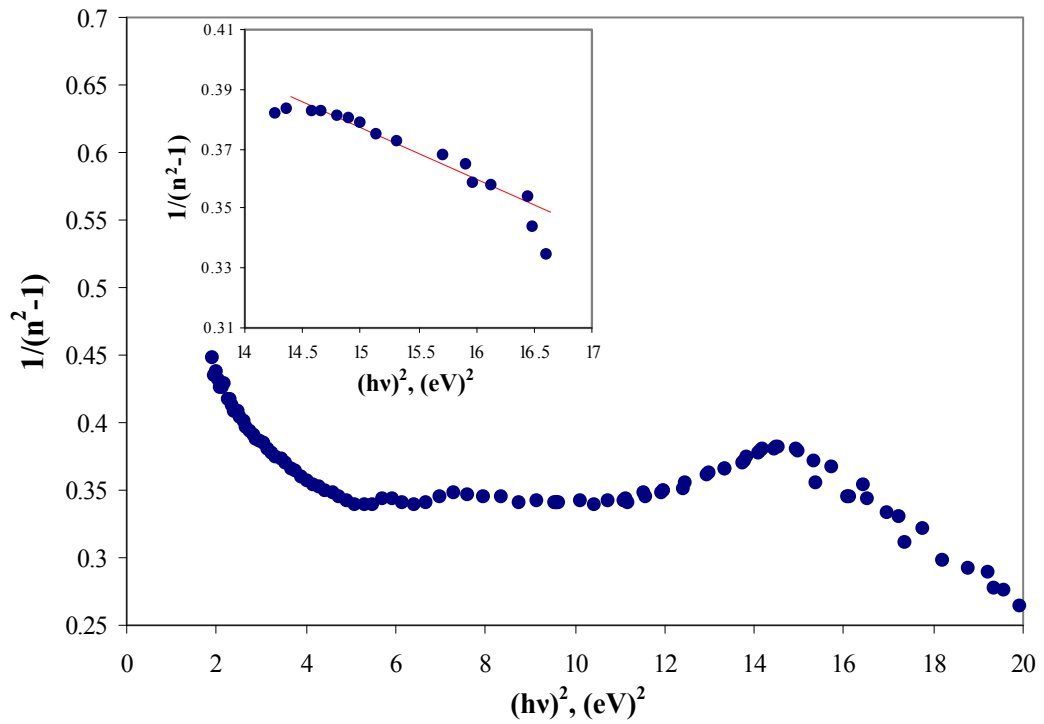


**Figure 6.7** Plot of  $1/(n^2-1) - (hv)^2$  for C12A7 thin film. The inset shows a linear relationship below the absorption edge of the material.

The values of the parameters introduced in the single-effective oscillator and Cauchy-Sellmair models are given in table 6.1.

**Table 6.1** Calculated values of the single-effective oscillator and Cauchy-Sellmair model parameters

<i>Model</i>	<i>Parameter</i>	<i>Calculated value</i>
<i>Single-effective oscillator</i>	$E_d$	9.609eV
	$E_s$	6.086eV
<i>Cauchy-Sellmair</i>	$n_o$	1.278
	$a_1$	0.0463 (eV) <sup>-2</sup>
	$n_o$	1.22

### 6.1.3 Absorption coefficient and Tauc's law

If the reflection is completely neglected, the relation between the transmittance (T) and the absorption coefficient ( $\alpha$ ) can be expressed as follows [159]:

$$\alpha = \frac{1}{d} \ln \frac{1}{T} \quad (6.11)$$

where d is the thickness of the film.

The absorption coefficient of the material can also be related to the absorbance according to the following formula [160, 161]:

$$\alpha = \frac{2.303}{d} \log \left( \frac{I_0}{I} \right) = 2.303 \frac{A}{d} \quad (6.12)$$

where A is the absorbance, d is the film thickness, and  $I_0$  and I are the intensities of the incident and transmitted light respectively.

If the reflection from the surface of the sample is to be considered, the relationship between the transmittance, absorption coefficient and reflectance of a material can be expressed by the following equation [162]:

$$T = \frac{(1-R)^2}{1-R^2} \exp(-\alpha d) \quad (6.13)$$

Near the optical band gap energy of the material where  $\alpha d$  is large, the above relation can be simplified into the following equation [126, 159, 163]:

$$\alpha = \frac{1}{d} \ln \frac{(1-R)^2}{T} \quad (6.14)$$

As mentioned earlier (section 2.4.1), the absorption coefficient of the material above the threshold of the absorption edge follows Tauc's law [164]:

$$\alpha(h\nu) = \frac{B}{h\nu} (h\nu - E_g)^r \quad (6.15)$$

where  $\alpha$  is the absorption coefficient,  $h\nu$  is the photon energy in eV,  $B$  is a constant,  $E_g$  is the energy band gap of the material and  $r$  is a constant that can take one of the four values of  $1/2$ ,  $3/2$ ,  $2$  and  $3$  depending on the type of the electronic transition responsible for the absorption [165]. In order to determine the nature of the transition and evaluate the band gap energy, the value of  $r$  must be determined.

The second derivative of the absorption coefficient with respect to  $h\nu$  for a direct transition, i.e. when  $r = \frac{1}{2}$ , gives the following expression:

$$\frac{d^2\alpha_{\text{direct}}}{d(h\nu)^2} = B \times \frac{3(h\nu)^2 - 12E_g(h\nu) + 8E_g^2}{4(h\nu)^3(h\nu - E_g)^{\frac{3}{2}}} \quad (6.16)$$

Assuming that the band gap energy lies somewhere in the range of  $\sim 3.5 - 4.5$  eV (roughly estimated from the plot of absorbance, figure 6.1), the above relation was found to be negative in Tauc region.

As for an indirect transition with  $r = 2$ , the second derivative of the absorption coefficient is expressed as follows:

$$\frac{d^2\alpha_{\text{indirect}}}{d(h\nu)^2} = B \times \frac{2E_g^2}{(h\nu)^3} \quad (6.17)$$

which gives positive values. Therefore, the nature of the electronic transition and the value of  $r$  can be determined by verifying the second derivative values of the absorption coefficient [166]. It is to be noted that both the above relations are only valid for photon energy ranges higher than the band gap energy, where

the absorption coefficient as a function of photon energy can be expressed by Tauc's formula.

The second derivative of the absorption coefficient with respect to photon energy in Tauc region is plotted in figure 6.8.

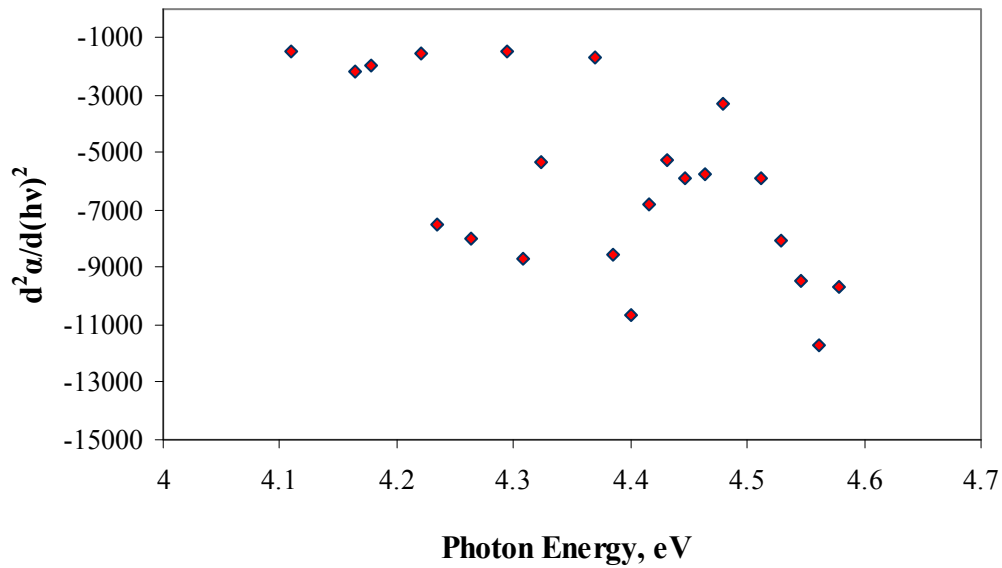


**Figure 6.8 Plot of the second derivative of the absorption coefficient with respect to photon energy in Tauc region**

Considering the negative values obtained for the second derivative of  $\alpha$ , it was concluded that the electronic transition of C12A7 responsible for absorption has a direct nature. A comparison between the plots of  $(\alpha h\nu)^{1/r}$  versus photon energy for all possible values of  $r$  also confirmed that the  $(\alpha h\nu)^2 - h\nu$  plot gives the best linear relation in the Tauc region. This plot is given in figure 6.9.

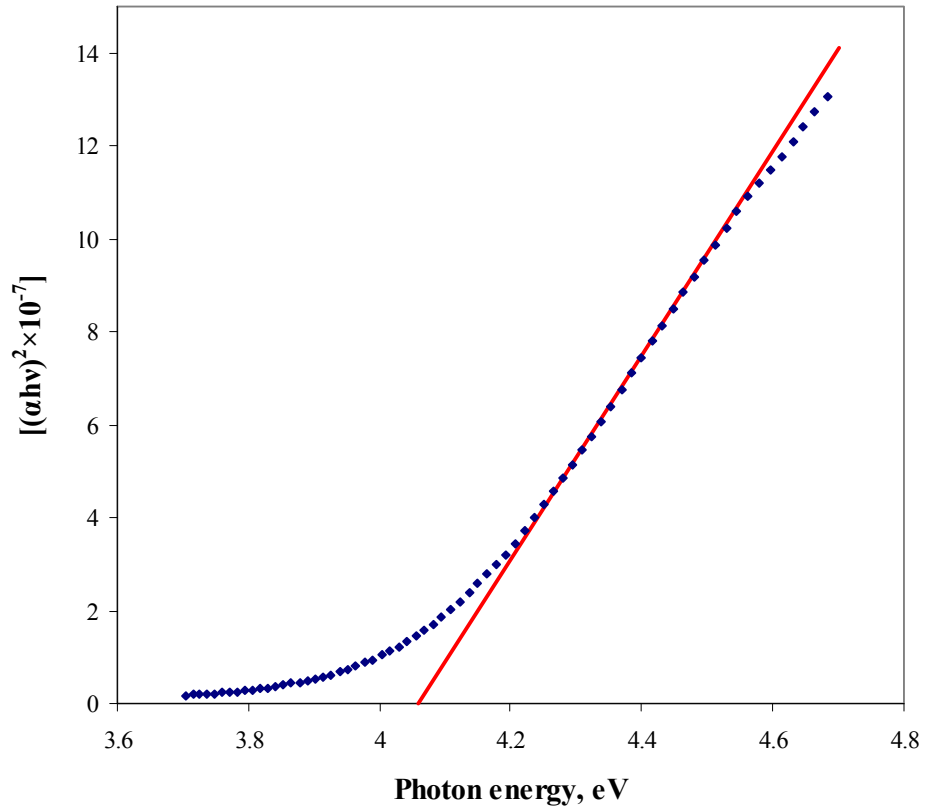


**Figure 6.9**  $(\alpha h\nu)^{1/r}$  plot versus  $h\nu$  for  $r = 0.5$ . The plot shows a linear relationship in the photon energy range of  $\sim 4.2$  to  $4.6$  eV.

An extrapolation of the above plot in the linear region gives the band gap energy of the material. The band gap was also estimated from the absorbance spectrum and compared to the value obtained from Tauc's law (the plot of figure 6.9). These values are given in table 6.2 along with the absorption edge and  $r$ .

**Table 6.2** Values of band gap energy obtained from the optical absorption spectrum and tauc's law

$r$	Absorption edge	Band gap energy obtained from $E_g = \frac{hc}{\lambda_g}$	Band gap energy based on Tauc's formula
0.5	327 nm	3.8 eV	4.088 eV

The value of  $r = 0.5$  identifies the nature of the excitation to be an allowed direct type of transition [53, 90]. The absorption edge of C12A7 framework has been reported to be  $\sim 6.8$  eV corresponding to the fundamental absorption of the material. However, the presence of extra-framework species has a significant effect on the absorption edge. The absorption edge shifts to lower values as a result of transition from an occupied state of the species to the framework conduction band. The transitions from the occupied states to the cage conduction band have much lower intensities, and therefore, the effect of these types of transitions on the absorption band shift is negligible. The extra-framework  $O^{2-}$  ions have the most significant effect on the absorption edge shift among all types of extra-framework species [57]. The absorption edge evaluated from the absorbance spectrum (figure 6.1) is  $\sim 3.8$  eV which is in the range of absorption edge reported for  $O^{2-}$ -incorporated C12A7 ( $\sim 3.75 - 4.3$  eV). The linearity of the  $(\alpha h\nu)^2 - h\nu$  plot is limited due to the presence of Urbach tail.

#### 6.1.4 Absorption tail and Urbach's law

According to Urbach [54] and Martienssen [167], in the energies lower than the band gap energy, the absorption coefficient shows a tail which can be expressed by an exponential equation as follows:

$$\alpha = \alpha_0 \exp\left(\frac{h\nu - E_0}{E_U}\right) \quad (6.18)$$

where  $\alpha_0$  and  $E_0$  are constants and  $E_U$  is the Urbach energy of the material.  $E_0$  nearly corresponds to the energy of the lowest free exciton state at zero lattice temperature. This type of exponential variation with photon energy is also known as Urbach-Martienssen tail [159].

The exponential absorption edge seems to be a fundamental optical property of many ionic and covalent materials in both crystalline and amorphous states [168, 169]. A high value of Urbach energy is mostly found with amorphous or partially crystalline materials [159]. It has been shown that the width of the absorption edge in crystalline semiconductors is proportional to thermal and structural disorder factors,  $\langle U^2 \rangle_T$  and  $\langle U^2 \rangle_x$ , i.e. the mean square displacements of the atoms from their original positions due to thermal or structural disorder respectively [56, 169].

Various mechanisms have been suggested in order to explain such behaviour. Among the proposed theories, the effect of the momentary localisation of the excitons in the randomly fluctuating field of optical phonons and ionization of the excitons' electric fields are the most accepted phenomena [159, 169]. According to a model proposed by Toyozawa et al. [170], the influence of phonon fields on the centre-of-mass motion of the excitons (i.e. momentary self-trapping of excitons) is responsible for the Urbach behaviour of the material.

According to Urbach's formula, the  $\ln \alpha - h\nu$  plot should exhibit a linear relationship below the absorption edge. This plot is depicted in figure 6.10 for C12A7 thin film.



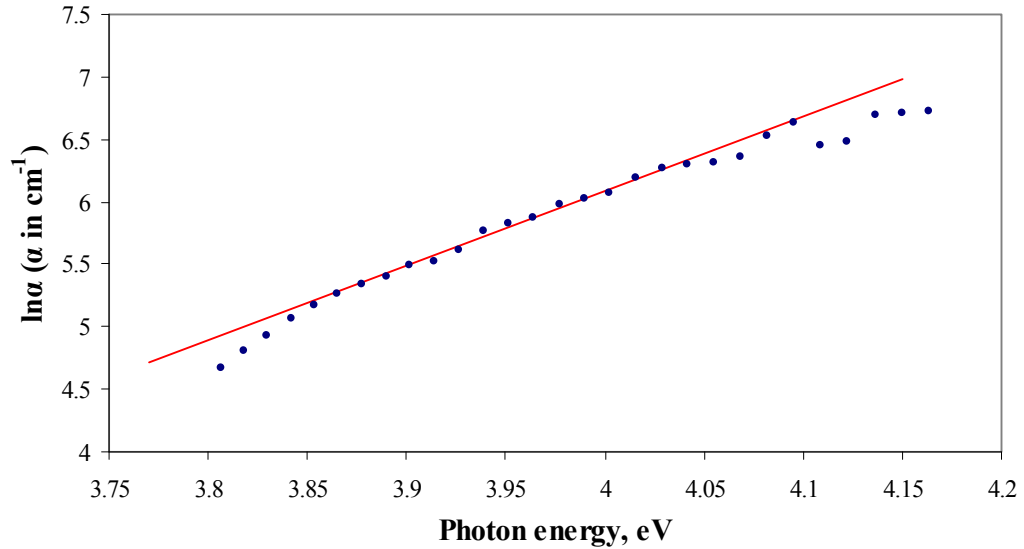


**Figure 6.10** Semi-logarithmic plot of the absorption coefficient as a function of photon energy for C12A7 thin film

As can be seen from the plot, the data follows the Urbach's rule up to a photon energy of  $\sim 4.09$  eV from which it starts deviating from the straight line. The value of Urbach energy was calculated from the slope of the line to be 0.1781 eV. The Urbach tail in C12A7 is attributed to the structural disorder at lower temperatures, while thermal disorder dominates at temperatures higher than  $\sim 100$  °C [15]. A detailed study of the Urbach tail dependency upon temperature will be explained in section 6.2.2.

## **6.2 Absorption properties at high temperatures**

### **6.2.1 Variation of the absorption coefficient with temperature**

The study of the optical absorption near the band edge and its dependency upon temperature can provide information on the electron/exciton-phonon interactions of the material [159, 165].

The absorption edge generally shifts towards lower photon energies with the increase in temperature. This type of behaviour is attributed to the change in the relative positions of the valence and conduction bands as a result of the temperature dilation of the lattice and the electron-phonon interactions being dependent upon temperature [165].

As mentioned in the previous section, the tail of the absorption edge can be determined from the exponential dependence of the absorption coefficient on photon energy according to Urbach's formula. If the tails of the absorption edge at different temperatures are Urbach type, the linear plots should converge to a single point with coordinates  $(E_0, \ln \alpha_0)$  [165]. The semi-logarithmic plots of the absorption coefficient as functions of photon energy are shown in figure 6.11 for a temperature range of 25 – 300 °C.

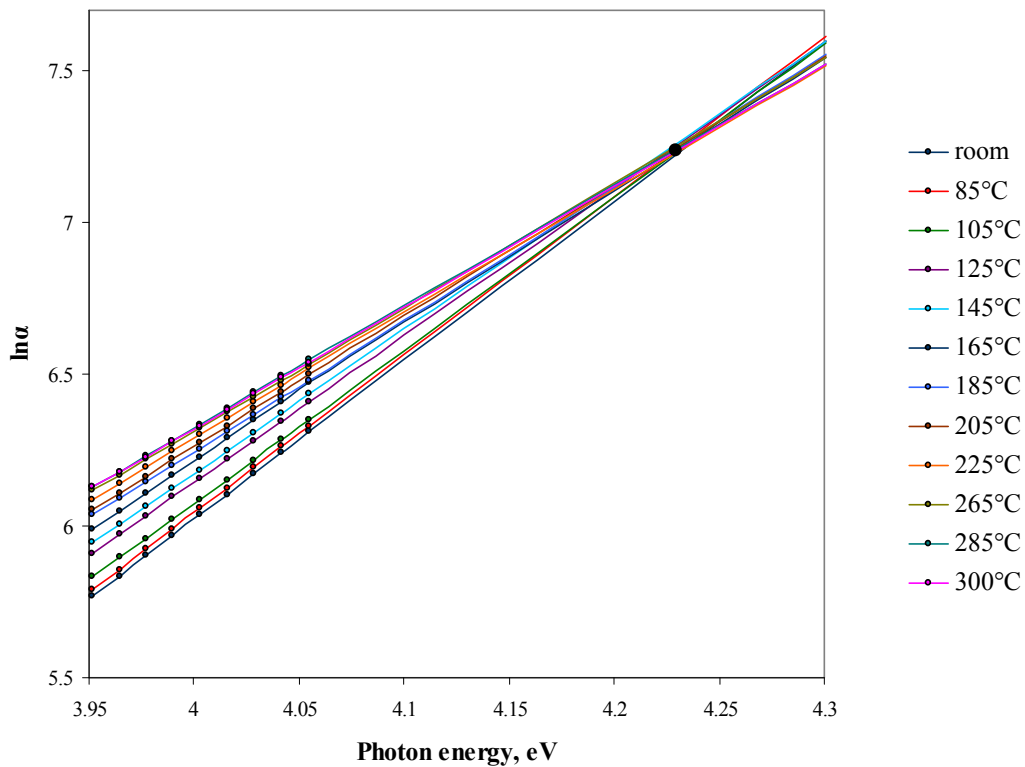


**Figure 6.11** Semi-logarithmic plots of the absorption coefficient as functions of photon energy in the Urbach region in a temperature range of 25 to 300 °C

The extrapolations of the plots converge to a single point with the coordinates  $E_0 = 4.229$  eV and  $\ln \alpha_0 = 7.24$ . Therefore, the Urbach formula for the sol-gel prepared C12A7 thin films at room temperature can be expressed as follows:

$$\alpha = 1.394 \times 10^3 \exp\left(\frac{h\nu - 4.229}{0.1911}\right) \quad (6.19)$$

in which the value of 0.1911 eV for the Urbach energy was determined from the slope of the plot at room temperature (as explained in section 6.1.4).

### 6.2.2 Variation of the Urbach energy with temperature

The Urbach energy is a function of temperature and the structural disorder of the material as well as material-dependent parameters such as phonon energy ( $h\nu_0$ ). Therefore, for the same material which is prepared using different chemical methods, the value of Urbach energy can differ [159, 171]. The temperature dependency of the Urbach tail is associated with the phonon-exciton interactions [171].

According to Cody et al, the contribution of temperature and structural disorder on the Urbach energy is expressed by the following relation [172]:

$$E_U = \frac{h\nu_0}{2\sigma_0} \left[ \coth\left(\frac{h\nu_0}{2kT}\right) + X \right] \quad (6.20)$$

where  $\sigma_0$  is an Urbach parameter depending on the ionicity of the material,  $h\nu_0$  is the average phonon energy contributing to the Urbach tail,  $\nu_0$  is the effective phonon frequency and T is the temperature in K [159, 169, 171]. This formula is a modified version of the Urbach and Martienssen models in

which  $X = 0$ .  $X$  is a measure of the degree of the structural disorder of the material and is defined by the following relation [159, 169]:

$$X = \frac{\langle U_x^2 \rangle}{\langle U^2 \rangle_0} \quad (6.21)$$

where  $\langle U_x^2 \rangle$  is the mean square deviation of the atomic positions caused by the actual structural disorder and  $\langle U^2 \rangle_0$  is the zero-point uncertainty in the atomic positions [159]. The structural disorder can be caused by intrinsic defects such as vacancies or dislocation, or extrinsic factors such as radiation and/or doping [159, 171]

According to Cody's studies, the thermal and structural disorders are additive and the Urbach energy can be expressed as the sum of two terms, one being temperature dependent and one being temperature independent [159, 169]:

$$E_U(X, T) = E_U(X) + E_U(T) \quad (6.22)$$

Cody et al. have proposed a formula which indicates the contribution of these two terms in the form [172]:

$$E_U(X, T) = \frac{k\Theta_E}{\sigma_0} \left[ \frac{X+1}{2} + \frac{1}{\exp(\Theta_E/T) - 1} \right] \quad (6.23)$$

where  $\Theta_E$  (also known as Einstein temperature [61]) is the average temperature of the interacting phonons representing the Einstein model for solids [159]. It could be assumed that the Debye phonon spectrum with temperature  $\Theta_D$  is responsible for an Einstein oscillator with a temperature of  $\Theta_E$ . The former temperature can be related to the latter according to following expression:

$$\Theta_D = \sqrt[3]{\frac{6}{\pi}} \Theta_E \quad (6.24)$$

The Debye temperature was calculated to be 471.5 K for C12A7 films. An alternative relation has been suggested by Yang et al. in the form [173]:

$$E_U(X, T) = A \left[ \frac{1}{\exp(\Theta_E / T) - 1} \right] + B \quad (6.25)$$

in which the first term is temperature dependent and represents the exciton-phonon interaction and the second term is due to the mean-square deviation of the atomic positions of a perfectly ordered lattice caused by structural disorder [159].

The value of Urbach energy as a function of temperature along with the fitted curves of Cody and Yang models are depicted in figure 6.12.

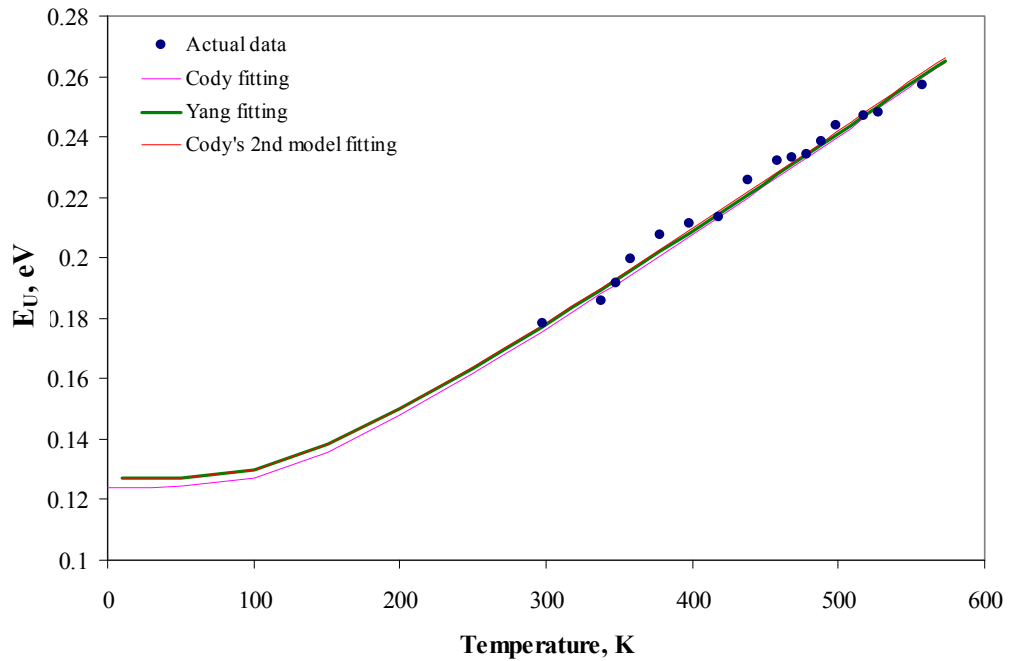


**Figure 6.12 Temperature dependency of the Urbach energy and the fitted models proposed by Cody and Yang. The first model by Cody represents the dependency of the Urbach energy on the phonon energy (equation 6.20) while the second model is based on the Einstein temperature (equation 6.23).**

The unknown parameters of the Urbach, Cody and Yang's models were determined by fitting the formulas to the actual data. These values are presented in table 6.3.

**Table 6.3 Fitting parameters of the Urbach energy-temperature models proposed by Urbach, Cody and Yang**

<i>Parameter</i>	<i>Fitted value</i>	<i>Model</i>
$h\nu_0$ (eV)	0.083	Urbach
	0.032	Cody
$\sigma_0$	0.228	Urbach
	0.25	Cody
$X$	0	Urbach
	0.94	Cody
$\Theta_E$ (K)	380	Cody
$A$ (eV)	0.13	Yang
$B$	0.127	Yang

The difference between the values of the fitting parameters obtained from Urbach and Cody's models comes from the fact that the effect of the structural disorder is not considered in the Urbach formula [159]. The fitted line of the Cody's formula is best described with the phonon energy of 32 meV which is equivalent to the Raman band of  $258\text{ cm}^{-1}$  [26]. This Raman band is associated with the vibration modes of the framework  $\text{Ca}^{2+}$  ions and has been reported to be responsible for the occurrence of Urbach tail in C12A7 [15]. Since the values of Urbach energy were obtained at room temperature and higher, the effect of

structural disorder cannot be neglected. Therefore, the parameters obtained from Cody's model will be used from now on for more accuracy.

### 6.2.3 Variation of the steepness parameter with temperature

The steepness parameter,  $\sigma$ , is proportional to the slope of the straight line in the semi-logarithmic absorption coefficient plot. This parameter can be determined using Urbach's formula given by [15]:

$$\sigma = \frac{kT}{E_U} \quad (6.26)$$

where  $k$  is the Boltzmann constant,  $T$  is the temperature in K, and  $E_U$  is the Urbach energy. According to Toyozawa's theory, which was later modified by Cody, the temperature dependence of the steepness parameter can also be expressed by the following relation [174]:

$$\sigma = \frac{2\sigma_0 kT}{h\nu_0} \tanh\left(\frac{h\nu_0}{2kT}\right) \quad (6.27)$$

where  $h\nu_0$  is the phonon energy interacting with the optical transitions. The constant  $\sigma_0$  indicates the strength of the electron-phonon interaction ( $g$ ) according to the following relationship [175]:

$$g = \frac{2}{3} \sigma_0^{-1} \quad (6.28)$$

Expanding the expression  $\tanh(h\nu_0/kT)$  in a power series of  $(h\nu_0/kT)$  using Taylor's series approximation gives:

$$\sigma = \sigma_0 \left( 1 - \frac{1}{3} \times \left( \frac{h\nu_0}{2kT} \right)^2 + \frac{2}{15} \times \left( \frac{h\nu_0}{2kT} \right)^4 - \frac{17}{315} \times \left( \frac{h\nu_0}{2kT} \right)^6 + \dots \right) \quad (6.29)$$

The value of the effective phonon frequency as well as the constant  $\sigma_0$  can be easily determined by plotting the values of  $\sigma$  against  $1/T^2$  [165]. The plot of the steepness parameter as a function of  $1/T^2$  is depicted in figure 6.13.

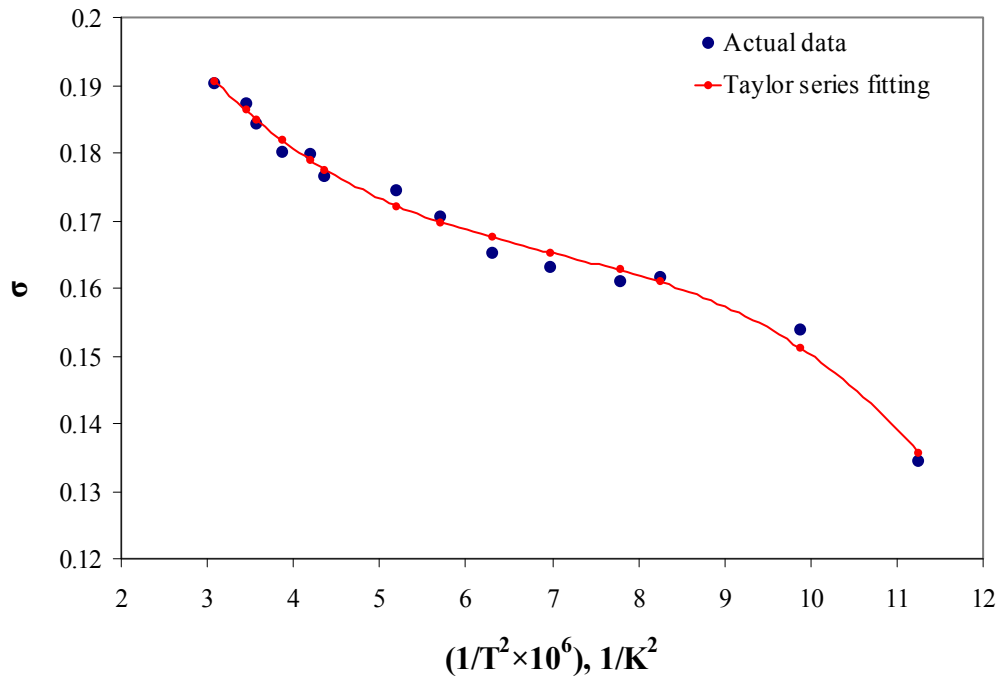


**Figure 6.13 Steepness parameter of C12A7 thin film as a function of  $T^{-2}$  and the fitted Taylor's series approximation**

The fitting parameters were found to be  $\sigma_0 = 0.23$  and  $h\nu_0 = 0.079$  eV using equation 6.29. The value of  $g$  was also calculated to be  $\sim 2.9$  using equation 6.28. Since the values of the fifth term onwards in the Taylor's series are relatively small, these terms have not been considered in the calculations. Figure 6.14 shows the temperature dependency of the steepness parameter of a C12A7



thin film along with the Urbach model fitting using the parameters obtained from equation 6.29.

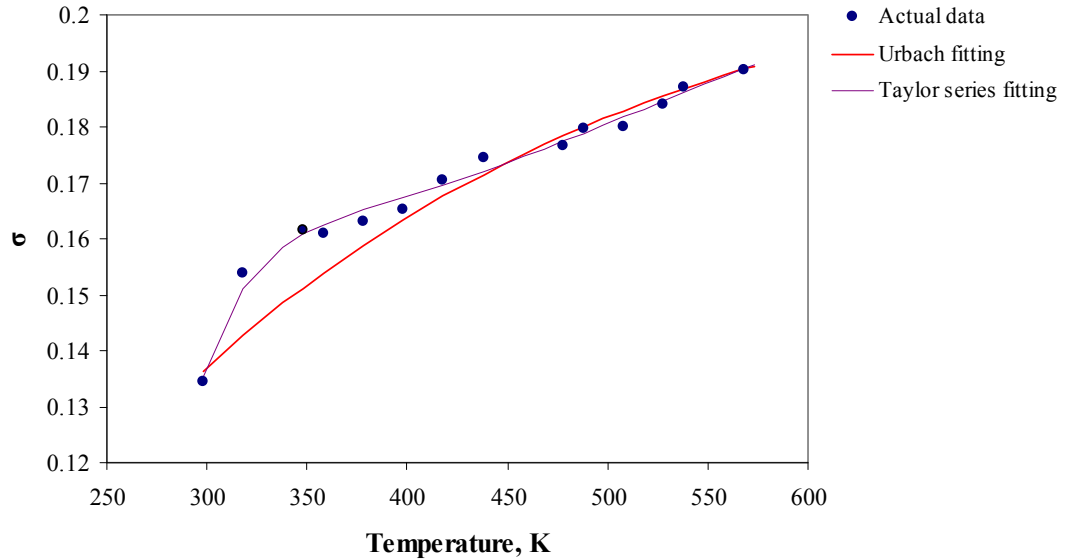


**Figure 6.14** Temperature dependency of the steepness parameter and the fitted model represented by Urbach. Taylor's series fitting is an approximation to the Urbach's model.

#### 6.2.4 Variation of the band gap energy with temperature

According to Manoogian-Woolley model, the temperature dependency of the band gap energy is expressed by the following equation [176]:

$$E_g(T) = E_g(0) - UT^S - V \frac{E_p}{k} \left( \coth \frac{E_p}{2kT} - 1 \right) \quad (6.30)$$

where  $k$  is the Boltzmann constant,  $T$  is the temperature in K, and  $E_g(0)$ ,  $U$ ,  $S$ ,  $V$  and  $E_p$  are the fitting parameters. The effects of lattice dilation and exciton-phonon interaction have been considered separately [171].

The temperature dependency of the band gap energy can also be expressed by Varshni equation as follows [177]:

$$E_{\text{eg}}(T) = E_{\text{eg}}(0) - \frac{\alpha T^2}{T + T_0} \quad (6.31)$$

where  $\alpha$  is the Varshni coefficient determined from the least squares fitting to the actual data [159].

An alternative to the above models is the Bose-Einstein model which considers the electron interaction with the phonon bath inside the crystal in order to explain the variations of the band gap with temperature [178]:

$$E_{\text{eg}}(T) = E_{\text{eg}}(0) - \frac{2a_B}{\exp\left(\frac{\Theta_E}{T}\right) - 1} \quad (6.32)$$

where  $E_g(0)$  is the band gap energy at 0 K,  $\Theta_E$  is the Einstein temperature, and  $a_B$  is a measure of the electron-phonon interaction coupling. Figure 6.15 shows the values of the band gap energy of a C12A7 thin film obtained at different temperatures along with the fitted models.

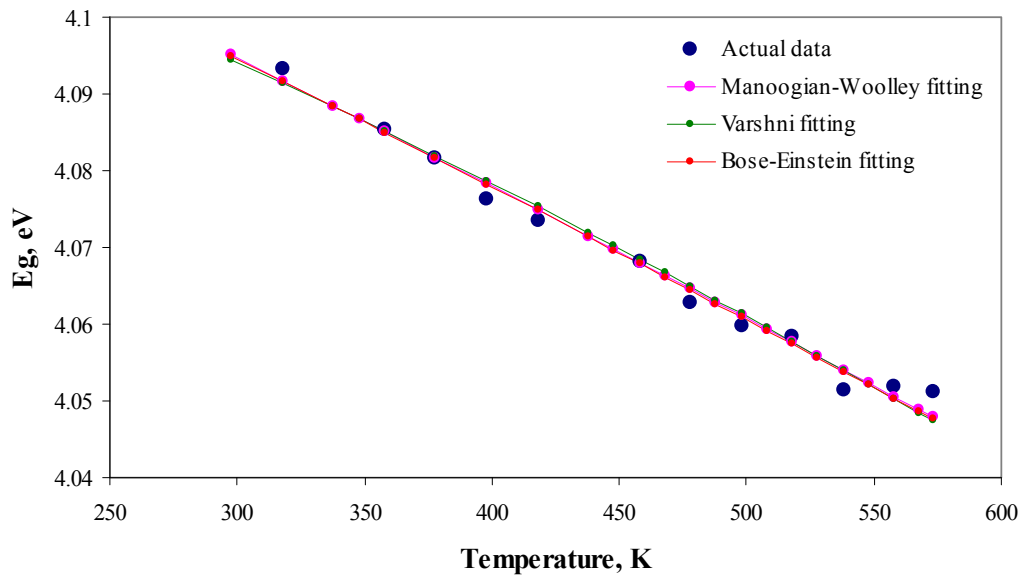


**Figure 6.15 Temperature dependency of the band gap energy and the fitted models proposed by Manoogian-Woolley, Varshni and Bose-Einstein**

The constant parameters of the models suggested by Manoogian-Woolley, Varshni, and Bose-Einstein were determined by fitting each model to the actual data (shown in figure 6.15). These values are listed in table 6.4.

**Table 6.4 Fitting parameters of the band gap energy-temperature models proposed by Manoogian-Woolley, Varshni, and Bose-Einstein**

<i>Parameter</i>	<i>Fitted value</i>	<i>Model</i>
$E_g(0)$ (eV)	4.127	Manoogian-Woolley
	4.122	Varshni
	4.122	Bose-Einstein
$U$ (eV.K <sup>-1.05</sup> )	$2.7 \times 10^{-5}$	Manoogian-Woolley
$s$	1.05	Manoogian-Woolley
$V$ (eV.K <sup>-1</sup> )	$7.1 \times 10^{-5}$	Manoogian-Woolley
$\alpha$ (T <sup>-1</sup> )	$2.32 \times 10^{-4}$	Varshni
$T_o$ (K)	450	Varshni
$a_B$	0.035	Bose-Einstein

A comparison between the parameter  $T_o = 450$  K and the Debye temperature  $\Theta_D = 417.5$  K (determined from equation 6.24) shows a close relation between the two parameters which has also been reported for other types of materials [179].

### 6.2.5 The relationship between the band gap energy and Urbach energy

According to Cody et al. the dependence of the band gap energy on Urbach energy should be linear [159]. The following equation relates the band gap energy to the Urbach energy in the form [172, 180]:

$$E_g(X, T) = E_g(0, 0) - \langle U^2 \rangle_0 D \left[ \frac{E_U(X, T)}{E_U(0, 0)} - 1 \right] \quad (6.33)$$

where  $E_g(0, 0)$  and  $E_U(0, 0)$  are the band gap energy and the Urbach energy of a defect-free crystal at 0K,  $\langle U^2 \rangle_0$  is the zero point uncertainty in atomic positions,  $D$  is the second-order deformation potential that determines the effect of temperature on the band gap energy, and  $E_g(X, T)$  and  $E_U(X, T)$  are the band gap energy and the Urbach energy of the material with finite degree of structural disorder at a fixed temperature [159, 171].

The relationship between the band gap energy and the Urbach energy of a C12A7 thin film is shown in figure 6.16 for a temperature range of 25 – 300 °C .

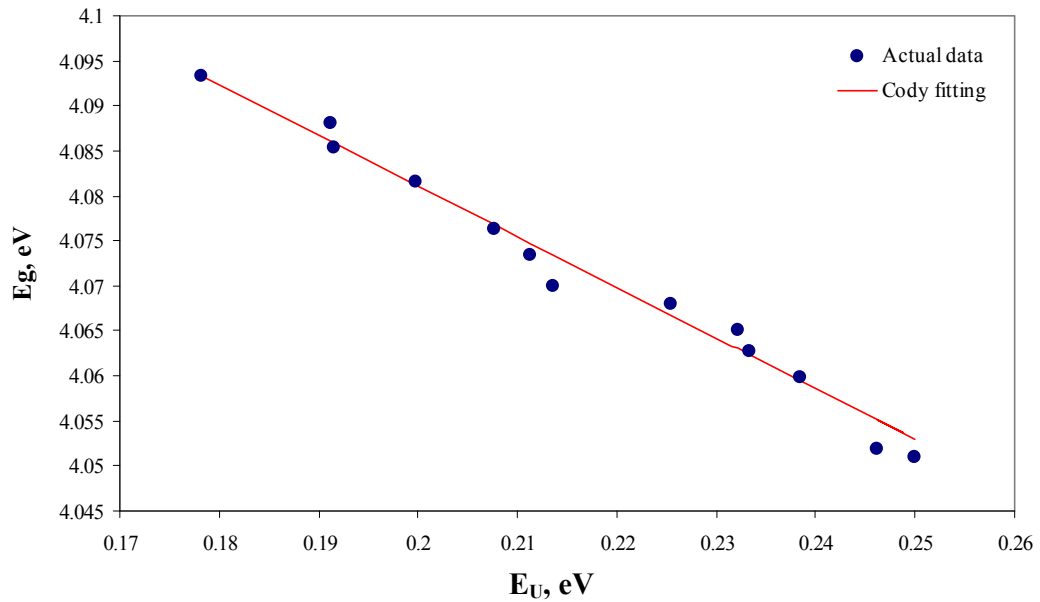


**Figure 6.16 Relationship between the band gap energy and Urbach energy obtained at different temperatures**

As can be seen from the plot, the relation nearly follows a straight line. The unknown parameters of the Cody's model were determined by fitting the formula to the actual data. These values are presented in table 6.5.  $E_U(0,0)$  can be calculated using the following formula [159]:

$$E_U(0,0) = \frac{k\Theta_E}{2\sigma_o} \quad (6.34)$$

The above equation is actually a simplified form of the Cody's formula (equation 6.23) in which the values of temperature and structural disorder constant (X) are zero.

**Table 6.5 Fitting parameters of the band gap energy-Urbach energy model proposed by Cody**

<i>Parameter</i>	<i>Fitted value</i>
$E_g(0,0)$ (eV)	4.156
$E_U(0,0)$ (meV)	65.49
$\langle U^2 \rangle_o D$ (meV)	36.5

## Chapter 7

### Conclusion and future work

The present study was set out to determine the appropriate processing parameters for the fabrication of sol-gel derived homogenous  $12\text{CaO}\cdot 7\text{Al}_2\text{O}_3$  (C12A7) films on magnesium oxide (MgO) substrates by systematic optimization.

The effect of the type and molar fraction of solvent, as well as the molar fraction of water, on the morphology and surface quality of the films was thoroughly studied and an optimum solution processing, including the appropriate types and molar fractions of the ingredients, was proposed based on the microstructural observations. The molar ratios of solvent and water with respect to the main precursors were considered as the variable solution ingredients and two alcohols, methanol and isopropyl alcohol, were chosen for solution preparation.

The effect of heat treatment temperature and duration under normal air atmosphere on the formation of C12A7 and other possible phases was investigated by means of X-ray diffraction (for powder) and FTIR-ATR and

Raman spectral analyses (for thin films), and the suitable heat treatment procedure was suggested for the fabrication of single-phase C12A7 in form of powder and films on MgO substrate.

The optical characteristics of C12A7 thin films were studied in a temperature range of 25-300 °C. The variations of the band gap energy and Urbach energy with respect to temperature were examined and compared to different theoretical models by the evaluation of the unknown parameters from fitting each model to the actual data. The theoretical relations that could best describe the variations of the band gap energy and Urbach energy with temperature, as well as the relationship between the two energies at different temperatures, were suggested for C12A7 thin films on MgO substrate.

A summary of the achievements are listed as follows:

1- The molar ratios of 10:1 for solvent to the main ingredients and 5:1 for water to aluminium sec-butoxide were found to be the optimum molar fractions in order to obtain a clear solution and high quality continuous films on MgO substrate.

2- The solution stability was increased substantially using the improved recipe and solutions with long life-times (1 to 2 months) were obtained without the need for the addition of acid.

3- The use of isopropyl alcohol as solvent improved the quality of the films compared to methanol.

4- The critical thickness of the films was increased to a few microns (up 6.5  $\mu\text{m}$ ) using the proposed solution recipe which is significantly higher than the

values reported for sol-gel processed thin films other than SiO<sub>2</sub> (typically no more than 10 nm).

5- The heat treatment of the thin film at 1100 °C, which has been previously reported in the literature [47, 135], was not high enough for the formation of C12A7 on MgO substrate under normal air atmosphere and heat treatment at this temperature even for several hours did not produce C12A7 crystals.

6- Based on FTIR and Raman spectral analyses, the heat treatment of the films at a temperature of 1300 °C for 2 hr under air atmosphere was suggested in order to fabricate single-phase C12A7 film on MgO substrate without any adverse effect on the film-substrate interaction or the surface quality of the films.

7- The phase formation temperature of C12A7 films was found to be different from powder. While the crystallization of C12A7 powder started at ~ 900 °C, there was no trace of this phase forming on MgO substrate even at a temperature as high as 1100 °C. In addition, the crystallization of C12A7 powder was accompanied by the formation of CA secondary phase which remained in the mixture even after long heat treatment durations. The thin films, however, consisted of a single-phase calcium aluminate phase with a favourable formation of C5A3 at lower temperatures and C12A7 at a higher temperature of 1300 °C.

8- The results of the FTIR spectral analysis of C12A7 films after a heat treatment in H<sub>2</sub>-N<sub>2</sub> reducing atmosphere showed a shift of the infrared absorption bands towards higher frequencies after the heat treatment in the reducing atmosphere. Since the shift of infrared peaks was not observed for the



thin films of C5A3 and C3A, it was concluded that the shift of absorption peaks is characteristic of C12A7 cage structure.

9- The optical characterization of C12A7 films showed a reduction in the band gap energy from 4.088 eV at room temperature to 4.051 eV at 300°C, while the Urbach energy increased from 0.178 eV at 25 °C to 0.257 eV at 300 °C.

10- A linear relationship was observed between the optical band gap energy and the Urbach energy at different temperatures.

The optimized sol-gel technique is found to be an elegant and economical method for the production of continuous crack-free thin films of homogeneous C12A7 phase as evident from morphological, compositional and optical studies. Therefore, an efficient post-fabrication technique can now be developed in order to produce sol-gel derived semiconductive and conductive C12A7 thin films. This will lead to the production of a new generation of thin-film-based optoelectronic devices as electron field emitters, and as transparent conductive oxide layers for solar cells and transparent transistors.

It is recommended that additional research be undertaken in the following categories:

1- The study on the effect of heat treatment under the reducing atmosphere of H<sub>2</sub>-N<sub>2</sub> on the incorporation of electrons in sol-gel derived C12A7 thin films and the insulating-to-conducting conversion of the compound.

2- Investigation on the fabrication of electrically conductive C12A7 films via heat treatment of the insulating films in presence of titanium.

3- Investigation on the possibility of fabricating conductive sol-gel derived C12A7 thin films via the deposition of a second amorphous C12A7 layer and subsequent heat treatment under vacuum.

4- Study on the effect of heat treatment under a reducing atmosphere of CO/CO<sub>2</sub> on the insulating-conducting conversion of C12A7 thin films.

## References

1. S. W. Kim, Y. Toda, K. Hayashi, M. Hirano, H. Hosono, *Chem. Mater.*, 2006, **18**, 1938-1944
2. L. Palacios, A. G. De La Torre, S. Bruque, J. L. Garcia-Munoz, S. Garcia-Granda, D. Sheptyakov, M. A. G. Aranda, *Inorg. Chem.*, 2007, **46**, 4167-4176
3. Q. Chen, K. Yoshida, H. Yamamoto, M. Uchida, M. Sadakata, *Energy Fuels*, 2007, **21**, 3264–3269
4. M. Miyakawaa, M. Hirano, T. Kamiya, H. Hosono, *Appl. Phys. Lett.*, 2007, **90**, 182105
5. C. Jing, X. Xu, J. Hou, *J. Sol-Gel Sci. Technol.*, 2007, **43**, 321–327
6. A. Douy, M. Gervais, *J. Am. Ceram. Soc.*, 2000, **83** [1], 70–76
7. S. Matsuishi, Y. Toda, M. Miyakawa, K. Hayashi, T. Kamiya, M. Hirano, I. Tanaka, H. Hosono, *Science*, 2003, **301**, 626-629
8. H. Boysen, M. Lerch, A. Stysb, A. Senyshyn, *Acta Cryst.*, 2007, **B63**, 675–682
9. H. Hosono, *Int. J. Appl. Ceram. Technol.*, 2004, **1**[2], 106-108
10. E. M. Levin, C. R. Robbins, H. F. McMurdie, *Phase Diagrams for Ceramists*, American Ceramic Society, Columbus, Ohio, 1987
11. J. A. McLeod, A. Buling, E. Z. Kurmaev, P. V. Sushko, M. Neumann, L. D. Finkelstein, S. W. Kim, H. Hosono, A. Moewes, *Phys. Rev. B: Condens. Matter*, 2012, **85**, 045204
12. Peter V. Sushko, A. L. Shluger, K. Hayashi, M. Hirano, H. Hosono, *Phys. Rev. B*, 2006, **73**, 014101

13. H. B. Bartl, T. Scheller, *Neuses Jarhrb. Minerl. Monatsh.*, 1970, 547-552
14. R. Kiyanagi, J. W. Richardson Jr., N. Sakamoto, M. Yoshimura, *Solid State Ionics*, 2008, **179**, 2365–2371
15. K. Hayashi, P. V. Sushko, D. Munoz Ramo, A. L. Shluger, S. Watauchi, I. Tanaka, S. Matsuishi, M. Hirano, H. Hosono, *J. Phys. Chem. B*, 2007, **111**, 1946-1956
16. M. Ruzsak, S. Witkowski, Z. Sojka, *Res. Chem. Intermed.*, 2007, **33**[8–9], 689–703
17. H. Yanagi, T. Kuroda, K. Kim, Y. Toda, T. Kamiya, H. Hosono, *J. Mater. Chem.*, 2012, **22**, 4278-4281
18. K. Hayashi, M. Hirano, H. Hosono, *J. Mater. Res.*, 2002, **17**[6], 1244-1247
19. A. Chatterjee, M. Nishioka, F. Mizukami, *Chem. Phys. Lett.*, 2004, **390**, 335–339
20. K. Hayashi, M. Hirano, S. Matsuishi, H. Hosono, *J. Am. Ceram. Soc.*, 2002, **124** [5], 738-739
21. A. Cuneyt Tas, *J. Am. Ceram. Soc.*, 1998, **81**[11], 2853–2863
22. P. V. Sushko, A. L. Shluger, M. Hirano, H. Hosono, *J. Am. Chem. Soc.*, 2007, **129**, 942-951
23. P. V. Sushko, A. L. Shlugera, K. Hayashib, M. Hiranob, H. Hosono, *Thin Solid Films*, 2003, **445**, 161–167
24. K. Hayashi, S. Matsuishi, T. Kamiya, M. Hirano, H. Hosono, *Nat.*, 2002, **419**, 462-465

25. S. Matsuishi, K. Hayashi, M. Hirano, I. Tanaka H. Hosono, *J. Phys. Chem. B*, 2004, **108**, 18557-18568
26. K. Kajihara, S. Matsuishi, K. Hayashi, M. Hirano, H. Hosono, *J. Phys. Chem. C*, 2007, **111**, 14855-14861
27. M. Miyakawa, H. Kamioka, M. Hirano, T. Kamiya, P. V. Sushko, A. L. Shluger, N. Matsunami, H. Hosono, *Phys. Rev. B*, 2006, **73**, 205108
28. P. Mondal, J. W. Jeffery, *Acta Cryst.*, 1975, **B31**, 689-697
29. N. Sakamoto, M. Hori, Y. Matsuyama, N. Wakiya, H. Suzuki, *J. Am. Ceram. Soc.*, 2009, **92**[S1], S189–S191
30. Sh. Yang, J. N. Kondo, K. Hayashi, M. Hirano, K. Domen, H. Hosono, *Chem. Mater.*, 2004, **16**, 104-110
31. J. Li, K. Hayashi, M. Hirano, H. Hosono, *Solid State Ionics*, 2009, **180**, 1113–1117
32. M. Lacerda A.R. West, J. T. S. Irvine, *Solid State Ionics*, 1993, **59**, 257-262
33. J. Li, F. Huang, L. Wang, Sh. Q. Yu, Y. Torimoto, M. Sadakata, Q. X. Li, *Chem. Mater.*, 2005, **17**, 2771-2774
34. H. Hosono, Y. Abe, *Inorg. Chem.*, 1987, **Vol. 26** [8], 1192-1195
35. H. Hosono, K. Hayashi, K. Kajihara, P. V. Sushko, A. L. Shluger, *Solid State Ionics*, 2009, **180**, 550–555
36. D. K. Lee, L. Kogel, S. G. Ebbinghaus, I. Valov, H. D. Wiemhoefer, M. Lerch, J. Janek, *Chem. Phys.*, 2009, **11**, 3105–3114

37. A. S. Tolkacheva, S. N. Shkerin, S. V. Plaksin, E. G. Vovkotrub, K. M. Bulanin, V. A. Kochedykov, D. P. Ordinartsev, O. I. Gyrdasova, N. G. Molchanova, *Russ. J. Appl. Chem.*, 2011, **Vol. 84 [6]**, 907-911
38. S. W. Kim, T. Shimoyama, H. Hosono, *Science*, 2011, **333**, 71-74
39. K. Hayashi, S. Matsuishi, N. Ueda, M. Hirano, H. Hosono, *Chem. Mater.*, 2003, **15**, 1851-1854
40. H. Hosono, *Sci. Technol. Adv. Mater.*, 2004, **5**, 409-416
41. H. Hosono, *Thin Solid Films*, 2007, **515**, 6000-6014
42. M. Miyakawa, K. Hayashi, M. Hirano, Y. Toda, T. Kamiya, H. Hosono, *Adv. Mater.*, 2003, **15[13]**, 1100-1103
43. E. Feldbach, V. P. Denks, M. Kirm, P. Liblik, A. Maaros, H. Mandar, T. Avarmaa, K. Kunnus, *J Mater Sci: Mater Electron*, 2009, **20**, S260-S263
44. Y. Toda, S. Matsuishi, K. Hayashi, K. Ueda, T. Kamiya, M. Hirano, H. Hosono, *Adv. Mater.*, 2004, **16[8]**, 685-689
45. Y. Nishio, K. Nomura, M. Miyakawa, K. Hayashi, H. Yanagi, T. Kamiya, M. Hirano, H. Hosono, *phys. stat. sol. (a)*, 2008, **205 [8]**, 2047-2051
46. T. Kamiya, S. Aiba, M. Miyakawa, K. Nomura, S. Matsuishi, K. Hayashi, K. Ueda, M. Hirano, H. Hosono, *Chem. Mater.*, 2005, **17[25]**, 6311-6316
47. M. Miyakawa, *J. Ceram. Soc. Jpn.*, 2009, **117[3]**, 395-401
48. S. W. Kim, R. Tarumi, H. Iwasaki, H. Ohta, M. Hirano, H. Hosono, *Phys. Rev. B: Condens. Matter*, 2009, 075201
49. H. Hosono, S. W. Kim, M. Miyakawa, S. Matsuishi, T. Kamiya, *J. Non-Cryst. Solids*, 2008, **354**, 2772-2776

50. D. S. Ginley, *Handbook of Transparent Conductors*, Springer Science + Business Media, LLC, United States of America, 2011, [1], 319
51. H.M. Ali, H.A. Mohamed, S.H. Mohamed, *Eur. Phys. J. Appl. Phys.*, 2005, **31**, 87–93
52. A. Ates, B. Gurbulak, M. Yildirim, S. Dogan, S. Duman, T. Yildirim, S. Tuzemen, *Turk. J. Phys.*, 2002, **26**, 127-131
53. M. Khalil, G. Nasr, N. El-Sawy, *J. Phys. D: Appl. Phys.*, 2006, **39**, 5305–5309
54. F. Urbach, *Phys. Rev.*, 1953, **92**, 1324
55. A. Ates, M. A. Yildirim, M. Kundakci, M. Yildirim, *Chin. J. Phys.*, 2007, **45[2-I]**, 135-141
56. M. Kranjc, I. P. Studenyak, M.V. Kurik, *J. Non-Cryst. Solids*, 2009, **355**, 54–57
57. P. V. Sushko, D. Munoz Ramo, A. L. Shluger, *phys. stat. sol. a*, 2007, **204[3]**, 663– 669
58. T. Tomiki, Y. Ganaha, T. Shikenbaru, T. Futemma, M. Yuri, Y. Aiura, S. Sato, H. Fukutani, H. Kato, T. Miyahara, A. Yonesu, J. Tamashiro, *J. Phys. Soc. Jap.*, 1993, **62**, 573-584
59. Ch. Lushchik, E. Feldbach, A. Frorip, M. Kirm, A. Luschchik, A. Maaros, I. Martinson, *J. Phys. Condens. Matter*, 1994, **6**, 11177-11187
60. E. Feldbach, M. Kirm, P. Liblik, A. Maaros, T. Avarmaa, H. Mändarphys, 2007, *stat. sol. (c)*, **4[3]**, 930– 933

61. S. Watauchi, I. Tanaka, K. Hayashi, M. Hirano, H. Hosono, *J. Cryst. Growth*, 2002, **237–239**, 801–805
62. Tanak, M. Yamanaka, J.K. Park, T. Shimomura, S. Watauchi, K. Kishio, *J. Ceram. Process. Res.*, 2005, **6 [2]**, 129-133
63. K. Kurashige, Y. Toda, S. Matsumishi, K. Hayashi, M. Hirano, H. Hosono, *Cryst. Growth Des.*, 2006, **6 [7]**, 1602-1605
64. C. Song, J. Sun, S. Qiu, L. Yuan, J. Tu, Y. Torimoto, M. Sadakata, Q. Li, *Chem. Mater.*, 2008, **20**, 3473–3479
65. M. Matsuda, Y. Inada, W. Hisamatsu, K. Mashita, T. Umegaki, *J. Mater. Sci. Lett.*, 1996, **15**, 933-934
66. A. Cunejt Tas, *J. Am. Ceram. Soc.*, 1998, **81 [11]**, 2853–2863
67. H. Yanagi, K. Kim, I. Koizumi, M. Kikuchi, H. Hiramatsu, M. Miyakawa, T. Kamiya, M. Hirano, H. Hosono, *J. Phys. Chem. C*, 2009, **113**, 18379–18384
68. S. Kurajica, G. Mali, T. Gazivoda, J. Sipusic, V. Mandic, *J. Sol-Gel Sci. Technol.*, 2009, **50**, 58–68
69. C. Jing, X. Zhao, Y. Zhang, *Mater. Res. Bull.*, 2007, **42**, 600–608
70. A. A. Goktas, M. C. Weinberg, *J. Am. Ceram. Soc.*, 1991, **74 [5]**, 1066-1070
71. H. Kozuka, M. Kajimura, T. Hirano, K. Katayama, *J. Sol-Gel Sci. Technol.*, 2000, **19**, 205–209
72. A. Atkinson, R. M. Guppy, *J. Mater. Sci.*, 1991, **26**, 3869-3873
73. C. Jing, J. Hou, *J. Appl. Polym. Sci.*, 2007, **105**, 697-705



74. L. Huashi, C. Juan, G. Heyi, *J. Wuhan Uni. Technol. Mater. Sci. Ed.*, 2009, 68-71
75. D. Hoebbel, T. Reinert, H. Schmidt E. Arpac, *J. Sol-Gel Sci. Technol.*, 1997, **10**,115–126
76. L. Gong, Z. Lin, S. Ning, J. Sun, J. Shen, Y. Torimoto, Q. Li, *Mater. Lett.*, 2010, **64**, 1322–1324
77. M. M. Haridas, J. R. Bellare, *Ceram. Int.*, 1999, **25**, 613-616
78. X. Krokidis, P. Raybaud, A. Gobichon, B. Rebours, P. Euzen, H. Toulhoat, *J. Phys. Chem. B*, 2001, **105**, 5121-5130
79. C. J. Serna, J. L. White, S. L. Hem, *Clays Clay Miner.*, 1977, **25**, 384-391
80. Y. Su, H. Chen, W. Y. Lee, *J. Am. Ceram. Soc.*, 2005, **88** [11], 3235–3237
81. H. Kozuka, *J. Ceram. Soc. Jpn.*, 2003, **111** [9], 624-632
82. J. F. John,a S. Mahurin, S. Daib, M. J. Sepaniaka, *J. Raman Spectrosc.*, 2010, **41**, 4–11
83. V. Gonzalez-Pena, C. Marquez-Alvarez, I. Diaz, M. Grandea, T. Blasco, J. Perez-Pariente, *Microporous Mesoporous Mater.*, 2005, **80**, 173–182
84. K. Wefers, C. Misra, *Oxides and Hydroxides of Aluminium*, ALCOA Research Laboratories, United States of America, 1987, 20
85. K. Hayashi, N. Ueda, M. Hirano, H. Hosono, *Solid State Ionics*, 2004, **173**, 89–94
86. K. Hayashi, M. Hirano, H. Hosono, *J. Phys. Chem. B*, 2005, **109**, 11900-11906

87. F. Huang, J. Li, L. Wang, T. Dong, J. Tu, Y. Torimoto, M. Sadakata, Q. Li, *J. Phys. Chem. B*, 2005, **109**, 12032-12037
88. Katsuro Hayashi, *J. Phys. Chem. C*, 2011, **115**, 11003–11009
89. C. Song, J. Sun, J. Li, S. Ning, M. Yamamoto, J. Tu, Y. Torimoto, Q. Li, *J. Phys. Chem. C*, 2008, **112**, 19061–19068
90. Y. Toda, M. Miyakawa, K. Hayashi, T. Kamiya, M. Hirano, H. Hosono, *Thin Solid Films*, 2003, **445**, 309–312
91. K. Hayashi, Y. Toda, T. Kamiya, M. Hirano, *Appl. Phys. Lett.*, 2005, **86**, 022109
92. P. V. Sushko, A. L. Shluger, K. Hayashi, M. Hirano, H. Hosono, *Appl. Phys. Lett.*, 2005, **86**, 092101
93. S. Kim, S. Matsuishi, M. Miyakawa, K. Hayashi, M. Hirano, H. Hosono, *J. Mater. Sci: Mater Electron*, 2007, **18**, S5–S14
94. Y. Toda, Y. Kubota, M. Hirano, H. Hirayama, H. Hosono, *ACS nano*, 2011, **Vol. 5 [3]**, 1907–1914
95. M. Miyakawa, H. Hiramatsu, T. Kamiya, M. Hirano, H. Hosono, *J. Solid State Chem.*, 2010, **183**, 385–391
96. S. W. Kim, M. Miyakawa, K. Hayashi, T. Sakai, M. Hirano, H. Hosono, *J. Am. Chem. Soc.*, 2005, **127**, 1370-1371
97. S. Yang, J. N. Kondo, K. Hayashi, M. Hirano, K. Domen, H. Hosono, *Appl. Catal. A*, 2004, **277**, 239–246
98. C.H. Jung, P.H. Tai, Y.K. Kang, D.S. Jang, D.H. Yoon, *Surf. Coat. Technol.*, 2008, **202**, 5421–5424

99. K. B. Kim, M. Kikuchi, M. Miyakawa, H. Yanagi, T. Kamiya, M. Hirano, H. Hosono, *J. Phys. Chem. C*, 2007, **111** [24], 8403-8406
100. W. Lian, S. Chong-Fu, S. Jian-Qiu, H. Ying, L. Xiao-Guang, L. Quan-Xin, *Chin. Phys. Soc.*, 2008, **17** [6], 1674-1056
101. Z. Wang, Y. Pan, T. Dong, X. Zhu, T. Kan, L. Yuan, Y. Torimoto, M. Sadakata, Q. Li, *Applied Catal. A*, 2007, **320**, 24–34
102. Y. Pan, Z. Wang, T. Kan, X. Zhu, Q. Li, *Chin. Chem. Phys.*, 2006, **19** [3], 190-192
103. T. Dong, Z. Wang, L. Yuan, Y. Torimoto, M. Sadakata, Q. Li, *Catal. Lett.*, 2007, **119**, 29–39
104. A. Gao, X. Zhu, H. Wang, J. Tu, P. Lin, Y. Torimoto, M. Sadakata, Q. Li, *J. Phys. Chem. B*, 2006, **110**, 11854-11862
105. Y.C. Liu, J.H. Hsieh, S.K. Tung, *Thin Solid Films*, 2006, **510**, 32–38
106. L. Reimer, *Scanning Electron Microscopy: Physics of Image Formation and Microanalysis*, 2<sup>nd</sup> ed., Springer-Verlag, Germany, 1998, 2
107. B. D. Cullity, *Elements of X-ray Diffraction*, Addison-Wesley, United States of America, 1956, 78-96
108. W. F. Bleam, *Soil and Environmental Chemistry*, Academic Press, Elsevier Inc., United States of America, 2012, 109
109. C. D. Wagner, W. M. Riggs, L. E. Davis, J. F. Moulder, *Handbook of X-Ray Photoelectron Spectroscopy*, Perkin-Elmer Corp., United States of America, 1979, 5

110. R. M. Cornell, U. Schwermann, *The Iron Oxides: Structure, Properties, Reaction, Occurrences and Uses*, 2<sup>nd</sup> ed., Wiley-VCH GmbH & Co. KgaA, Germany, 2003, 169-170
111. B. Stuart, D. J. Ando, *Biological Applications of Infrared Spectroscopy*, John Wiley & Sons, Ltd, England, 1997, 47
112. J. R. Ferraro, K. Nakamoto, *Introductory Raman Spectroscopy*, 2<sup>nd</sup> ed., Elsevier Science, United States of America, 2003, 16
113. P. Wittung, J. Kajanusa, M. Kubistab, B. G. Malmstrom, *FEBS Letters*, 1994, **352**, 37- 40
114. J. Workman, *Applied Spectroscopy: A Compact Reference for Practitioners*, Academic Press, United States of America, 1998, 208
115. C. McDonagh, F. Sheridan, T. Butler, B.D. MacCraith, *J. Non-Cryst. Solids*, 1996, **194**, 72-77
116. R. Zhou, Q. Wei, K. Sun, L. Wang, *Microsc. Microanal.*, 2006, **12** [2], 1078-1079
117. A. C. Pierre, *Introduction to sol-gel processing*, Kluwer Academic Publishers, USA, 1998, 279- 309
118. M. N. Rahman, *Ceramic Processing and Sintering*, 2<sup>nd</sup> ed., Marcel Dekker, Inc., United States of America, 2005, 267-269
119. W. Li, B. S. Mitchell, *J. Non-Cryst. Solids*, 1999, **255**, 199-207
120. J. Lee, C. Won, B. Chun, H. Y. Sohn, *J. Mater. Res.*, 1993, **8**[12], 3151-3157

121. J. T. Kloprogge, L. V. Duong, B. J. Wood, R. L. Frost, *J. Colloid Interface Sci.*, 2006, **296**, 572–576
122. B. Demri, D. Muster, *J. Mater. Process. Technol.*, 1995, **55**, 311-314
123. B. V. Crist, *XPS Inter. LLC*, 2005, **Vol.2**, 59-65
124. S. Ardizzone, C.L. Bianchi, M. Fadoni, B. Vercelli, *Appl. Surf. Sci.*, 1997, **119**, 253-259
125. P.M. Chavhan, A. Sharma, R.K. Sharma, G. Singh, N.K. Kaushik, *Thin Solid Films*, 2010, **Vol. 519 [1]**, 18-23
126. J. S. Corneille, J. W. He, D. W. Goodman, *Surf. Sci.*, 1994, **Vol. 306 [3]**, 269-278
127. S. N. Ghosh, *Cement and Concrete Science and Technology*, Vol. 1, ABI Books Pvt. Ltd., India, 1991, 258-259
128. A. Gaki, R. Chrysafi, Th. Perraki, G. Kakali, *CI&CEQ*, 2006, **12 [2]**, 1370140
129. B. Chesnokov, *Dokl. Acad. Sci. USSR, Earth Sci. Sec.* (Engl. Transl.), 1995, **332**, 139
130. W. Horkner, H.K. Muller Buschbaum, *J. Inorg. Nucl. Chem.*, 1976, **38**, 983-984
131. F. Cervantes Lee, F. P. Glasser., *J. Appl. Crystallogr.*, 1979, **12**, 407-410
132. J. I. Langford, A. J. C. Wilson, *J. Appl. Cryst.*, 1978, **11**, 102-133
133. B.Y. A. R. Stokes, A. J. C. Wilson, *Proc. Phys. Soc.*, 1944, **56**, 174-181
134. G.K. Williamson, W.H. Hall, *Acta Metall.*, 1953, **Vol. 1 [1]**, 22-31

135. M. Zahedi, A. K. Ray, D. S. Barratt, *J. Phys. D: Appl. Phys.*, 2008, **41**, 035404
136. T. Dong, Zh. Wang, T. Kan, Q. Li, *Chin. J. Chem. Phys.*, 2007, **Vol. 20 [3]**, 297-304
137. D. E. Irish and G. E. Walrafen, *J. Chem. Phys.*, 1967, **46 [1]**, 378-384
138. Y. J. Liu, T. Zhu, D. F. Zhao, Z. F. Zhang, *Atmos. Chem. Phys.*, 2008, **8**, 7205–7215
139. J. Workman Jr., *Handbook of Organic Compounds*, Vol. 3, Elsevier Science, 2000, 66
140. P. K. Kipkemboi, P. C. Kiprono, J. Sanga, *Bull. Chem. Soc. Ethiop.*, 2003, **17 [2]**, 211-218
141. C. J. Serna, J. White, S. L. Hem, *Clays Clay Miner.*, 1977, **Vol. 25**, 384-391
142. H. D. Ruan, R. L. Frost, J. T. Kloprogge, *J. Raman Spectrosc.*, 2001, **32**, 745–750
143. L. Huashi, Ch. Juan, G. E. Heyi, *J. W. Uni. Technol. Mater. Sci.*, 2009, **Vol. 24 [1]**, 68-71
144. A. G. Kokhman, G. I. Zhmoidin, *Zhurnal Prikladnoi Spektroskopii* (Engl. Transl.), 1981, **Vol. 35 [6]**, 998-1003
145. N. Sakamoto, Y. Matsuyama, M. Hori, N. Wakiya, H. Suzuki, *Mater. Sci. Eng. B*, 2010, **173**, 21–24
146. Q. Mei, C. J. Benmore, J. Siewenie, J. K. R. Weber, M. Wilding, *J. Phys.: Condens. Matter*, 2008, **20**, 245106

147. G. I. Zhmoidin, A. K. Chatterdzhi, I. I. Plyusnina, *Zhurnal Prikladnoi Spektroskopii* (Engl. Transl.), 1972, **Vol. 16 [6]**, 1061-1066
148. P. Tarte, *Spectrochim. Acta Part A*, 1966, **Vol. 23 [7]**, 2127-2143
149. P. Mondal, J. W. Jeffery, *Acta Cryst.*, 1975, **B31**, 689-697
150. L. D. S. Yadav, *Organic Spectroscopy*, Kluwer Academic publishers, Netherlands, 2005, 61-62
151. T. Assih, A. Ayril, M. Abenoza, J. Phalippou, *J. Mater. Sci.*, 1988, **23**, 3326-3331
152. J. K. F. Tait, H. G. M. Edwards, D. W. Farwell, J. Yarwood, *Spectrochim. Acta Part A*, 1995, **51**, 2101-2106
153. L. Black, Ch. Breen, J. Yarwood, C. S. Deng, J. Phipps, G. Maitland, *J. Mater. Chem.*, 2006, **16**, 1263–1272
154. C. Tams, N. Enjalbert, *Appl. Note PerkinElmer, Inc*, 2009
155. T. S. Moss, G. J. Burrell, B. Ellis, *Semiconductor Optoelectronics*, Butterworth, 1973, 10
156. F. Wooten, *Optical Properties of Solids*, Academic Press, 1972, 49.
157. F. A. Jenkins, H. E. White, *Fundamentals of Optics*, McGraw-Hill Inc., 1981, 4th ed.
158. S. H. Wemple, H. Didomenico, *Phys. Rev.*, 1971, **3**, 1338–1351
159. P. Biljana, A. Bahattin, B. Irina, *J. Phys. Chem.*, 2010, **114**, 15280–15291
160. R. Murali, V. S. Vidya, M. Jayachandran, *Ionics*, 2008, **14**, 569–575

161. M. Caglar, Y. Caglar, S. Ilican, *J. Optoelectron. Adv. Mater.*, 2006, **8** [4], 1410 – 1413
162. J. I. Pankove, *Optical Processes in Semiconductors*, Dover Publications, New York, 1975, 93
163. T. Guang Lei, H. Hong Bo, S. Jian Da, *Chin. Phys. Lett.*, 2005, **22** [7], 1787-1789
164. J. Tauc, in *The Optical Properties of Solids*, ed. G. Harbeke, Academic Press Inc., New York, 1966, 303
165. A. Abu El-Fadl, A.S. Soltan, N.M. Shaalan, *Opt. Lasers Eng.*, 2007, **39**, 1310–1318
166. A. Majumdar, H. Z. Xu, F. Zhao, J. C. Keay, L. Jayasinghe, S. Khosravani, X. Lu, V. Kelkar, Z. Shi, *J. Appl. Phys.*, 2004, **Vol. 95** [3], 939-942
167. W. J. Martienssen, *Phys. Chem. Solids*, 1957, **2**, 257
168. T. Skettrup, *Phys. Rev. B*, 1978, **18** [6], 2622-2631
169. N. M. Ravindra, F. Demichelis, *Phys. Rev. B*, 1985, **32** [10], 6591-6595
170. H. Tang, F. Levy, H. Berger, P. E. Schmid, *Phys. Rev. B*, 1995, **52** [11], 7771-7774
171. A. E. Rakhshani, *J. Phys.: Condens. Matter*, 2000, **12**, 4391–4400
172. G. D. Cody, T. Tiedje, B. Abeles, B. Brooks, Y. Goldstein, *Phys. Rev. Lett.*, 1981, **47**, 1480-1483
173. Z. Yang, K.P. Homewood, M.S. Finney, M.A. Harry, K.J. Reeson, *J. Appl. Phys.*, 1995, **78**, 1958-1963



174. B. Abay, H. S. Guder, H. Efeoglu, Y. K. Yogurtcu, *J. Appl. Phys.*, 1998, **84**, 3872-3879
175. I. Dunja, M. Kranycec, B. Celustka, *J. Phys. Chem. Solids*, 1991, **52**, 915-920
176. A. Manoogian, J. C. Woolley, *Can. J. Phys.*, 1984, **62 [3]**, 285-287
177. Y. P. Varshni, *Physica*, 1967, **34**, 149-154
178. B. Abay, H. S. Guder, H. Efeoglu, Y. K. Yogurtcu, *Semicond. Sci. Technol.*, 2000, **15**, 535-541
179. A. B. Novoselova, *Physical-Chemical Properties of Semiconductors-Handbook*, Nauka, Moscow, 1978
180. K. L. Narayanan, K. P. Vijaykumar, K. G. M. Nair, N. S. Thampi, *Physica B*, 1997, **240 [1]**, 8-12